The Dissertation Committee for Prasanna Ganesan Krishnamurthy certifies that this is the approved version of the following dissertation:

Geologic Heterogeneity Controls On CO_2 Migration and Trapping

Committee:

David A. DiCarlo, Supervisor

Timothy A. Meckel, Co-Supervisor

Maša Prodanović

Steven L. Bryant

Larry W. Lake

Geologic Heterogeneity Controls On CO_2 Migration and Trapping

by

Prasanna Ganesan Krishnamurthy

DISSERTATION

Presented to the Faculty of the Graduate School of

The University of Texas at Austin

in Partial Fulfillment

of the Requirements

for the Degree of

DOCTOR OF PHILOSOPHY

THE UNIVERSITY OF TEXAS AT AUSTIN

May 2020

Dedicated to my parents Ganesan and Uma

Acknowledgments

They say it takes a village to raise a PhD. Truer words were never spoken. The support and encouragement of all the amazing people I interacted with and worked alongside, at Petroleum Engineering, Gulf Coast Carbon Center and the Jackson School of Geosciences has been fundamental for the success of this PhD.

First and foremost, my advisors. Thank you Tip for the tremendous support. You gave me the freedom to pursue new research directions, and new ideas and equipment in the lab, and when I failed (which happened all too often) you had my back. I am grateful to David for graciously accepting to be my advisor, 2 years into my PhD. Your guidance and gentle push has been very important whenever I hit a dead end.

I also would like to thank Larry Lake, Maša Prodanović and Steven Bryant for taking time to be on the committee and for their support. This work has benefited from the interesting questions Steve always likes to ask.

I am greatly indebted to Jim Buttles for giving my experiments a home at the Pickle Research Campus. I also thank David Mohrig, Wonsuck Kim, Bayani Cardenas and Blair Johnson for accommodating me. All of these faculty, practically strangers to me, from schools and departments I am not affiliated to, generously agreed to share their lab space with me. I thank the

students from these research groups: Max, Muhammad, Eric and Anna whose companionship added cheer to my life in that isolated lab.

David's research group was a fun, open and helpful place to talk science. It was great knowing and discussing ideas with Lauren, Hasan, Sid, Xiao and Rafael. I was fortunate to work with some great colleagues at the Gulf Coast Carbon Center. I thank Sue for her infectious enthusiasm and continued patronage of this work; Ramon Trevino for all the produce from his garden; and Peter, Mohammad, Sarah, Emily, Izaak and Reynaldy for all the fun times. In the early days of the lab, I had a chance to work with Luca Trevisan, whose experimental insights I am thankful for.

I'd like to thank my friends: Avani, Ajit, Jhanani, Ashish, Kaustubh, Arjun, Manoj, Esha and others for enriching my life and helping me maintain my sanity during tough times. Anil and Azmin were like family away from home and I will always be grateful for their never ending love and support. Thanks again to Anil and Advanced Micro Devices for sponsoring PCs and laptops for this research.

Lastly, I wouldn't be here without the support, love and sacrifice of my parents.

Geologic Heterogeneity Controls On CO_2 Migration and Trapping

by

Prasanna Ganesan Krishnamurthy, Ph.D.
The University of Texas at Austin, 2020

Supervisor: David A. DiCarlo
Co-Supervisor: Timothy A. Meckel

In this dissertation, we study the influence of small-scale geologic heterogeneities (mm to dm) on buoyant, vertical migration of CO_2 at intermediate length scales (sub-meter) in two different ways: using numerical simulations in highly resolved geologic models, and by visualizing flow through lab generated bedform fabrics. In the first part of this dissertation, we present a new technique to generate high resolution, 3D geocellular models that capture depositional architectures in a realistic manner. We then use a reduced physics formulation (Invasion Percolation) to simulate the migration of CO_2 through the developed models. Results from these simulations provide insight into how the trapped saturation is a non-linear function of the capillary entry pressure contrast between the primary lithologic features. This dependence suggests that some ability to predict CO_2 storage performance can be achieved from common sedimentological descriptors.

In the second half, we develop a unique experimental technique to generate intermediate scale (0.6m x 0.6m) beadpacks that mimic natural sedimentary features in a reproducible manner. We then perform a set of two-phase flow experiments in heterogeneous beadpacks with cross-stratified geometry, where the underlying geometry is kept constant but the grain size contrast is varied, analogous to our simulations. The experiments are conducted at atmospheric conditions using an immiscible fluid pair that mirrors the physical properties of supercritical CO_2 and brine at reservoir conditions. Light transmission is used to visualize the flows in real time and quantify fluid saturations at the millimeter scale. Observations from these experiments help corroborate our simulation results, showing that geometry and grain size variability strongly influence CO_2 flow and trapping behavior in a non-linear fashion.

We then conduct similar experiments at different flow rates and demonstrate the persistence of heterogeneity effects even at high flow rates and capillary numbers in such vertical flows. These results help demarcate trapping behavior at near well bore and far field conditions.

Together these experiments provide a unique opportunity to visualize complex multiphase flow dynamics in realistic geologic fabrics at the sub-meter scale, and can help bridge understanding between core scale experiments and reservoir scale observations.

Table of Contents

List of Tables

List of Figures

Chapter 1

Introduction

The Paris Agreement and its intended nationally determined contributions (INDCs) to limit global temperature rise "2 degrees Celsius above pre-industrial levels and to pursue efforts to limit the temperature increase even further to 1.5 degrees" require rapid reduction in greenhouse gas emissions. A majority of the developed emission scenarios that adhere to the goals of the Paris agreement feature Carbon Capture and Storage (CCS) as an important mitigation mechanism. CCS is considered to be one of the most cost-effective ways to achieve the essential net-zero emissions goal by the end of this century. CCS is key to neutralize emissions from hard-to-mitigate sectors such as air travel, freight and heavy manufacturing (Davis et al., 2018), and most crucially, it will enable the use of a wider mix of energy sources before transitioning to a renewable energy economy, thereby ensuring energy security in developing nations. Meeting the proposed emissions reduction goals calls for rapid and large-scale deployment of CCS (Rogelj et al., 2018), somewhere in the order of 40 Gt/year by 2100. To put that into perspective, to reach 1 Gt/year capacity by 2050, a million ton per year facility would need to be built every week starting now (Peters and Sognnaes, 2019) In 2019, the National Petroleum Council, while announcing the road map for CCUS in the

United States, called for a 20-fold increase in capacity from 20 to 500 Million tons /year in the next 2 decades. With the advent of the 45Q tax credit and climate investment funds like the OGCI keen on backing CCS projects, the need for increasing confidence in our capability to predict subsurface CO_2 flow behavior and estimate storage capacities is more than ever. *This dissertation focuses on multiphase flow in porous media that is relevant to geologic storage of CO_2.*

1.1 Background

Geologic CO_2 storage relies on different kinds of trapping mechanisms (Orr, 2009, Benson, 2005) to hold it in place: 1) stratigraphic or hydrodynamic trapping (Benson and Cole, 2008), where the buoyant CO_2 is trapped beneath impermeable rocks; 2) residual (Krevor et al., 2015), where the CO_2 is immobilized as isolated blobs or bubbles; 3) dissolution (Ennis-King and Paterson, 2005; Islam et al., 2016), where the CO_2 dissolves into the in-situ brine and the dense CO_2 rich brine sinks deeper into the reservoir; and 4) mineralization (Snaebjornsdottir et al., 2020), where the dissolved CO_2 precipitates to form carbonate minerals. Dissolution and mineralization are controlled by mass transfer and kinetic processes, and are predicted to occur over large timescales (hundreds to thousands of years or more). During injection, viscous dominated flow occurs driven by the pressure gradient. For typical field conditions and injection rates, pressure gradients weaken within hundreds of meters of the injection wells (Cavanagh and Haszeldine, 2014; Meckel and Bryant, 2014),

and buoyancy and capillary forces grow dominant over viscous forces. Thus, the rest of the storage domain, where the majority of the post injection CO_2 migration will occur is likely to be dominated by buoyancy and capillary forces.

During such flow regimes, small-scale geologic heterogeneities have been known to strongly influence multiphase flow dynamics (Corbett et al., 1992). For instance, bedform scale (decimeters to meters) depositional features such as laminated cross-strata that are common in most clastic reservoirs can act as capillary barriers resulting in oil entrapment (Ringrose et al., 1993). While the length scales of such depositional features are in the sub-meter range, their influence can propagate to affect large scale flow behavior (reservoir to basin) (Ringrose and Bentley, 2015).

1.2 Local Capillary Trapping

In the case of CO_2 storage, these small-scale capillary heterogeneities act to our advantage since the objective during CCS is trapping rather than mobilization. Post injection, as the CO_2 plume migrates upwards driven by buoyancy, it displaces the in-situ brine (drainage), while at the trailing edge imbibition occurs as the displaced formation brine re-invades the CO_2 filled pore space (Juanes et al., 2006). Trapping of CO_2 due to capillarity occurs during both drainage and imbibition, and at different length scales. Capillary trapping in the conventional sense also known as residual trapping occurs during imbibition due to pore scale events resulting in CO_2 immobilized as isolated blobs (Morrow, 1990; Krevor et al., 2015, Lenormand et al., 1983). Small

scale capillary heterogeneities cause CO_2 to accumulate beneath high capillary entry pressure barriers or laminae during drainage that get disconnected during imbibition. These accumulations or pools of CO_2 left behind in this form of trapping extend hundreds or thousands of pores across cm to decimeter scales at saturations higher than that of residual. They remain trapped since they lack the capillary entry pressure necessary to breach through the barriers. This is known as local capillary trapping, a new form of trapping proposed by Saadatpoor et al. (2010). Both forms of capillary trapping are considered to be safer than structural or hydrodynamic trapping which relies on the overlying caprock, and occur at relatively shorter time scales compared to the more secure dissolution or mineralization trapping mechanisms. Owing to the heterogeneous nature of most clastic reservoirs, it is expected that small scale capillary heterogeneities will play a significant role in influencing the CO_2 plume migration pathways (Bryant et al., 2006) and trapping behavior and in consequence the storage integrity and capacity (Li and Benson, 2015). Constraining the impact of such heterogeneities on CO_2 flow dynamics and trapping thus becomes essential.

The role of small-scale geological heterogeneities on CO_2 migration has been known for a while thanks to observations from the field as well as numerical simulations and laboratory experiments. The lateral spreading of the CO_2 plume beneath mudstone barriers in Sleipner (Cavanagh and Nazarian, 2014), and the early breakthrough at Frio (Hovorka et al. 2006) due to preferential low capillary entry pressure pathways have been attributed to such hetero-

geneities (Zhou et al., 2019). Numerical simulations at the meter (Li and Benson, 2015, Behzadi et al., 2012; Meckel et al., 2015, Bech and Frykman, 2018) and reservoir scales (Doughty and Pruess, 2004; Flett et al., 2007; Ide et al., 2007; Altundas et al., 2011; Lengler et al., 2010; Ren et al., 2015, Deng et al., 2012, Tavassoli et al., 2019) have shown how capillary heterogeneities contribute greatly to overall trapped saturations (Krevor et al., 2015), cause preferential flow pathways (Bryant et al., 2008), disperse the CO_2 through the reservoir by inducing lateral migration (Saadatpoor et al., 2010; Gershenzon et al., 2015), and retard plume migration rates (Saadatpoor et al., 2008, Li and Benson, 2015). On the experimental front core flooding using whole rock cores and small core plugs have been widely used to demonstrate the effects of mm to cm scale depositional heterogeneities (Kuo et al., 2011; Shi et al, 2011; Krevor et al., 2011, 2012; Pini et al., 2012; Pini and Benson, 2013; Krause et al., 2013; Ni et al., 2019; Reynolds et al., 2018; Herring et al., 2013, 2015). Using integrated experimental and modeling approaches, various studies have emphasized the need to account for capillary dominated flows (Reynolds and Krevor, 2015) while measuring important flow properties like relative permeability in the presence of heterogeneities (Perrin and Benson, 2010; Jackson et al, 2018; Akbarabadi and Piri, 2013). To account for buoyancy, carefully controlled vertical core-flooding studies have also been conducted lately (Oh et al., 2015; Krishnamurthy et al., 2017). At the intermediate scale, a series of sand-pack experiments by Trevisan et al. (2014, 2015, 2017b) explored how capillary barriers at the sub-meter scale can increase trapped non-wetting

phase saturation and plume migration times.

1.3 Outline

A longstanding challenge in this area has been quantifying the effect of small-scale heterogeneities on flow and trapping behavior. This calls for a systematic study that accounts for natural geologic heterogeneities and the relevant flow physics accurately. To be able to delineate the effect of different heterogeneous features, synthetic but nature mimicking model domains where the heterogeneity can be engineered are needed. *In this dissertation, we tackle this challenge using numerical modeling and experiments, and aim to advance our understanding of multiphase flows in heterogeneous porous media.*

There are various metrics to quantify geological heterogeneity. Here we ask the question: *Whether we can predict CO_2 trapping performance and storage capacity (i.e. saturations) in rocks using common sedimentological and lithologic descriptors of heterogeneity.* This becomes the leitmotif of this dissertation.

This dissertation is organized into 6 chapters.

In Chapter 2, the effect of two different geologic heterogeneity parameters: fabric (arrangement of the depositional features), and lithology (grain size distribution), on CO_2 drainage saturations is investigated numerically. To achieve this, a method to generate 3D, high resolution, geologically realistic sedimentary models is developed. Macroscopic Invasion Percolation is used to

simulate flow through the developed flow domains. Exploring a large parameters space that includes eight depositional fabrics and forty different grain size distributions, a non-linear correlation model between the grain size heterogeneity metric and the CO_2 drainage saturations is developed. In Chapter 3, starting with a brief review of previous experimental studies that have investigated heterogeneity, a new method to generate bedform mimicking, 2D, intermediate scale (0.6m $\times$ 0.6m $\times$ 0.02m) beadpacks for conducting flow experiments is presented. Using the said method, flow experiments analogous to the simulations in Chapter 2 are presented in Chapter 4. A surrogate fluid pair that mimics physical properties of supercritical CO_2 and brine is used to conduct the experiments at room temperatures and pressures. Using light transmission to quantify fluid saturations, the impact and persistence of local capillary trapping is investigated. The results are used to compare and validate the predictive model proposed in Chapter 2 and application of the model to the field scale is discussed. In Chapter 5, the effect of flow rates on heterogeneity trapping is investigated experimentally. Using flow rates that vary over three orders of magnitude the persistence of the effect of small-scale heterogeneities is investigated. Finally, an overview of the contributions of this dissertation and future work are discussed in Chapter 6.

Chapter 2

Influence of Small Scale Geologic Heterogeneities on CO_2 Migration: Invasion Percolation Simulations

During CO_2 sequestration, the influence of subsurface heterogeneities on the long term migration and trapping of CO_2 has been recognized, but incorporating these features in numerical simulations at the correct length scales, in a physically rational manner remains problematic. In this chapter, we address this challenge. We first introduce a method to generate high resolution, 3D geocellular models that capture depositional architectures in a realistic manner. Using a reduced physics flow modeling technique, we then simulate the buoyant flow of CO_2 through these natural geologic models. The ensemble behavior, from thousands of MIP simulations reveal saturation in the eight models to be a non-linear function that is primarily influenced by the contrast in threshold capillary pressures between matrix and lamina (observable lithologic heterogeneity), suggesting some predictive ability is achievable from

Based on "Impact of 3D capillary heterogeneity and bedform architecture at the submeter scale on CO_2 saturation for buoyant flow in clastic aquifers", L Trevisan, PG Krishnamurthy and TA Meckel ,International Journal of Greenhouse Gas Control, 56, 237-249(2017) PGK helped design and conduct the research and co-wrote the manuscript.

common sedimentologic descriptors, although quantifying the independent effect of depositional architecture remains elusive.

2.1 Introduction

In order to predict subsurface CO_2 plume behavior and to assess storage capacity, continuum-based multiphase flow models are conventionally applied at the reservoir scale. Typically, these models utilize coarse grids (100s of meters) with upscaled properties (e.g. permeability, residual gas saturation) in order to be computationally efficient. Failure to account for geological heterogeneity, especially capillary pressure has been shown to result in overestimation of the migration speed (Li and Benson, 2015), mismatch of breakthrough times (Green and Ennis-King, 2010; 2013), and underestimation of final trapped saturation (Saadatpoor et al., 2010) and lateral extent of CO_2 (Hesse and Woods, 2010).

An alternative to developing upscaled properties for reservoir scale simulations (Pickup et al., 1994; Pickup and Hern, 2002; Ringrose et al., 2008; Mouche et al., 2010; Gasda et al., 2013; Rabinovich et al., 2015) is to simulate flow in highly resolved geologic domains that represent heterogeneity at the scales previously established as critical to capture essential multiphase flow behavior (Hartkamp-Bakker, 1991; Graue, 1994; Ringrose and Corbett, 1994; Li and Benson, 2015). However representing features at the depositional scale requires an extremely large number (10s to 100s of millions) of small (mm to dm scale) gridblocks which in turn requires very high computational resources.

To circumvent this limitation, we use Macroscopic Invasion Percolation (MIP) (Wilkinson and Willemsen, 1983; Kueper and McWhorter, 1992; Yortsos et al. 1993; Carruthers, 2003), a reduced physics flow modeling technique. MIP is considered here for two main reasons: 1) it captures the relevant flow physics during CO_2 migration: the interplay between capillary and buoyancy forces and 2) owing to its speed and efficiency, it lets us honor fine-scale heterogeneity in flow simulations at reasonable computational costs.

Heterogeneity is a multi-scale phenomenon, but in particular, geologic features at the sub-meter scale (bedform scale) have been attributed to have a significant impact on multiphase flows even at the large scale (100s to 1000s meters)(Pickup et al., 1994; Ringrose and Corbett, 1994). Our focus in this work is on the geometry and distribution of facies at the centimeter to meter scale. For the purposes of this research, heterogeneity is considered to be composed of 1) a lithological component and 2) a fabric component. The lithological component relates to grain sizes, and specifically to contrasts in grain size between depositional laminae (typically finer-grained; baffles) and the matrix. These grain sizes and contrasts are controlled by the average energy (magnitude) of flow velocity (average grain size in transport) and fluctuations in energy of deposition, with more consistent energy producing more homogenous materials (less overall grain size contrast). The fabric component relates to the depositional organization of the laminae, typically described as ripples,cross stratification etc., and depends on the flow regime of deposition. Our goal is to consider a wide range of lithological contrasts and fabrics rep-

resentative of typical geologic depositional settings to understand the primary factors influencing buoyant fluid saturation in realistic materials.

Here, we build upon previous work by Meckel (2013) and Meckel et al. (2015) to address the influence of stratigraphic heterogeneity at the sub-meter scale on the containment of CO_2 for different types of sedimentary architectures. To adequately represent 3D heterogeneity, we present numerical models that combine a deterministic bedform architecture component with stochastic variability of petrophysical properties. One advantage of this approach is that it allows consideration of domain sizes larger than whole core and core plugs typically used for laboratory flow experiments, where small sizes may not fully capture depositional architecture. A similar approach has been described for different purposes in previous studies (Cox et al., 1994; Kjonsvik et al., 1994; Nordahl et al., 2005; Nordahl and Ringrose, 2008; Behzadi et al., 2012). Conclusions reported by Meckel et al. (2015) for 2D simulations suggest that basic geological features such as grain size distribution and sedimentary bedform architecture can be used to predict the fraction of rock invaded by CO_2 during capillary/buoyancy-dominated flow conditions. In the present work, we aim at improving capacity estimations by accounting for the third dimension, as well as through a more realistic representation of the sub-meter scale heterogeneity.

Our approach for efficiently accounting for capillary heterogeneity trapping in storage capacity estimations consists of developing a work-flow that involves systematic IP simulations applied to a large range of geological models characterized by different bedform architectures and threshold capillary pres-

sure (P_{th}) fields with increasing contrast between matrix and laminae facies. Our conceptual model relies on the assumption that for post-injection, far-field scenarios, CO_2 migration can be considered to be under capillary equilibrium, thereby reducing the problem to a static balance between capillary and buoyancy forces. The main contribution of this chapter is the development of a predictive model for CO_2 capacity estimation based on a comprehensive, yet simplified, set of geological models resembling a range of fluvial facies. These models are unique in regard to their geological realism and permit evaluation of the impact of sub-meter scale capillary heterogeneity on buoyant fluid flow scenarios that are relevant to the long term behavior of the injected CO_2.

2.2 Flow Regimes and Invasion Percolation

In the subsurface, CO_2 migration is controlled by the interplay of viscous, capillary and buoyancy forces. Depending on the relative dominance of these forces, the CO_2 flow regime varies from compact flow to capillary dominated flow. These flow regimes are characterized by specific displacement patterns that are described by dimensionless groups, like the Bond number, Capillary number, and viscosity ratio, constraining a parameter space such as the one introduced by Lenormand et al. (1988). When large pressure gradients are present, e.g. in the near-wellbore zone, viscous-dominated displacements are likely to occur, while capillary and buoyancy-dominated flow regimes become more prevalent in far-field areas, where the injection-induced pressure gradient has already dissipated. Recent reports from the Sleipner project high-

light the fact that buoyancy forces take control not far from the wellbore after which the upward migration of CO_2 towards the seal is only a function of capillary and gravity forces (Andrew et al. 2015). Thus, it is safe to hypothesize that the storage domain will mostly experience buoyancy/capillary dominated flow of CO_2.

Taking into account the CO_2 flow regimes, secondary hydrocarbon migration can be considered to be a good proxy for buoyancy dominated CO_2 migration (Hermanrud et al. 2010). The principal driving force in hydrocarbon migration is the density difference (buoyancy) and the competing force is the capillary pressure (Vasseur et al., 2013) since the rocks are brine saturated. With very low rates of expulsion at the source the capillary numbers during this process have been found to be around 1E-10, thus making it completely capillary dominated (England et al. 1987). In comparison, post injection CO_2 migration rates have been reported to be in the range of 1E-10 to 1E-7 (Soroush et al. 2014, Cavanagh and Haseldine 2014, Yan et al., 2012). Various laboratory observations (Dembicki and Anderson, 1989; Catalan et al., 1992; Frette et al., 1992; Rasmussen, 1997) have shown that, in such a capillary dominated regime, hydrocarbons migrate as stringers (stringer is a continuous phase of oil between two points) driven by buoyancy forces. When the hydrostatic head of the stringer is greater than the capillary entry pressure of the upstream pores, it is able to invade the pores. If there is not enough pressure, the oil accumulates beneath the barrier until more charge replenishes it and sufficient potential energy is available to the stringer breach the capillary entry

pressure barrier.

$$\Delta\rho g h_c = P_{nw} - P_w = \frac{2\gamma\cos\theta}{R} \tag{2.1}$$

Where h_c is the accumulation height, $\Delta\rho$ is the density difference, γ is the interfacial tension, θ is the contact angle and R is the pore radius.

Based on these observations, Frette et al. (1992) suggested that secondary oil migration flows could be modeled by incorporating gravity forces in Invasion Percolation, a quasi-static technique that was originally developed to model the capillary driven immiscible displacement in porous media (Wilkinson and Willemsen, 1983). Invasion Percolation has since been used by various groups to model secondary hydrocarbon migration (Meakin et al. 2000; Carruthers and Ringrose, 1998; Luo et al., 2007). Considering the similarities between the flow regimes in CO_2, and hydrocarbon migration, and the early work by Hermanrud et al. (2010) to model CO_2 plume movement using Invasion Percolation, IP has gained attention in the CO_2 storage community (Cavanagh et al. 2015; Cavanagh and Haszeldine, 2014)

2.3 Developing 3D Geologic Models

We investigate the impact of bedform architecture and capillary pressure heterogeneity at the sub-meter scale on CO_2 trapping. Three type of methods are commonly applied to represent lithological variations in reservoir modeling: structure-imitating, process-imitating, and descriptive (Koltermann

and Gorelick, 1996). The approach adopted in this study falls into the second category; by means of forward modeling sedimentary processes (Rubin and Carter, 2005) we attempt to mimic depositional architectures, focusing on unconsolidated clastic deposits of fluvial origin. Due to the strong influence of small-scale heterogeneity attributable to this type of stratigraphic architecture on capillary trapping of CO_2, these type of reservoirs are often considered valuable when screening for candidates (Gershenzon et al., 2015).

The approach to consider a large spectrum of possible geological models embraces three concepts: (1) different sedimentary processes lead to a variety of bedform architecture models (BAM), (2) each depositional environment can be defined by a unique facies with characteristic grain size distribution, (3) the impact of crossbedded stratification on capillary heterogeneity can be inferred by pairing facies with variable textural contrast in a series of matrix-laminae cases.

2.3.1 Bedform architecture models (BAM)

With the goal of reproducing various types of bedforms produced by a range of depositional processes, Rubin (1987) developed a model that generated images of sedimentary bedform structures and provided reference cases in the form of scaled photographs of outcrops. More recently, Rubin and Carter (2005) converted the existing program into an open-source MATLAB package. Even though the main purpose of the codes was to visually interpret sedimentary deposits and depositional environments, Rubin's algorithm

has been adopted by a number of authors to investigate the effect of cross-laminated sediments on hydrocarbon recovery (Cox et al., 1994; Kjonsvik et al., 1994; Ringrose et al., 2003; Nordahl et al., 2005; Ma et al., 2008). For the specific application of this study, which involves three-dimensional IP simulations, we implemented the original script from Rubin and Carter (2005) with a modification that converts the workspace variables associated with the computer-graphics output into three-dimensional binary volumes (matrix = 0; laminae = 1) that can be used to populate numerical grids. The MATLAB code along with instructions on how to generate bedform models and populate them with petrophysical parameters can be freely obtained from here: Meckel et al., Sci Rep 7, 9238 (2017)

Among the 62 bedforms illustrated in Rubin (1987), we take into account those related to fluvial depositional environments and characterized by sub-meter scale heterogeneity (Figure 2.1). Also, in order to represent each of the main bedform subsets described by Rubin and Carter (2005), we select eight models characterized by different classification criteria, such as dimensionality, variability, and orientation relative to transport (Table 2.1). The first model (No.3 in Rubin (1987)) is a structure formed by two-dimensional bedforms climbing vertically. The second model (No.5) represents a structure qualitatively described by tabular sets and 'deposited by two-dimensional bedforms climbing at a stoss-erosional, lee-depositional, net-positive angle of climb'. The third model (No.13) represents a structure formed by 'bedforms climbing at an angle that is fluctuating but always positive'. The fourth model

(No.19) represents a structure qualitatively described by zig-zag bedding features and 'produced by symmetrical bedforms that migrate back and forth a fraction of the distance of the bedform spacing with no net displacement'. The fifth model (No.27) represents a structure formed by 'bedforms with superimposed bedforms migrating in the opposite direction'. The sixth model (No.36) represents a structure formed by 'bedforms with pseudorandom planform geometry'. The seventh model (No.42a) represents a structure qualitatively described by trough sets and 'formed by bedforms with along-crest-migrating in-phase sinuosities'. The eighth model (No.63) represents a structure qualitatively described by rippleform features and 'formed by reversing, three-dimensional bedforms'. While these descriptors are rigorous, they are observational and process-based, making them entirely suitable for systematic descriptions of geologic materials (e.g. subsurface cores).

To summarize, the sedimentary models presented in this study allow for representation of different depositional environments by generating patterns of grain size heterogeneity emphasized by finer-grained laminae in a more prevalent coarser-grained matrix. Although grain size variability in natural sedimentary deposits can exhibit a continuum of values (Meckel, 2013), the primary assumption made in this study is that each BAM can be described by the spatial arrangement of two depositional and rigorously descriptive features: matrix and laminae facies. These finer-grained (lower-permeability, higher threshold pressure) laminae are known to influence fluid flow and accumulation arrangements at variable scales (Corbett et al., 1992; Mikes and

Bruining, 2006; Gershenzon et al., 2015; Luo et al., 2015). Models developed here specifically emphasize these two components, and explore the degree of contrast that could occur between them. A major advantage of these models is their geological realism, making them recognizable and correlated to depositional environments with a rich research history. Other methods that might achieve this are structure-imitating techniques, although models generated with these methods generally consider larger domains equivalent to reservoir-scale, with a focus on spatial inter-relationships of various facies (e.g. point bar, crevasse splay, channel, etc.). Models used here focus on smaller scale features that might exist within each of those depositional lithologies.

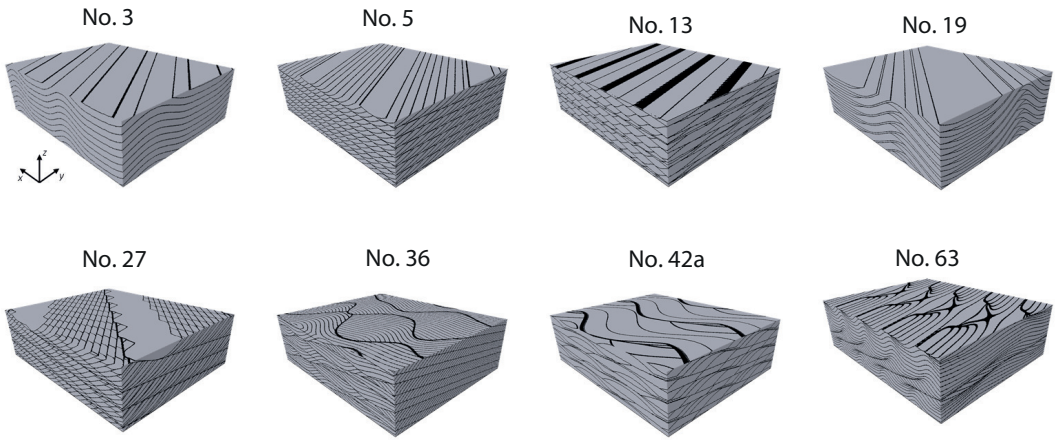

Figure 2.1: The eight sedimentary models generated with modified MATLAB script that are used in this study. The numerical grids (XYZ) consist of $495 \times 400 \times 142$ cells, corresponding to $(0.99 \times 0.8 \times 0.28)$ m^3

2.3.2 Grain Size Characterization

Threshold capillary pressure, P_{th}, also defined as displacement or entry pressure, is a key parameter controlling the migration pathway of CO_2, especially when flow occurs in the capillary limit (Saadatpoor et al., 2010). To make our study applicable to actual field settings, we consider a range of values that are expected in unconsolidated clastic reservoirs. Based on textural parameters such as grain size and grain sorting, Beard and Weyl (1973) classified 54 artificially mixed unconsolidated sands into eight grain-size subclasses and six sorting groups. Following previous work of Meckel et al. (2015), we used this classification to extrapolate realistic P_{th} values and populate each BAM with different degrees of textural contrast between matrix and laminae values, as characterized by the difference in the mean of the distributions used for each.

The grain size is subsequently used to calculate P_{th} (in kPa) using equation 2 from Berg (1975):

$$P_{th} = 16.3 \times \frac{\gamma}{d_{50}} \tag{2.2}$$

Where 16.3 is a geometric constant that also incorporates unit conversion, γ is interfacial tension in N/m, and d_{50} is median grain diameter, in millimeters. In this study we use $\gamma = 0.03$ mN/m for CO_2-H_2O system, representative for reservoirs at approximately 10 MPa and 35^o (Chiquet et al., 2007). Each of the facies shown in Figure 2.2 has a lognormal grain size dis-

tribution and is described by the median diameter (d_{50}) and the Trask sorting coefficient (S_o). We convert these grain size distributions to analogous capillary threshold pressure distributions as described below. The Trask sorting coefficient (S_o) is defined as the square root of the ratio of the 25th to the 75th percentile of the cumulative density function of the lognormal distribution:

$$S_0 = \sqrt{\frac{d_{25}}{d_{75}}} \tag{2.3}$$

Where d is grain size in millimeters. Since the grain sizes are often log normally distributed (Folk, 1966), the logarithm of the grain size (D) will be normally distributed and is given as:

$$D = \log(d) \tag{2.4}$$

Then, substituting 4 into 3, the Trask sorting coefficient can be rewritten as:

$$S_0 = e^{\frac{D_{25} - D_{75}}{2}} \tag{2.5}$$

For a normal distribution, the quantile function is defined as:

$$D = \mu + \sigma\sqrt{2} erf^{-1}(1 - 2p) \tag{2.6}$$

Where is the mean, is the standard deviation and is the cumulative probability. The mean of the normal distribution is given by the logarithm of

the median of the lognormal distribution:

$$\mu = \log\left(d_{50}\right) \tag{2.7}$$

Substituting 6 and 7 into 5, we solve for the standard deviation of the normal distribution. Then, using the calculated mean and the standard deviation, for cumulative probabilities from 0 to 0.999, we calculate the inverse CDF which gives the values of the normal distribution. Since these are logarithmic values, the antilog gives back the lognormally distributed grain sizes in millimeters. These values are then substituted in equation 2 to obtain log-normally distributed P_{th} values. The main input parameters for the numerical models are the arithmetic mean (m.) and standard deviation (s.d.) of the log-normally distributed P_{th} PDF of matrix and laminae values, which are calculated as follows:

$$\begin{aligned} m. &= e^{\left(\mu+\frac{1}{2}\sigma^2\right)} \\ \text{s. } d. &= e^{\left(\mu+\frac{1}{2}\sigma^2\right)}\sqrt{e^{(\sigma^2)}-1} \end{aligned} \tag{2.8}$$

Where μ is the mean and σ is the standard deviation of P_{th} PDF on a logarithmic scale.

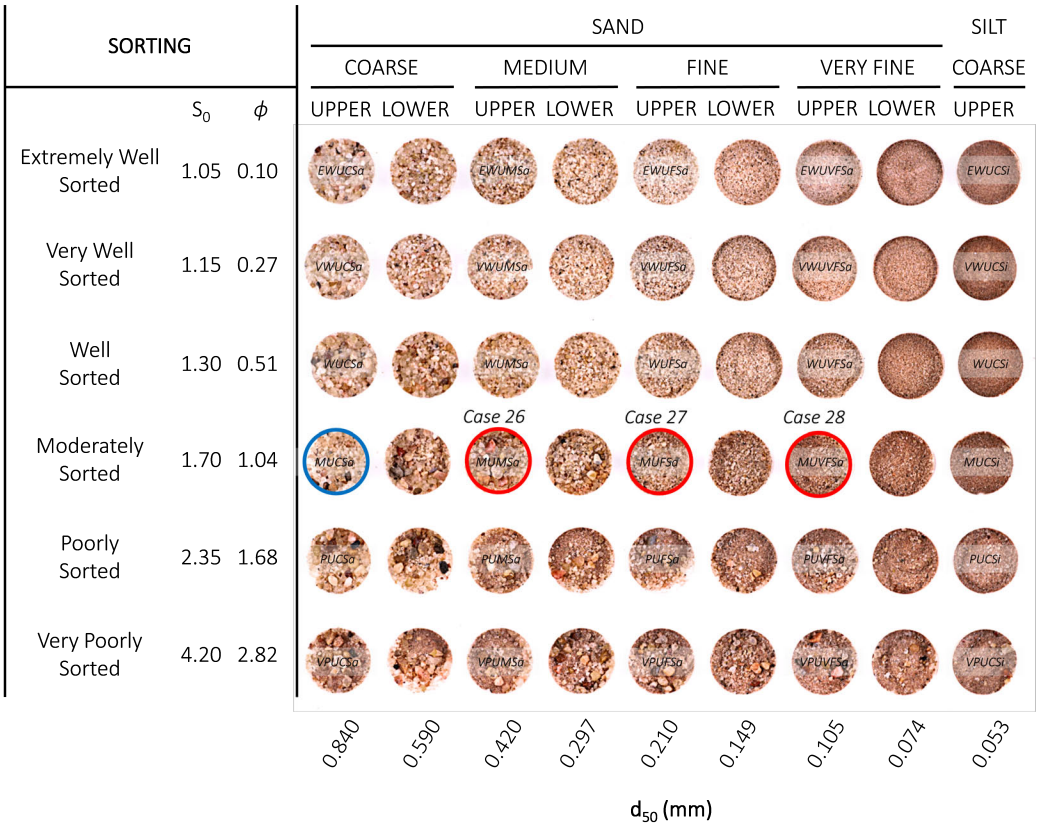

Figure 2.2: The library of 54 facies used for assignment of Pth values to matrix and laminae in the eight BAMs. Each facies has a specific distribution of grain sizes described by a median value (columns) and sorting category (rows). Sorting is given in terms of Trask coefficient S_o and ϕ scale [Folk and Ward, 1957]. These facies are characteristic of a wide range of clastic depositional processes and environments. For example, very fine grained, well sorted silt reflects upper point bar deposits of fluvial deposits, poorly sorted coarse sand reflects channel thalwegs, and very well sorted medium sand typically occurs in shoreface environments. Permeabilities for these materials range from 471 Darcy (extremely well sorted upper coarse sand, upper left) to 50 mD (very poorly sorted upper coarse silt, lower right) (Beard and Weyl [1973], their Table 6). To illustrate the methodology used for generating different textural contrasts, three cases are shown where MUCSa represents the matrix facies and MUMSa, MUFSa, and MUVFSa are used for the laminae of cases 26, 27, and 28, respectively.

2.3.3 Lithologic variability

In reservoir characterization, geological heterogeneity is generally measured by coefficients of variation that consider the central tendency of the property of interest (e.g. P_{th}) across the medium. The bimodality of P_{th} distribution, however, represents a key controlling parameter in this study and needs to be reflected in coefficients that are used to predict capillary trapping capacity. To characterize the textural contrast between matrix and laminae for each modeling scenario, we introduce the dimensionless parameter, :

$$\delta = \frac{|\mu_1 - \mu_2|}{\sigma} \tag{2.9}$$

Where μ_1 and μ_2 are the means (on a logarithmic scale)of P_{th} PDF assigned to of the matrix and lamina, respectively, and σ is the standard deviation of P_{th} PDF (also on a logarithmic scale) assigned to the laminae. Since the pairings of matrix and laminae share the same sorting category for all the examples presented here, hence the same standard deviation of the P_{th} PDF, only one appears at the denominator of equation 11. As it will be shown in the Discussion section, the parameter appears to correlate well with the average model saturation predicted across a large range of different textural contrasts. More importantly, the variables involved in the quantification of are directly available from the classification of Beard and Weyl (1973) and simple to gather in the field or from a core description. To visually illustrate the influence of different facies combinations on textural contrast between matrix and laminae,

Figure 2.3 shows the resulting P_{th} PDFs for the three example cases presented in Figure 2.2. As mentioned above, with the purpose of representing realistic depositional environments, grain sizes assigned to matrix facies are always coarser than grain sizes assigned to the laminae. Also, an attempt was made to represent a large part of the ensemble of possible combinations by selecting 40 different matrix-laminae cases (Appendix: Figure 2.12). These cases can be grouped in a 5 by 8 matrix, having sorting categories as rows, and textural contrast between matrix (in blue) and laminae (in red) as columns (Appendix Figure 2.13).

As it will be demonstrated in the next sections, the baffle effect exerted by the laminae on the buoyant plume is closely related to the bimodal character of the P_{th} PDF and it manifests itself with different plume distributions across the eight BAMs.

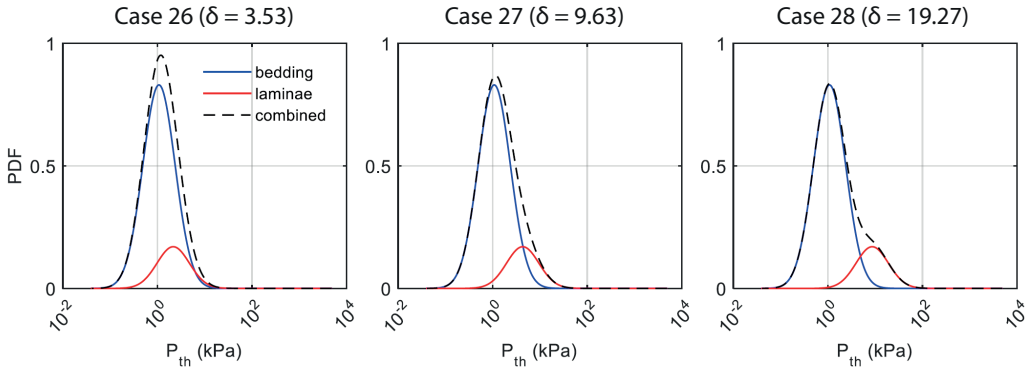

Figure 2.3: Three different textural contrasts created by assigning constant Pth PDF to matrix (in this case Moderately Sorted Upper Coarse Sand, or MUCSa, in blue) and changing P_{th} PDF of laminae (in this case showing Upper Medium Sand > Upper Fine Sand > Upper Very Fine Sand, from low to high P_{th}, in red). The complete set of 40 cases is available in the supplementary information.

2.3.4 Representative Elementary Volume

Prior to charging the porous medium with CO_2 through IP simulations, we evaluated the effect of spatial scale on variation of heterogeneity in order to determine the appropriate representative elementary volume (REV) for the numerical domain. The purpose of this analysis is two fold: 1) to save computational time by selecting models with efficient grid sizes and 2) to relate average storage capacity predictions with grid block volumes that can be considered for a future upscaling study. The property of the medium we target for REV identification is the matrix to laminae ratio, which is analogous to the net-to-gross sand/shale ratio (Flett et al., 2007) and merely represents the volumetric fraction of matrix cells. As previously pointed out by other authors (Ma et al., 2008), we consider this property to significantly affect the overall distribution of CO_2 under quasi-static buoyant flow.

The methodology used to identify the size of the REV combined the approach followed by Bear (2013) and Nordahl and Ringrose (2008). To calculate the matrix to laminae ratio for each BAM illustrated in Figure 2.1, cubic subsets with progressively larger dimensions are extracted from the center of the full size $495 \times 142 \times 400$ cells model and plotted as a function of sample volume. Data presented in Figure 2.4 show a common behavior converging towards constant plateaus, indicating $8.24 \times$ 10-3 m^3 (0.202 m $\times$ 0.202 m $\times$ 0.202 m) as a potential effective medium volume for approximating matrix to lamina ratio heterogeneity at larger scales. For the BAMs involved in this study, matrix to lamina ratios range between 0.81 and 0.94.

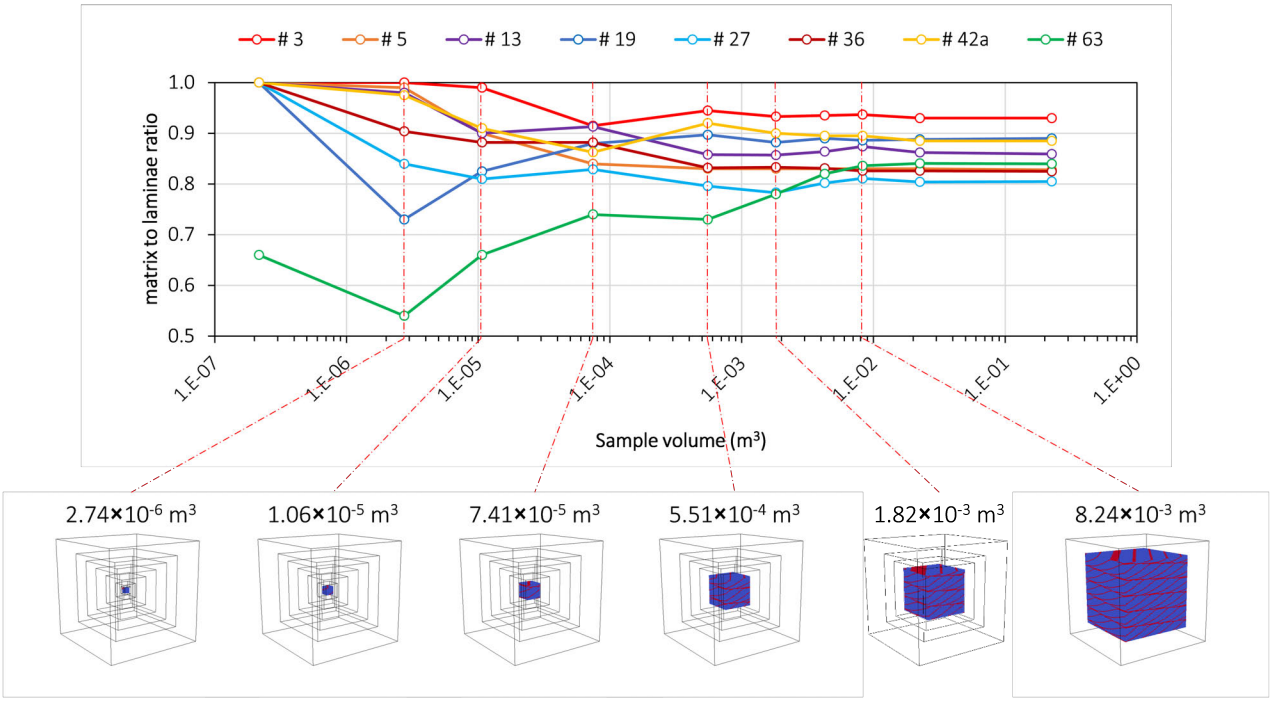

Figure 2.4: Matrix to laminae ratio as a function of sample volume. Each sample volume corresponds to a cubic subset extracted from the middle of the full size BAM.

2.4 Modeling

Based on seismic observations gathered at the Sleipner storage site (Chadwick et al., 2010) following injection of a large volume of CO_2 in a brine-bearing sedimentary formation, continuous-phase high-saturation plumes can be structurally trapped underneath low permeability baffles in a stacked layer configuration (Figure 2.5). We setup our simulations based on a scenario where the model domain (assumed to be located between two baffles in Figure 2.5) is underlain by a near infinite source of CO_2. An analog approach for representing such boundary condition has been previously adopted in numerical simulations studying CO_2 migration dominated by capillarity and buoyancy (Bryant et al., 2008; Saadatpoor et al., 2010; Ren et al., 2015).

The numerical simulations are based on the assumption that post-injection, pressure gradients have dissipated and the migration of CO_2 is mainly controlled by 1) the density difference between the two phases and 2) the spatial arrangement of facies with contrasting P_{th} within the reservoir.

The Invasion Percolation simulations are carried out with Permedia's Static Migration model, which despite its original scope of capturing the transport processes of secondary oil migration, has been recently proved capable of matching certain aspects of CO_2 migration (Cavanagh and Haszeldine, 2014). Permedia is a commercial simulator that utilizes a gravity destabilized macroscopic IP modeling scheme. Traditional IP algorithms model pore scale fluid displacement processes where drainage and imbibition can be modeled as bond and site percolation, respectively. Permedia utilizes a macroscopic approach

(Kueper and McWhorter, 1992; Ioannidis et al., 1996; Glass and Yarrington, 2003; Yang et al., 2013), where the lattice sites/cells are considered to be a macroscopic block with averaged capillary entry pressures instead of as a single pore. Permedia accounts for buoyancy thereby allowing the formulation of gravity destabilized flow scenarios. Commonly used IP models that account for gravity do so by implementing a simple vertical gradient proportional to the height of the cell above the base layer (Meakin et al., 1992). This is based on the assumption that the invading phase forms a continuous and connected path across the domain. Since this does not accurately represent the physics and the invading phase undergoes fragmentation, in Permedia the buoyancy pressure is calculated dynamically from the top of the connected/active cluster (Carruthers, 1998). These connected clusters formed due to backfilling at capillary barriers are called 'accumulations'. The rest of the plume consists of stringers that are classified as 'migration pathways'. Permedia also allows bicontinua of fluids to occupy each grid block. However, unlike other IP models which use the Pc-S curve to determine the saturation at each cell (Kueper and McWhorter, 1992), in Permedia the cells that form the accumulation are assigned non-wetting phase saturation equal to 1-Swc (connate water saturation) and the migration pathways are assigned critical/residual non-wetting saturation. Fragmentation due to capillary forces is implemented by assuming that snap-off occurs in migration pathways where the oil saturation is just enough to form a spanning cluster. Snap-off occurs when the pore to throat size ratio is small i.e. when low entry pressure cells are surrounded by high

entry pressure cells (Carruthers, 1998). As such, the specific simulator used is not dissimilar from many modified IP simulators.

One of the main benefits of Permedia's IP simulator compared to Darcy-based solvers is the capability to represent geological heterogeneity with a higher degree of resolution, without compromising on computational time. We take advantage of this by carrying out stochastic simulations through a large number of realizations of the P_{th} field. This approach allows us to account for the high uncertainty of natural geological heterogeneity by correlating grain size distribution with standard deviation of the P_{th} probability distribution function (PDF). For this purpose, batch simulations including 200 equiprobable realizations of the P_{th} field were carried out to represent the variability of solutions for each scenario considered in this study.

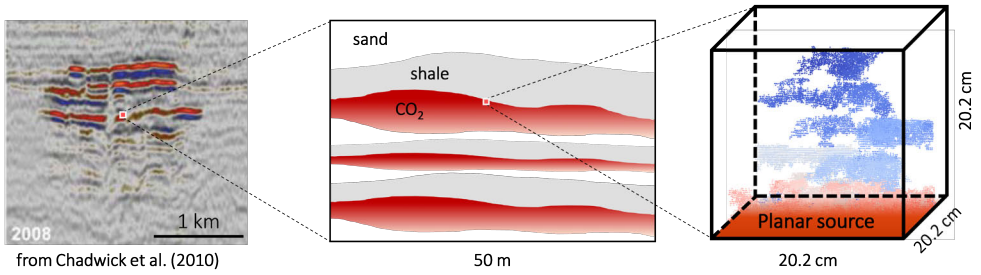

Figure 2.5: Problem conceptualization of the invasion percolation approach. Seismic image of the Sleipner CO_2 plume (left) shows accumulation of CO_2 at high saturations underneath shale layers, which can be simplified to a planar source boundary condition underneath a porous medium at the mesoscale (cm-m).

To exemplify the implementation of lithologic variability into the BAM, Figure 2.6 shows one realization of the P_{th} field applied to four of the eight

REVs considered in this study after being populated with values representative of matrix-laminae case 28 (MUCSa-MUVFSa). Although it is worth nothing that the laminae are very thin (1-3 gridblocks) compared to the bulk thickness of the cross-bedded model (101 gridblocks), we expect that the amount of trapped CO_2 within the laminae will be minimal. In fact, once the average threshold pressure of a lamina is reached by the non-wetting phase pressure building up underneath it, the plume will have enough energy to penetrate and quickly reach the overlying coarser zone (matrix). In other words, the large part of plume trapping is likely to be achieved as a result of the backfilling process within the matrix.

Regarding the variability of threshold pressure distribution within matrix and laminae, no specific correlation structure was applied, although a different seed of the random number generator was automatically assigned to each of the 200 realizations to convert the user-specified PDFs into cell attributes. The numerical grid consists of approximately one million cells with dimensions of $2 \times 2 \times 2$ mm^3, which is analogous to the measurement scale of a probe-permeameter device (Nordahl et al., 2005) and is consistent with the scale at which P_{th} values are accounted for. Closed boundary conditions are applied to all the faces of the numerical domain. To recreate an infinite source of CO_2 at the bottom of the REV, we apply an injection volume 69 times larger than the pore volume (1.65 L, assuming constant porosity of 0.2). Despite the volumetric constrain of the source, however, we disregard any CO_2 volume calculation and emphasize the final distribution of the plume, which

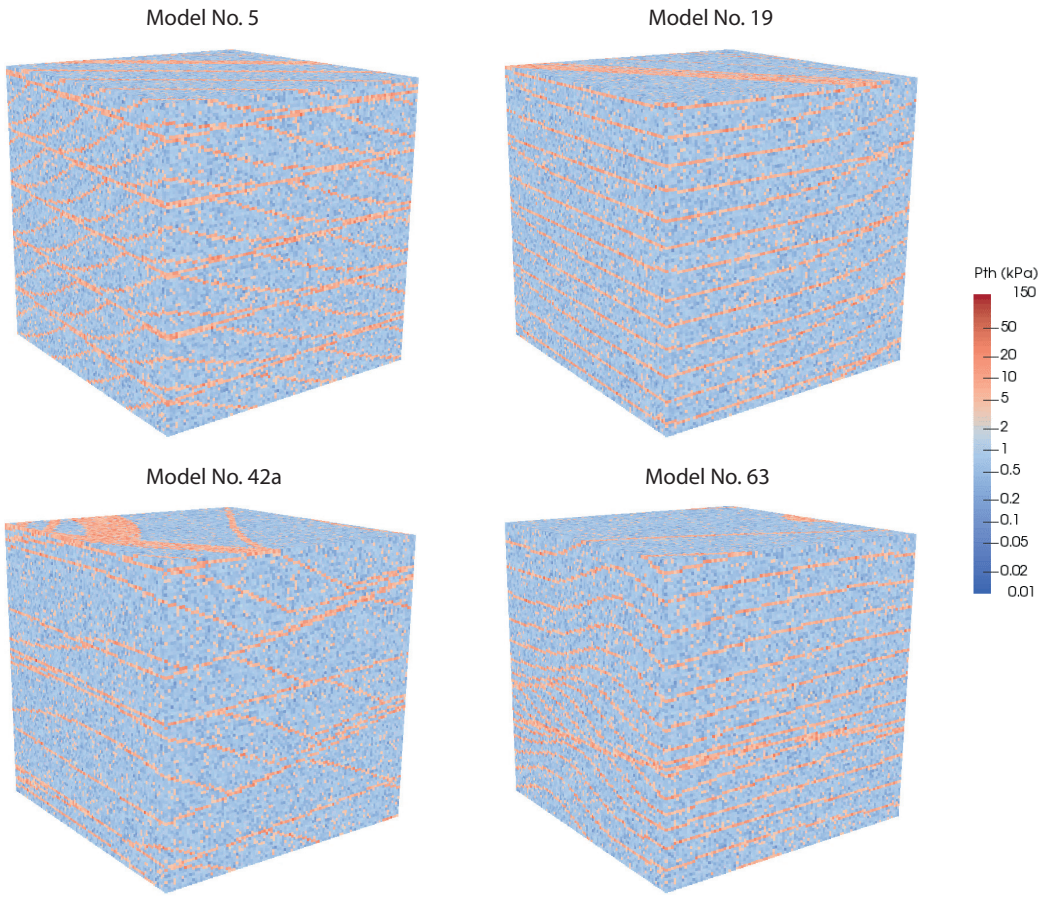

Figure 2.6: Representative Elementary Volumes for four (of eight total) BAMs after being populated with $P_t h$ values sampled from PDF of case 28 (MUCSa-MUVFSa).

will be evaluated in terms of cells invaded at percolation normalized by the total number of cells:

$$\langle S_{CO_2} \rangle = \frac{\text{cells invaded}}{\text{total cells}} \tag{2.10}$$

The stochastic nature of geological heterogeneity requires IP simulations to be carried out across a range of P_{th} fields for each textural contrast scenario. The small computational burden of this modelling approach allows doing so by random sampling the P_{th} PDF and creating 200 equiprobable P_{th} realizations. On the one hand, this methodology permits a quick assessment of the average storage capacity at the REV scale from the knowledge of textural contrast between matrix and laminae facies. On the other hand, the uncertainty of model predictions can be quantified by evaluating the standard deviation of simulation results.

To exemplify the impact of threshold pressure heterogeneity on plume migration, IP simulation results in Figure 2.7 show CO_2 distribution at percolation for one P_{th} field realization (random seed=1234) and three different textural contrasts applied to BAM 5, 36 and 63. Despite the lack of time-dependence of the IP method, invasion sequences such as the ones presented in Figure 2.7 can give insights into the predominant processes controlling CO_2 distribution within the porous medium, such as migration via low-saturation stringers or trap backfilling at higher saturation.

Although limited to three cases, Figure 2.7 illustrates the influence of

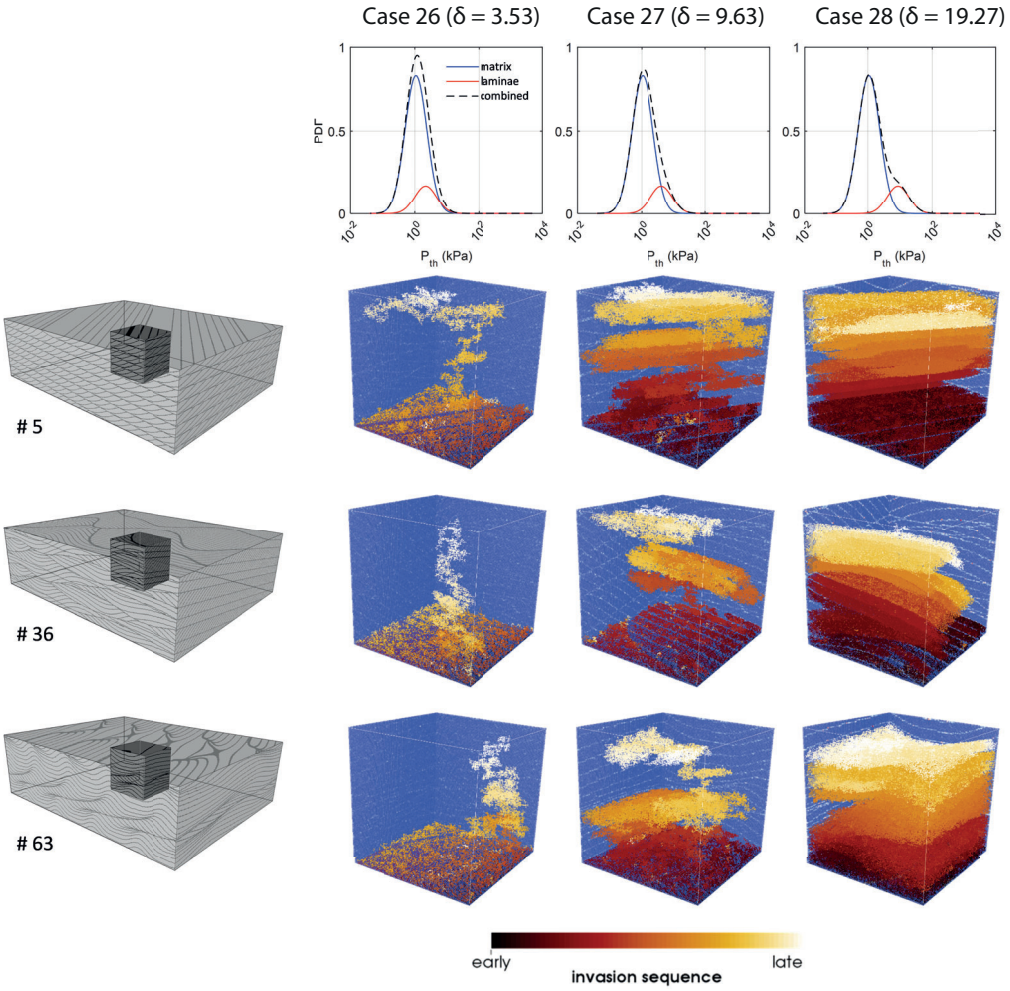

Figure 2.7: Pth fields of matrix and laminae lithofacies populated following the corresponding PDF shown in Figure 2.3. The increasing textural contrast represented by δ leads to different responses in terms of displacement patterns and plume trapping as can be observed from invasion sequences of CO_2 across the three models.

P_{th} PDF overlap (Figure 2.3) on the magnitude of the baffle effect exerted by the laminae over the final CO_2 distribution. As one can expect by intuition, more local capillary trapping will be observed in cases with more separation between P_{th} PDFs of matrix and laminae (e.g. case 28). As opposed to the high saturation due to this backfilling behavior, when the overlap between the two PDFs increases (e.g. case 26), the laminae P_{th} distribution will lose correlation and the plume will favor a stringer-like migration. As a matter of fact, this is the overall trend that emerges from IP simulations carried out across a large number of textural contrast combinations. However, as we report in Figure 2.8, the relationship between average model saturation and textural contrast parameter is nonlinear and affected by the spatial arrangement of the laminae.

2.5 Discussion

Following a systematic approach accounting for a wide range of textural contrasts we assessed the hypothesis that the fraction of rock invaded by CO_2 at percolation is correlated with the Pth contrast between matrix and laminae and with the geometry of the sedimentary model. We believe that this approach can lead to more accurate predictive estimates of storage capacity in sedimentary formations with respect to other estimation methods based on static assumptions. The contrast is defined by the parameter introduced in equation 11, which is calculated for the 40 cases mentioned earlier. We are aware of the fact that some extreme cases are geologically unlikely, especially the ones involving laminae with extremely poor grain sorting, which translate

into questionably large variances. Also, in some cases, $\delta > 50$ may be unreasonable from a depositional process perspective. For the sake of completeness and to explore fundamental aspects, however, we included in our analysis a range of contrasts that in some cases may exceed the limits of reality. Figure 2.8 shows the correlation between percentage of model invaded by the plume and the parameter δ, plotted against the average model saturation predicted by equation 14.

$$\{S_{CO_2}\rangle(\delta) = C_4 + \frac{C_1 - C_4}{1 + \left(\frac{\delta}{C_3}\right)^{C_2}} \tag{2.11}$$

The non-linearity of the correlation seems to be well captured by the 4-parameter regression model that constrains the minimum and maximum asymptotes with coefficients C1 and C4, respectively. While coefficient C1 has no role in differentiating the eight BAMs, the maximum average model saturation represented by coefficient C4 shows higher variability and a strong dependence on the depositional architecture of the geological model. Interestingly, the influence of each architecture is manifested at textural contrasts denoted by $\delta > 3$, which can be related to differences in median grain sizes between matrix and laminae ranging from about 0.4 mm (e.g. between EWUCSa and EWUMSa) to about 0.7 mm (e.g. between PUCSa and PUMSa). Similar contrast in grain size have been observed by Meckel (2013) in sedimentary relief-peels from fluvial depositional environments.

Given the strong anisotropy of the medium, we can expect considerably

	Min. saturation asymptote (C1)	Slope Factor (C2)	Inflection Point (C3)	Max. saturation asymptote (C4)	R2
No. 3	3.23	5.11	3.49	72.43	0.97
No. 5	2.88	4.04	2.69	51.84	0.92
No. 13	3.25	3.71	2.82	57.75	0.94
No. 19	3.03	5.12	3.51	48.68	0.96
No. 27	3.07	3.62	2.69	36.15	0.90
No. 36	2.48	4.37	2.71	36.08	0.88
No. 42a	2.74	4.17	3.08	68.59	0.97
No. 63	2.72	4.05	3.02	69.53	0.98

Table 2.1: Fitting parameters for the regression model and coefficient of determination for each bedform model. R2 values are estimated using mean square errors between regression model and average IP simulation results, represented by points in Figure 2.8

different saturation trends if the CO_2 flow direction is parallel or sub-parallel to the laminae. However, we consider that a sub-horizontal orientation of the sedimentary model represents the most common scenario encountered in the subsurface to include in our simulations.

Overall, the predictions of the non-linear parametric model indicate a satisfactory fit with the average number of cells invaded by the plume calculated from 200 realizations for each matrix-laminae case, leading to coefficients of determination between 0.9288 and 0.978 (Table 2.1). Regardless of the metric used to characterize the statistical distance between PDFs of matrix and laminae, this study aims at identifying trends in trapped CO_2 volumes as a function of textural contrast and bedform architecture.

As can be observed from Figure 2.8, average saturations follow a scattered distribution, especially at high textural contrasts between matrix and

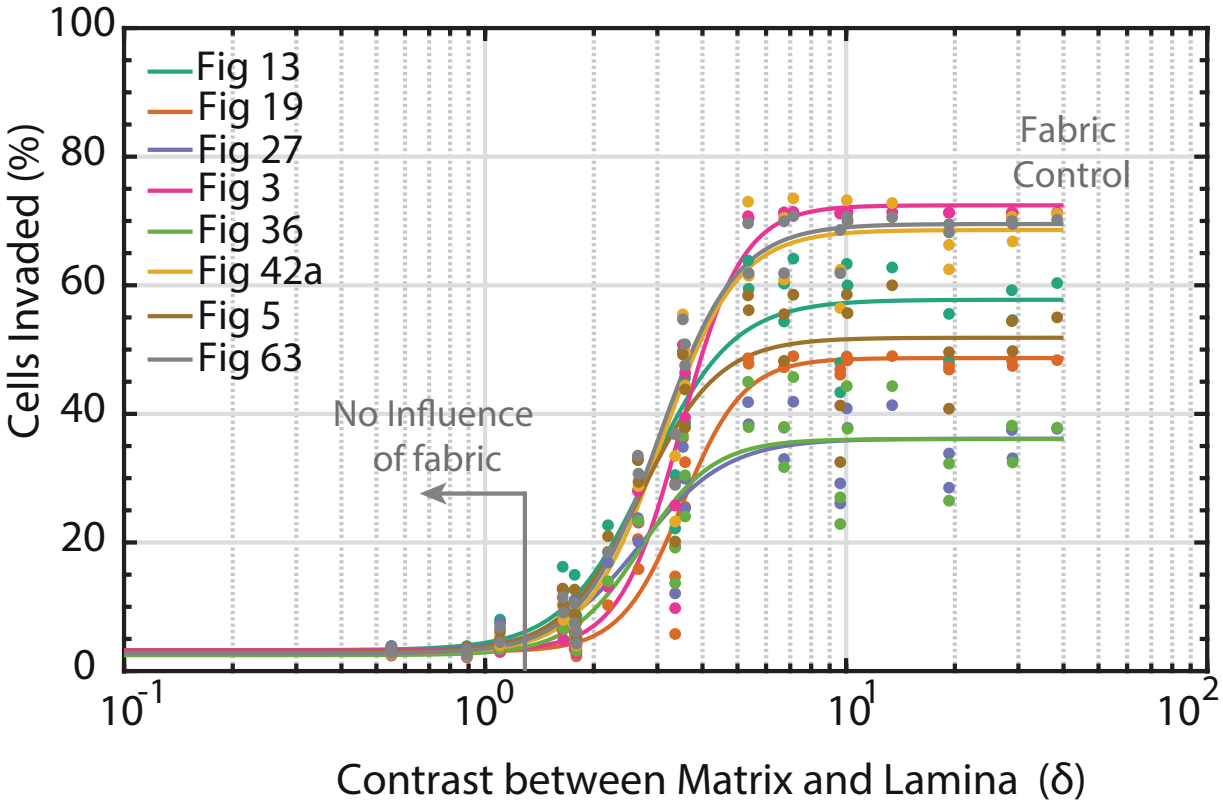

Figure 2.8: Influence of Pth contrast between matrix and laminae on average model saturation (expressed as percentage of cells invaded by CO_2 plume).

laminae. In an attempt to understand this poorly constrained behavior, we analyze the effect of Pth PDF on the percentage of cells invaded by the plume by breaking down the results into each grain sorting category (Figure 2.9). The resulting plot shows how each sorting category affects the distribution of the results along the x-axis, where higher standard deviations (e.g. Poorly Sorted) constrain the results to lower contrast values. Remarkably, the Extremely Well Sorted category follows a trend that is quite separated from the rest of the data. This tendency suggests that 1) the parameter δ does not integrate all the factors affecting the average model saturation over the entire range of textural contrast, and 2) the scarce overlap between matrix and laminae Pth PDF due to small standard deviations generates saturation trends that do not reach stable plateaus within realistic textural contrasts.

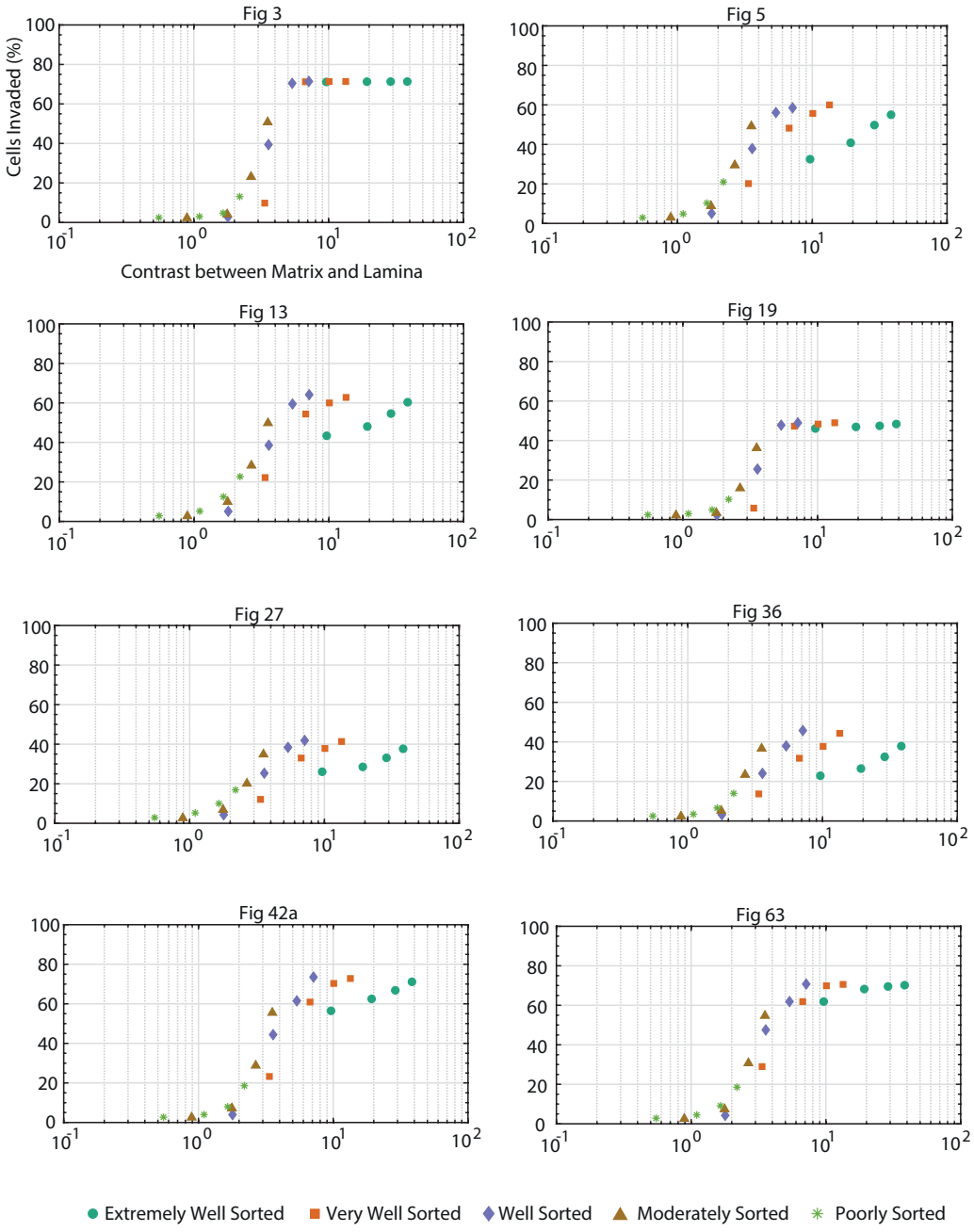

Figure 2.9: Average model saturation results for all models showing different trends corresponding to each sorting category.

2.6 Conclusions

The ability to anticipate fluid saturations resulting from buoyant flow in heterogeneous clastic materials has been greatly advanced through this research. It is clear that the contrast in average grain size between matrix and laminae (overall degree of lithologic heterogeneity) can have a profound influence on CO_2 saturation. The range of saturation from a homogenous sand (low matrix-laminae Pth contrast; $\delta < 3$) to a similar architecture but with large contrast ($\delta > 20$) could be as much as 30 or 40%. Sedimentary descriptors such as grain size and bedform architecture can be related to depositional environments, which are typically inferred from well log (Gamma, SP) motifs in the subsurface. The presented work is an effort to understand the influence of bedform-scale (cm-to-m) heterogeneity on CO_2 saturation in geological reservoirs experiencing buoyant fluid flow. By means of IP simulations through three-dimensional sedimentary models we considered a range of possible textural contrasts with the goal of detecting trends in trapping behavior. Ultimately, the fraction of trapped CO_2 plume is revealed to be controlled by both sedimentary architecture and Pth contrast between matrix and laminae. We suggest that anticipated saturations of candidate reservoirs can be constrained using diagnostic descriptive sedimentology criteria related to interpreted depositional environments.

These saturation results have significant implications for CO_2 storage capacity assessment. Van der Meer (1992) recognized that the CO_2 storage process is "affected by many individual mechanisms: fluid properties at reser-

voir conditions, specific conditions of the rock matrix and depositional environment of the geological formation". Further, he noted that mobility aspects would reduce the pore volume accessed by the CO_2, a concept termed theoretical effective pore volume and eventually codified as storage efficiency (typically represented as 'E'). In his early work, Van der Meer (1992) assumed that perhaps 2% of the total pore volume would be accessed by the CO_2, although the determination of that factor was informal until Van der Meer (1995) formalized it. This concept of storage efficiency has been arguably the most debated aspect of storage capacity assessment since then. These early concepts are reflected in the early capacity work in both Canada (Bachu et al., 1994), USA (Bergman and Winter, 1995), and in every regional storage capacity atlas developed since (where E is typically quite low). The saturations we present for small-scale heterogeneous models are not appropriate for applying to regional assessments (too much lithologic heterogeneity at coarse stratigraphic scales), but are likely to be useful for understanding reservoir-scale performance. Small scale heterogeneity may elevate saturation well above 5%, and is likely to be instrumental in limiting long-term migration.

2.7 Limitations

The principal limitation with the Invasion Percolation implementation in Permedia is that only drainage can be modeled. Invasion Percolation itself was developed for simulating drainage. Imbibition usually is described by a site percolation algorithm. What that means for these results is that the

subsequent imbibition of the in-situ brine post invasion of CO_2 is not accounted for here. Thus the values reported in this chapter are not really "trapped" saturations. Some of this trapped non-wetting phase will be displaced during natural imbibition/ redistribution. We will revisit this aspect in Chapter 4.

2.8 Retrospective on REV

Figure 2.9 shows that in some models, the non-wetting phase saturations at high contrasts do not plateau and thus cannot be described by the regression model. To understand this anomaly, we repeated the entire set of flow simulations on the full scale model ($495 \times 400 \times 142$ cells). The ensemble results show similar behavior and could be described using a 4 parameter regression model albeit with different fitting parameters. This result is shown in Figure 2.10.

Overall we find that the fitting model is able to constrain the results better. Some of the models however, stabilize at saturations much lower than that in the REV scale simulations. Remarkably we find that these four models: No 13, 5, 27 and 36 are the ones that showed a lot of scatter in the REV scale. The commonality between these figures is that they all display inclined cross bedding like features. When the REV is extracted, the inclination of the bedding layers is curtailed. This combined with the closed boundary conditions limits the horizontal up-dip direction the CO_2 can travel. In the full scale simulations, it travels further up-dip and is able to build more buoyancy head quickly, thereby resulting in lower saturations at percolation. Thus, we find

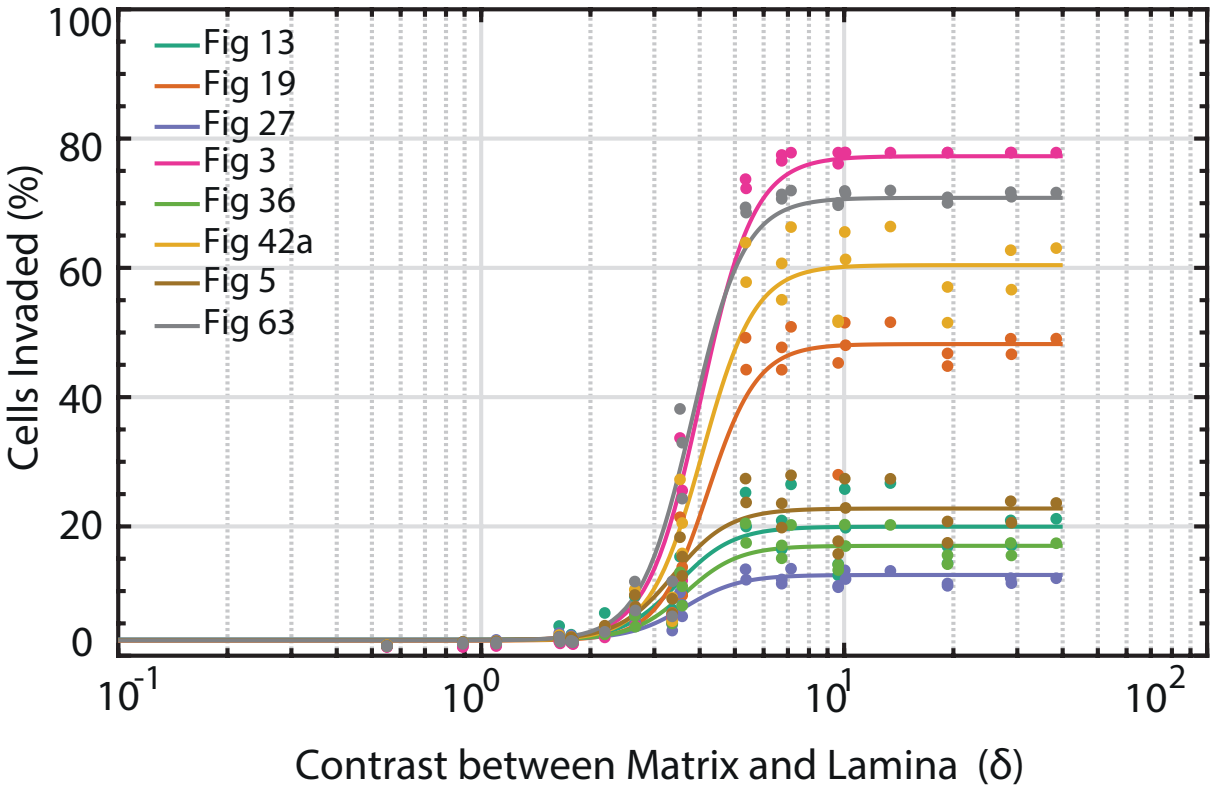

Figure 2.10: Influence of Pth contrast between matrix and laminae on average model saturation (full scale) (expressed as percentage of cells invaded by CO_2 plume).

that determining the correct REV scale for such capillary dominated flows is challenging and cannot be based on static rock properties like porosity, permeability or matrix to laminae ratio. Further, the presence of an inclined bedding layer does not always result in lower saturations. We discuss this with an example in Chapter 4.

2.9 Saturation versus Cells Invaded

The results from the invasion percolation simulations (Figure 2.8 to 2.10) were presented as cells invaded divided by the total number of cells. To make comparison of these results easier with experiments and other similar studies, we attempt to convert cells invaded into CO_2 saturation. As discussed in section 2.4, in the MIP formulation used in Permedia, the invaded cells are considered to be of two types- accumulations and pathways. The accumulations have the maximum possible saturation (1-S_{wr}) while the pathway cells have the minimum saturation required to form a spanning cluster (S_{or}). Since the number of accumulation cells are much larger than that of pathways, in our calculations we assume all the invaded cells to be of the former type. Thus to obtain saturation values, we simply multiply the fraction of cells invaded with (1-S_{wr}). Since the library of lithofacies used to populate the BAMs consist of unconsolidated sands, their porosities are high ($>$0.3) and hence have low ($<$0.15) irreducible water saturations (Holtz, 2002). We conservatively picked 0.2 as the S_{wr} in our calculations. Figure 2.11 shows these results.

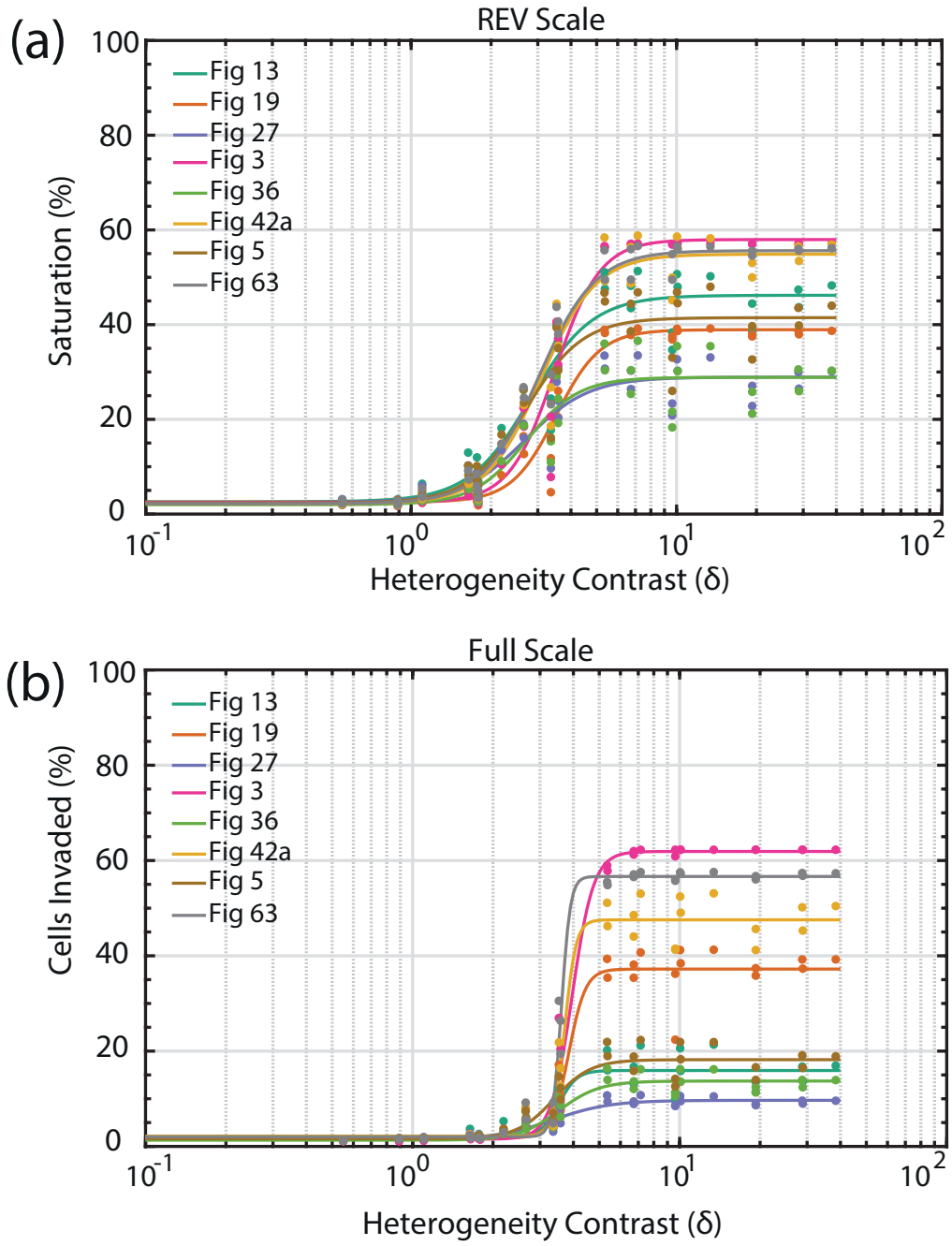

Figure 2.11: Influence of Pth contrast between matrix and laminae on average model CO_2 saturations at (A) REV Scale and (B) Full Scale

2.10 Appendix

Case No	δ (-)	Average cells invaded (%)							
		# 3	# 5	# 13	# 19	#27	# 36	# 42a	# 63
1	0.00	2.61	2.61	2.61	2.61	2.61	2.61	2.61	2.61
2	9.63	71.15	32.51	43.36	46.09	26.07	22.87	56.45	61.88
3	19.27	71.27	40.81	48.05	46.89	28.52	26.50	62.48	68.23
4	28.90	71.30	49.78	54.59	47.45	33.10	32.45	66.81	69.53
5	38.40	71.33	55.01	60.35	48.36	37.67	37.85	71.12	70.18
6	9.63	71.27	41.30	47.94	46.88	29.19	27.02	62.40	68.61
7	19.27	71.31	49.59	55.55	47.39	33.84	32.27	66.29	69.49
8	28.77	71.34	54.42	59.23	48.37	37.49	38.18	70.66	69.99
9	0.00	2.14	2.14	2.14	2.14	2.14	2.14	2.14	2.14
10	3.36	9.78	20.16	22.18	5.77	12.09	13.68	23.26	28.96
11	6.73	71.23	48.24	54.36	47.26	32.99	31.72	60.90	61.89
12	10.09	71.36	55.67	59.99	48.33	37.83	37.70	70.29	69.90
13	13.41	71.37	60.00	62.77	48.98	41.35	44.32	72.79	70.58
14	3.36	25.75	29.14	30.49	14.73	19.38	19.21	33.45	36.83
15	6.73	71.35	55.51	60.25	48.18	37.86	37.97	70.47	69.93
16	10.04	71.42	58.57	63.33	48.92	40.85	44.33	73.22	70.68
17	0.00	2.01	2.01	2.01	2.01	2.01	2.01	2.01	2.01
18	1.79	2.77	5.08	5.09	2.29	4.29	3.17	3.98	4.27
19	3.58	39.43	37.89	38.58	25.54	25.33	24.05	44.41	47.54
20	5.37	70.46	56.13	59.45	47.80	38.38	37.95	61.48	61.88
21	7.14	71.41	58.53	64.16	48.97	41.89	45.73	73.52	70.75
22	1.79	3.65	7.60	8.60	3.07	5.76	4.39	6.04	6.16
23	3.58	46.38	43.79	45.61	32.50	29.91	30.45	49.55	50.84
24	5.35	70.75	58.42	63.85	48.65	41.83	44.99	73.00	69.64
25	0.00	1.99	1.99	1.99	1.99	1.99	1.99	1.99	1.99
26	0.89	2.21	2.96	2.70	2.14	2.63	2.31	2.52	2.54
27	1.77	4.10	8.83	9.91	3.38	6.86	5.17	7.18	7.41
28	2.66	23.08	29.43	28.29	15.85	20.09	23.37	28.78	30.71
29	3.53	50.75	49.23	49.78	36.22	34.86	36.64	55.48	54.70
30	0.89	2.69	3.70	3.89	2.60	3.77	2.85	3.20	3.44
30	0.89	2.69	3.70	3.89	2.60	3.77	2.85	3.20	3.44
31	1.77	6.03	12.67	14.97	5.19	11.05	7.49	10.29	10.53

32	2.65	28.02	32.86	32.80	20.54	23.80	23.35	33.01	33.50
33	0.00	2.27	2.27	2.27	2.27	2.26	2.27	2.27	2.27
34	0.55	2.45	2.90	2.85	2.41	2.87	2.50	2.66	2.82
35	1.10	3.00	4.84	5.20	2.97	5.24	3.44	3.99	4.49
36	1.65	4.77	10.28	12.47	4.91	9.99	6.56	7.97	9.12
37	2.19	13.11	20.97	22.68	10.26	16.88	13.97	18.55	18.53
38	0.55	2.95	3.57	3.89	2.97	3.90	3.07	3.34	3.76
39	1.10	3.84	6.17	8.00	3.93	7.46	4.70	5.28	6.81
40	1.64	6.38	12.74	16.23	7.11	12.83	8.67	10.30	11.47

Table 2.2: Model saturation, expressed as percentage of cells invaded by the plume, averaged across 200 equiprobable Pth field realizations for 40 matrix-laminae cases and eight BAMs.

Case #	Matrix facies		Laminae facies		Case #	Matrix facies		Laminae facies	
	m. (kPa)	*s.d.* (kPa)	*m.* (kPa)	*s.d.* (kPa)		*m.* (kPa)	*s.d.* (kPa)	*m.* (kPa)	*s.d.* (kPa)
1	*EWUCSa*		*EWUCSa*		21	*WUCSa*		*WUCSi*	
			0.5837	0.0420		0.6274	0.2521	9.9434	3.9955
2			*EWUMSa*		22	*WUMSa*		*WUFSa*	
			1.1673	0.0841				2.5095	1.0084
3			*EWUFSa*		23			*WUVFSa*	
	0.5837	0.0420	2.3346	0.1682				5.0191	2.0168
4			*EWUVFSa*		24	1.2548	0.5042	*WUCSi*	
			4.6692	0.3364				9.9434	3.9955
5			*EWUCSi*		25	*MUCSa*		*MUCSa*	
			9.2503	0.6664				0.7906	0.7266
6	*EWUMSa*		*EWUFSa*		26			*MUMSa*	
			2.3346	0.1682				1.5813	1.4532
7			*EWUVFSa*		27			*MUFSa*	
	1.1673	0.0841	4.6692	0.3364				3.1626	2.9065
8			*EWUCSi*		28	0.7906	0.7266	*MUVFSa*	
			9.2503	0.6664				6.3252	5.8130
9	*VWUCSa*		*VWUCSa*		29			*MUCSi*	
			0.5946	0.1239				12.5310	11.5163
10			*VWUMSa*		30	*MUMSa*		*MUFSa*	
			1.1893	0.2477				3.1626	2.9065
11			*VWUFSa*		31			*MUVFSa*	
	0.5946	0.1239	2.3786	0.4955				6.3252	5.8130
12			*VWUVFSa*		32	1.5813	1.4532	*MUCSi*	
			4.7571	0.9909				12.5310	11.5163
13			*VWUCSi*		33	*PUCSa*		*PUCSa*	
			9.4245	1.9631				1.2875	2.5397
14	*VWUMSa*		*VWUFSa*		34			*PUMSa*	
			2.3786	0.4955				2.5749	5.0794
15			*VWUVFSa*		35			*PUFSa*	
	1.1893	0.2477	4.7571	0.9909				5.1499	10.1587
16			*VWUCSi*		36			*PUVFSa*	
			9.4245	0.2477		1.2875	2.5397	10.2998	20.3175
17	*WUCSa*		*WUCSa*		37			*PUCSi*	
			0.6274	0.2521				20.4052	40.2516
18			*WUMSa*		38	*PUMSa*		*PUFSa*	
			1.2548	0.5042				5.1499	10.1587
19			*WUFSa*		39			*PUVFSa*	
	0.6274	0.2521	2.5095	1.0084				10.2998	20.3175
20			*WUVFSa*		40	2.5749	5.0794	*PUCSi*	
			5.0191	2.0168				20.4052	40.2516

Figure 2.12: Summary of statistical properties (on arithmetic scale) of Pth PDF of matrix and laminae for the 40 matrix-laminae cases. Thick lines delimit subsets with common matrix facies.

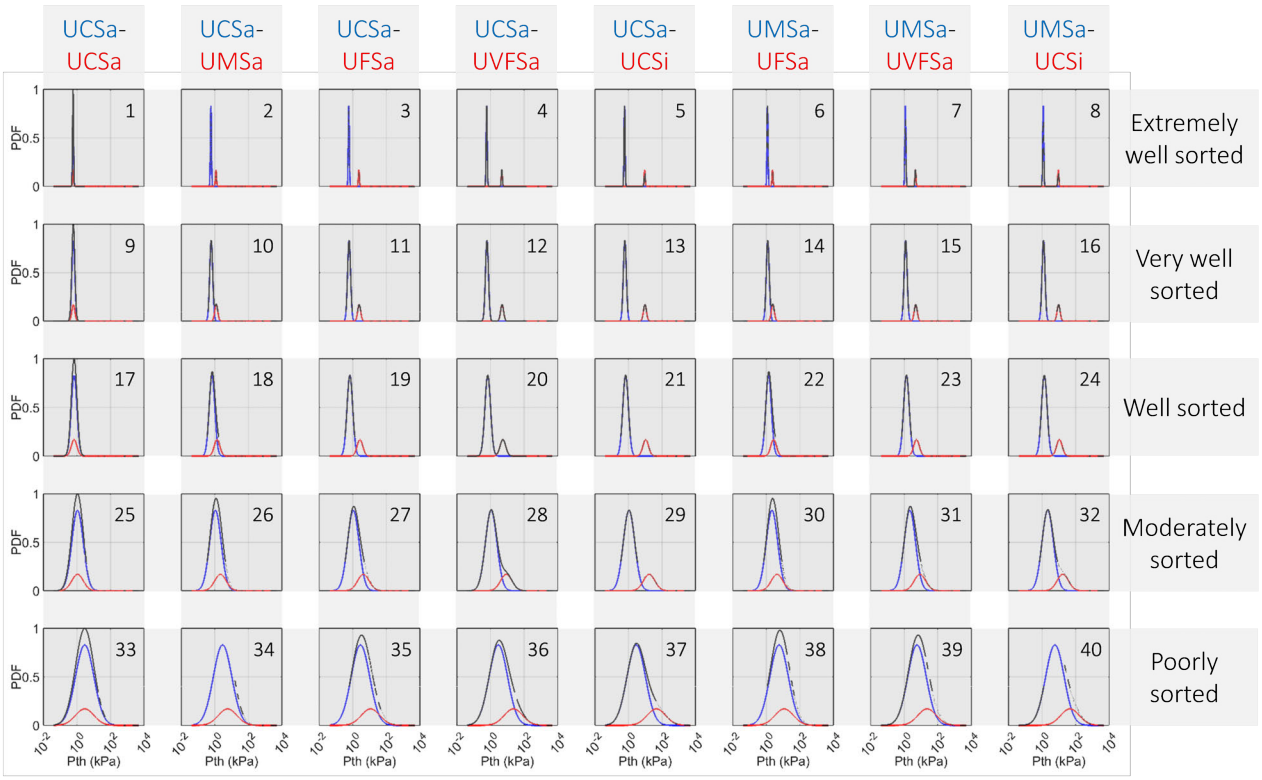

Figure 2.13: Probability density functions (PDF) of threshold capillary pressure (Pth) for the 40 matrix-laminae cases presented in this study. Five different sorting categories are displayed along rows (better sorting translates into smaller variances and narrower curves), while eight different textural contrasts between matrix (in blue) and laminae (in red) are shown along columns. Black dashed lines represent the combined PDF.

Chapter 3

Mimicking Geologic Depositional Fabrics for Multiphase Flow Experiments

In the previous chapter, we used high resolution numerical simulations to correlate heterogeneity with invaded saturations. In this chapter we introduce the methods developed to perform flow experiments analogous to our modeling studies to verify those results.

3.1 Introduction

Clastic subsurface aquifers and reservoirs are characterized by geologic heterogeneity that occurs over a wide range of length scales (Murphy et al., 1984), presenting a major challenge in predicting flow in the subsurface. Small scale (mm to dm) depositional fabrics such as ripple laminae and cross-beds have been widely recognized as important controls on subsurface fluid transport (Ringrose and Bentley, 2015). These features are a reflection of grain size variability that arise due to periodic fluctuations in depositional processes.

Based on "Mimicking Geologic Depositional Fabrics for Multiphase Flow Experiments", PG Krishnamurthy, TA Meckel and D DiCarlo ,Water Resources Research, 55, 9623 (2019) PGK designed and conducted the research and wrote the manuscript.

The fluctuations in grain size create local heterogeneity in properties such as porosity, permeability, and threshold capillary entry pressure. If clastic material with different grain size distributions are deposited in close proximity, large contrasts in capillary entry pressures can occur over short distances (Corbett et al., 1992). As a consequence, small scale heterogeneties such as laminae (mm to cm) and bedding (cm to dm) become especially important in the dynamics of multiphase flow (CO_2/Oil/NAPL-Water) and can further impact reservoir and aquifer flow behavior (Hartkamp-Bakker, 1991; Saadatpoor et al., 2010; Glass et al., 2000). The effect of capillary pressure gradients due to heterogeneities at such scales becomes accentuated in specific flow regimes: small capillary number and low velocity flows where the viscous and buoyancy forces are comparable or smaller than capillary forces.

Several studies (Kortekaas 1985; Weber, 1982; Ringrose et al., 1993) have shown how textural heterogeneities strongly influence non-aqueous phase migration pathways and saturation distribution during multiphase flows in the subsurface. While small scale heterogeneities gained attention initially in the context of how they affect oil recovery (Huang et al., 1996), subsequent studies shifted focus toward hydrocarbon migration (Ringrose and Corbett, 1994; Carruthers and Ringrose, 1998) contaminant transport (Glass and Nicholl, 1996), and more recently CO_2 sequestration (Pini and Benson, 2013; Li and Benson, 2015; Trevisan et al., 2017a; Ren, 2017; Jackson et al.,2018).

A few different types of laboratory experimental methods have been used for studying the influence of capillary heterogeneity on fluid flow. In-

termediate scale (dm to m) 2D heterogeneous sand/glass bead packs have been the most widely used. They have been used to study DNAPL migration (Kueper et al., 1989; Illangasekare et al., 1995; Conrad et al., 2002), gravity unstable gas flows (Glass et al., 2000; Ji.et al., 1993; Van De Ven and Mumford, 2018), hydrocarbon migration (Thomas and Clouse, 1995), immiscible oil displacement (Roti and Dawe, 1993; Dawe et al., 2011) and CO_2 migration and dissolution (Trevisan et al., 2014, 2015, 2017b; Rasmusson et al., 2017). Intermediate scale flow experiments represent a convenient method for visualizing and studying the influence of heterogeneity on macro scale immiscible flow dynamics. Using beads or grains of different sizes, structures with heterogeneity contrasts of specific interest can be engineered. However most of these experiments are conducted in macro-heterogeneous media that are constructed by arranging discrete homogeneous units. Natural looking heterogeneity, with variations at a hierarchy of scales, has gone unrepresented in these flow experiments.

Coreflood experiments using whole rock cores and smaller core plugs have been a popular method in oil recovery and CO_2 sequestration research (Krevor et al.,2011, 2012; Reynolds et al., 2018; Krishnamurthy et al., 2017). Rock cores mitigate the principal shortcoming of sandpack experiments in that they incorporate the natural depositional features and have been recovered directly from the reservoirs of interest. The main drawback however is that they are limited by their size ($\sim$2 to 3 inches in diameter) to adequately capture important sedimentary features at the bedform scale (Ringrose et al., 1996).

A few studies have employed thin sandstone slabs (10s of cm wide) instead of cores (Klise et al., 2008; Huang et al., 1995a, 1995b). This method offers a middle ground between the previous techniques and addresses both shortcomings, but poses many experimental and imaging challenges. However neither cores nor slabs offer the capability to customize and engineer the heterogeneity of the porous medium as sandpacks do.

To incorporate realistic geologic textures in sandpacks, Glass and Nicholl (1996) generated media with intra-layer micro-heterogeneities and cross-bedding, by depositing a sand mixture through a funnel at the top of the chamber, and moving it back and forth manually. However the manual technique precluded the ability to generate heterogeneity reproducibly (Lebron and Robinson, 2003). Griffith et al. (2013) automated horizontal movement, thereby allowing the generation of sandpacks with millimeter-scale heterogeneity in a reproducible manner, but the method was limited to only simple horizontal layered media.

In this work we extend and improve the methods of Griffith et al. (2013) to develop a new approach for generating reproducible, "geologically realistic" bead packs for studying heterogeneity and visualizing flow experiments. We construct an apparatus with an automated dual axis (horizontal and vertical) computer-controlled arm to deposit mixtures of sand-sized glass beads in a glass slab chamber. We exploit the spontaneous grain flow segregation and stratification processes that occur when pouring solid grains onto a pile, to mimic geological fabrics that are produced by sedimentary processes. The au-

tomated filler yields beadpacks with grain size variability at multiple scales (mm to dm). By carefully designing custom computer programs for actuator input and anticipating granular flow conditions, a variety of reproducible structures that exhibit realistic macro-heterogeneous features with micro-scale heterogeneity are produced. The ability to generate sandpacks with such features reproducibly enables a systematic investigation of the effect of various grain-controlled petrophysical and fluid properties on multi-phase flow while maintaining the underlying macroscale fabric.

3.2 Particle Flows: Geometry and Pattern Formation in Sedimentary Rocks

Sedimentary rocks often have complex correlated patterns that arise from various geological processes. These patterns and processes are a function of the depositional environment and the forces in play. In this work, we focus on the most commonly observed sedimentary features: ripples and cross strata (Figure 3.1). The length scales of such features considered here (mm to 10s of cm) are characteristic of fluvial, deltaic, and shallow marine environments (Reineck and Singh, 1980).

We briefly review the natural processes that result in these features before describing the methods employed to recreate them in a laboratory setting.

In depositional settings, when water current velocity increases such that the shear rate is large enough, transport of unconsolidated sediment begins. Instabilities in the water-sediment interface during flow cause the formation

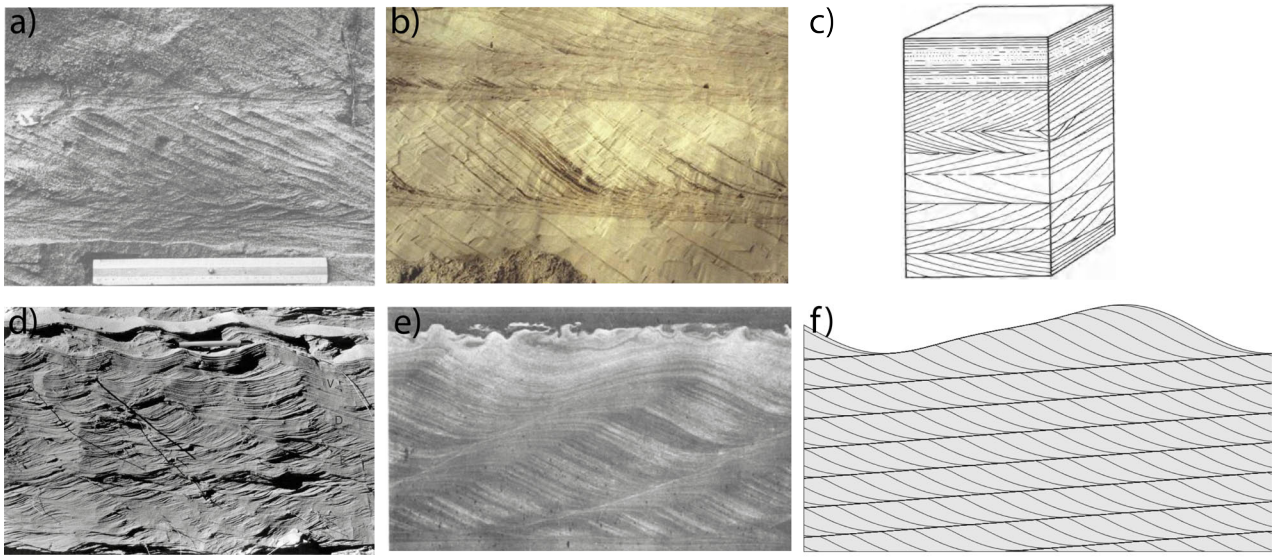

Figure 3.1: Outcrop photographs and conceptual diagrams of sedimentary features mimicked in this work: a) Cross-bedding set formed by ripples (courtesy Allen, 1982b) b) Cross-strata formed by tidal flow (Reesink and Bridge, 2007) c) Herringbone cross-strata (Reineck and Singh, 1980) d) Fluvial ripples (Rubin and Carter, 1987) e) Climbing ripple lamination (Allen, 1982a) f) Climbing cross-stratified bedding (Rubin and Carter, 2005).

of ripples (Reineck and Singh, 1980). Next to the sediment- water interface, exists a fluid layer with a high concentration of sediments also known as the bed load. Further up from the interface, the water mainly consists of suspended fine sediment. As the water flows, the sediments (a mixture of heavy and fine particles) in the particle heavy fluid layer move by rolling, sliding and by bouncing due to impact with other solid grains/surfaces (known as saltation) (Allen, 1982). The movement of sediments in the heavy fluid layer greatly impacts the formation and propagation of ripples. Ripples are formed in the direction of flow and are made up of a gradually upward sloping stoss side and a relatively steep downward facing lee side. The crest of the dune separates the two faces. The sediment laden water flowing along the stoss face gets dissipated at the crest due to boundary layer separation, thereby causing the particles to be deposited. The sediment grains arrive at the crest of the dunes and accumulate high on the lee face, slowly steepening the slope. When the angle of slip is exceeded, failure occurs and the grains avalanche onto the lee side of the dunes. As the sediment is carried over from the upstream to the lee side of the ripple, the result is a gradual migration of the ripple in the direction of flow (Engelund and Fredsoe, 1982). The migration of ripples or dunes in the downstream direction of flow results in the formation of crossbeds. They are characterized by three types of laminae: the foreset laminae is the result of avalanching grains on the lee side of the dunes; the topset and bottomset laminae are due to the settling of suspended fine grains on the stoss side and toe of the lee side of ripples respectively. This is a simplified overview of the

processes that cause the formation of the main structure

The heterogeneities observed in such clastic material has been attributed to the grain sorting and stratification processes that occur during the avalanching of grains down the slope of ripples during their formation and migration (Reineck and Singh, 1980; Kleinhans, 2004; Reesink and Bridge, 2007). Pattern formation during such avalanches has received much attention in the granular matter physics community (Makse et al., 1996). In order to study this phenomenon, numerous studies have emulated the heterogeneities and patterns in the laboratory, by pouring grain mixtures onto a pile between two vertical plates spaced close to each other (Hele-Shaw cell) (Makse et al., 1997c, 1998; Baxter et al., 1998). We use the learnings from these studies to adapt and automate the grain pouring process in order to emulate the crucial avalanching step to obtain decimeter scale crossbed and dune like structures.

3.3 Methods and Materials

3.3.1 Experimental Setup

The experiments were carried out in a 2D square slab chamber (Figure 3.2). The glass slab chamber was constructed using an aluminum frame and glass panels. A 68 cm x 68 cm x 4.5 cm thick slab of aluminum was cut and machined to make the main frame. The frame has viewing windows on the front and back faces (Figure 3.3), and inlet and outlet slits on the top and bottom faces. Two 3/8" thick, low iron, tempered glass panels were fitted onto the windows of the frame. The glass panels and the main frame were sandwiched

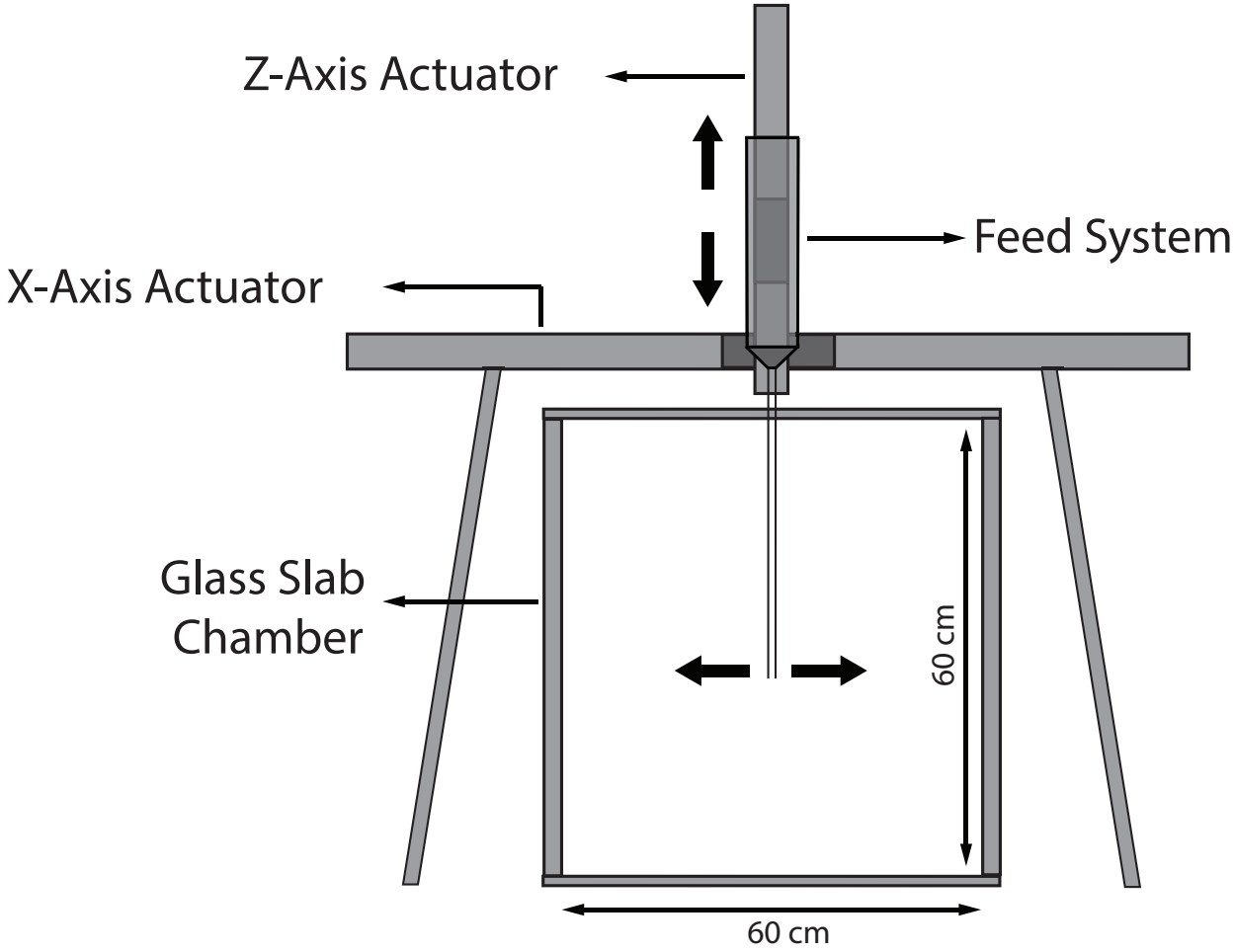

Figure 3.2: Schematic of the automated filling apparatus. The motion is controlled by a computer programming interface.

between two external aluminum frames and clamped together by bolts. A solvent resistant gasket (polyurethane sheet, McMaster Carr) emplaced between the glass panels and metal plates provided the necessary water and airtight sealing. The top and bottom faces were also sealed using gaskets and removable aluminum plates. The bottom and top sealing plates were each provided with five injection and outlet ports (3.175 mm ID, equally spaced). The chamber was mounted using horizontal pivots on a support frame made of struts. The effective internal dimension of the chamber is 60 cm x 60 cm x 2 cm.

The chamber was packed with glass beads using an automated filling apparatus (Figure 3.3). The filling apparatus consists of a pair of belt driven linear actuators (Parker Hannifin) that provide motion in the horizontal axis. One of the actuators was mounted onto the other perpendicularly so as to obtain motion in two axes (X and Z). The actuators are driven by servo motors and controlled by a compumotor that enabled coordinated movement of the two actuators, thereby providing dual axis motion capabilities. The interface between the user and compu-motor is provided by Parker Motion's proprietary program 'ACR-view'. The software interface allowed the user to create programs to control actuator parameters such as the horizontal and vertical extents, velocity, acceleration and pauses, and introduce loops that facilitated complex coordinated motion of the two axes. A mount for the feeder tube and hopper was bolted onto the vertical axis actuator. The feed tube was made of stainless steel (4.5 mm ID) with its top end connected to a funnel via a ball valve. The other end of the tube protruded into the glass chamber. An

acrylic cylinder was attached on top of the funnel to act as the bead reservoir. Inside the hopper was placed, a cylindrical tube with a series of horizontal metal mesh screens (4 mm openings) along its height. When a pre-defined mixture of glass bead sizes was introduced into the hopper from the top, the screens helped reduce segregation and maintained the randomized state of the mixture.

3.3.2 Materials

The porous media used to pack the chamber were translucent glass beads acquired from Potter Industries and MARCO. The bead sizes were characterized to assure specifications using an image based particle analyzer (CAMSIZER, Retsch Technology). The glass bead sizes used in this work along with their properties are shown in Table 1.

Table 3.1: Glass Bead Properties

Glass Bead Type	US Sieve Fraction	Mean Diameter (mm)	Standard Deviation (mm)
Marco Size 4	30-40	0.465	0.075
Marco Size 6	50-70	0.194	0.051
P120	50-70	0.259	0.025
P230	30-40	0.457	0.06
P280	25-35	0.599	0.07
P337	20-30	0.689	0.086
A100	16-20	0.866	0.08

3.3.3 Sample Preparation and Packing

Feed grain mixtures were first created by combining pre-determined volumes of the two differently sized beads in a large bucket. To achieve re-

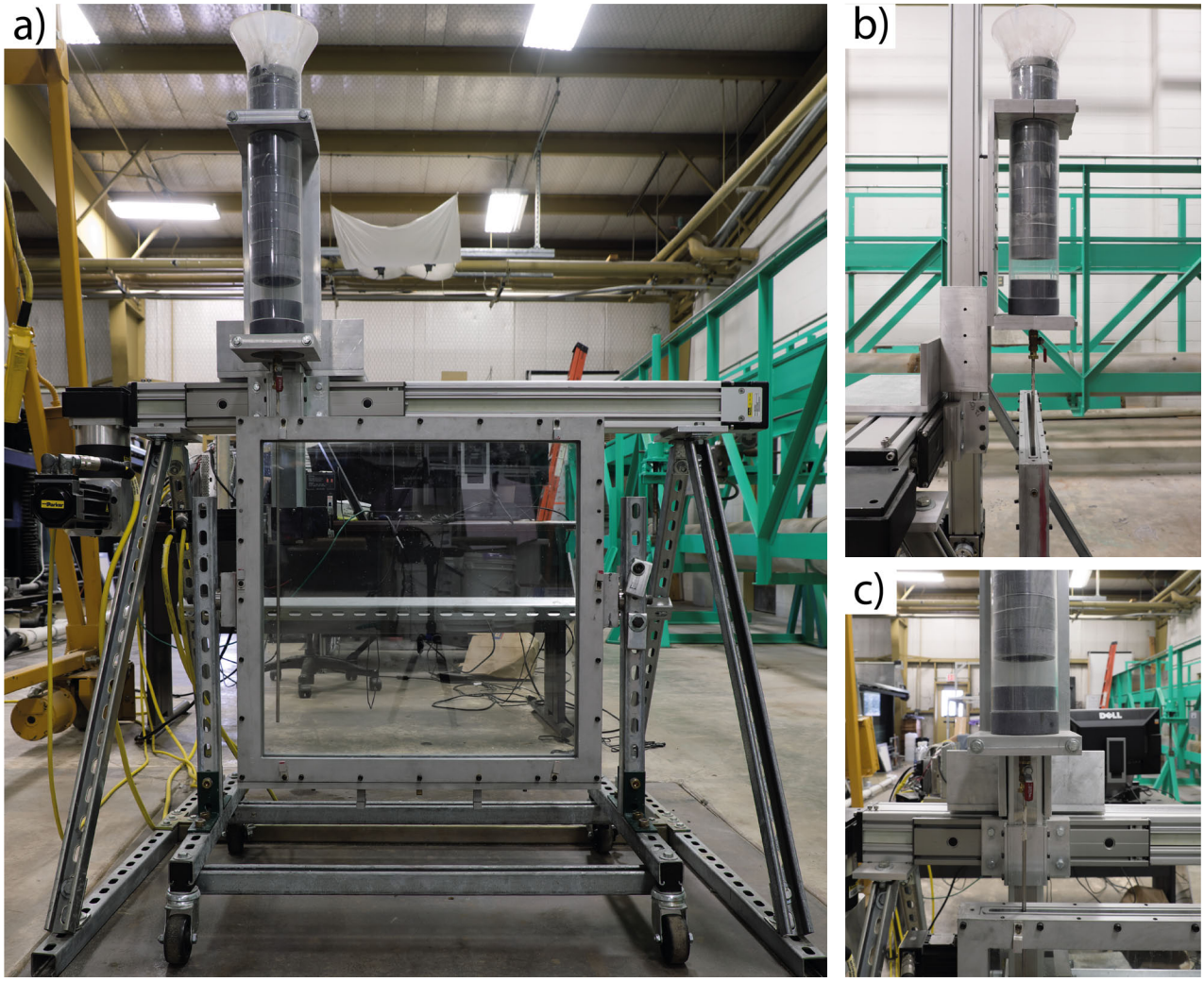

Figure 3.3: Photographs of the experimental setup showing a) Actuator system, glass chamber and feed setup b) Side view showing the feed silo and mesh screens c) Close up of the feed valve.

producible sedimentary fabrics, it is essential that the input mixture be as uniformly mixed as possible. In order to ensure a homogeneous mixture, the bucket was flipped vertically 10 to 15 times. The flipping was done quickly, so that the pouring action, which causes size segregation, is minimized. A 80:20 volumetric ratio of coarse to fine beads was used to make the initial mixture. This volumetric ratio is maintained for all packings reported here. For the various packings generated in this chapter, the mean grain size ratio of the beads ranged from 1.25:1 to 4:1. This mixture was then transferred into the hopper using borosil glass beakers. The mixture container was rapidly inverted into the randomizer attached to the hopper, again to avoid the pouring action. As the beads fell through the horizontal mesh screens, collisions between the beads and mesh ensured that they were continually randomized. Usually the beads were introduced one beaker (500 mL) at a time into the hopper. Additional beads were added when a conical depression began to form in the funnel at the bottom of the hopper. The objective was to minimize the time the beads spend in the hopper funnel before being deposited, limiting opportunity for segregation prior to deposition. If the beads stayed longer in the hopper, size segregation allowed the finer grains to percolate to the bottom (Rosato et al., 1987). From the hopper the beads flow through the feed tube into the glass chamber and fall a distance of five centimeters on the accumulating depositional surface. This falling distance is kept constant using the vertical component of the linear actuator as the chamber is filled in order to maintain similar sorting processes. The size distribution of the mixture dic-

tates the flow rate of grains. After the filling was complete, a rubber mallet was used to tap on the outer glass walls to help compaction and ensure a dense packing.

3.3.4 Image Acquisition

To facilitate visualization, the packed glass chamber was illuminated from behind by a light source. The light source used is a 63.5 cm x 63.5 cm panel (Evo-Lite Industries) made up of LED strips (5700K) on all four edges and a diffuser on the face. The panel was mounted onto the back window of the glass chamber. High resolution digital images of the various bead packs were captured using a 24 megapixel, full frame color CMOS sensor (36mm x 24mm) camera (Sony RX1).

3.4 Results and Discussion

3.4.1 Fabric Generation

3.4.1.1 Cross Stratification

We generated cross strata in the laboratory, mimicking the ripple migration process that forms cross-beds in natural depositional environments, by engineering a moving avalanche of grains, brought about by the horizontal motion of the feed-tube during deposition. Figure 3.4 illustrates the steps involved in the generation of cross-beds and the formation of its characteristic features. The cross-bed generation process consists of 4 main steps: A) Forming a pile at the left edge of the chamber. B) Depositing beads during

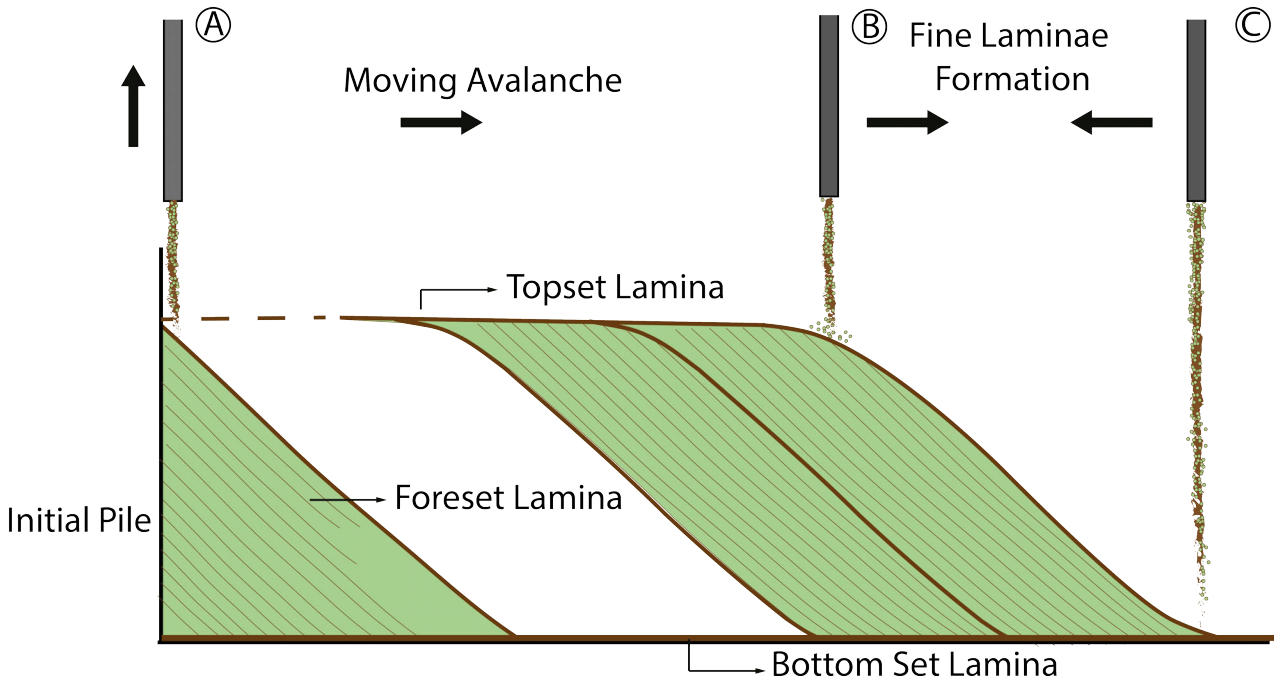

Figure 3.4: Schematic of crossbed generation: A) Formation of the initial pile of beads against the wall. B) Moving avalanche causing the propagation of the bed B-C). The back and forth motion resulting in the formation of the bounding fine foreset laminae.

horizontal migration of the feed tube from left to right C) Short, back and forth motion during periodic intervals, and D) Rastering of the feed tube back to the starting point on the left edge.

In step A, the sloping face of a dune (lee face) was deposited near the left bounding wall of the glass chamber thereby forming a pile. The pile was formed as the bead mixture fell through the feed tube positioned against the left wall. The feed tube was raised up at the rate at which the pile height increased to ensure that the distance between the end of the tube and the surface of the deposited beads remained constant (5 cm).

In step B, with the generated pile of beads as the starting point, the deposition was continued laterally in order to form a bedding layer. A moving avalanche, caused by the deposition of beads as the feed tube moved laterally from left to right, resulted in the migration of the bed (Figure 3.4). Periodic pauses were programmed in, during this horizontal movement of the actuator. After every 2 millimeters of horizontal motion, the feed tube motion was paused for a predetermined period of time (based on flow rate and rate of height buildup). The addition of beads onto the slope of the bed (2 mm away from the apex of the pile) resulted in avalanching of the grains and subsequently the lateral migration of the bed. The pause duration was a function of the height of the bed. Thicker beds needed larger grain volume to build laterally to the same height. The horizontal velocity was maintained at 15mm/sec while the pause duration varied anywhere between 0.3 sec to 1.5 seconds depending on the height of the beds.

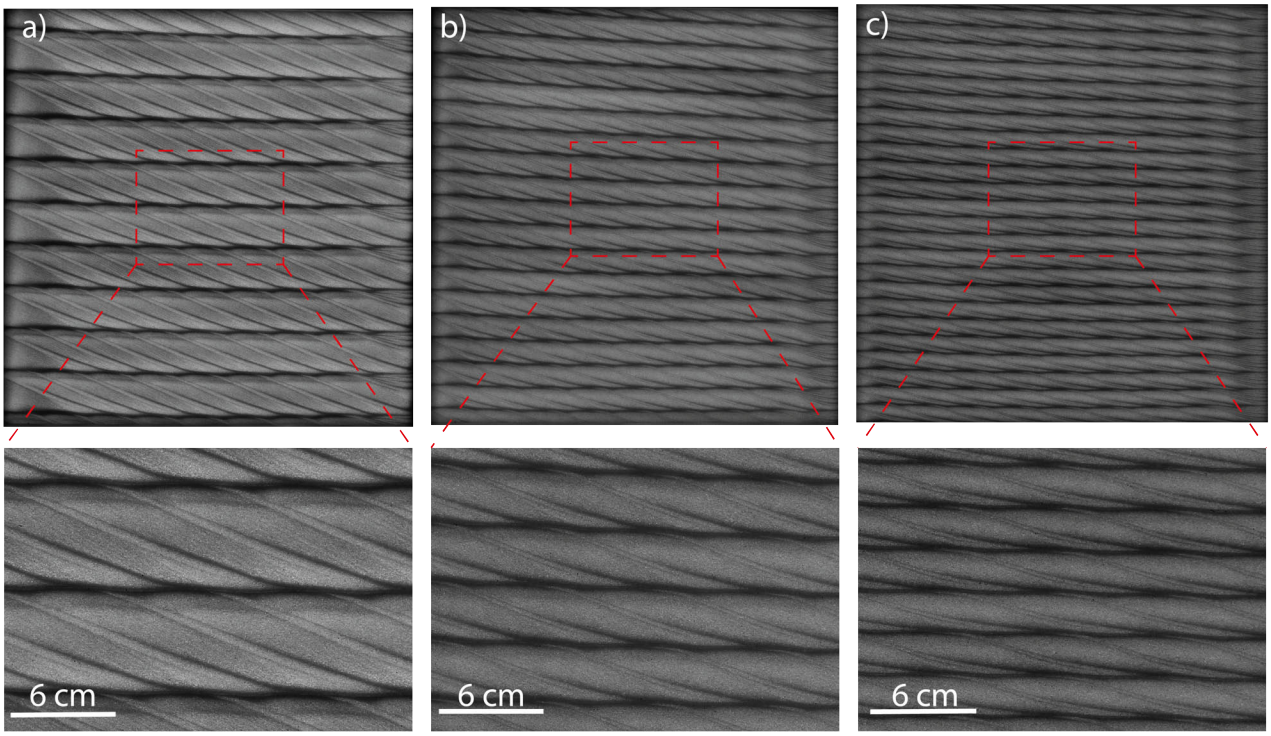

Figure 3.5: Digital images of cross-strata of different bed thickness and laminae concavity generated using the automated filler. In these images the coarse beads (Marco Type 3, Mesh Size 20-30) transmit the most light and hence are brighter; the fine beads (Marco Type 6, Mesh size 40-50) appear dark. Subfigures a) to c) show cross-beds with decreasing thickness and increasing foreset laminae concavity. Magnified section from the center of the packing shown beneath each image. Compare to patterns in Fig 1a-b.

In the third step (C), a periodic, bounding layer of fine-grained foreset lamina (analogous to fine laminae formed due to settling of fine grains in natural environments) was deposited. This was done by moving the feed tube forward to the toe of the slope and back at fixed intervals (Figure 4). This interval was set to 60mm in all the cross-beds in this chapter. The forward movement was at a very high velocity (200mm/sec) and the move back at the normal velocity (15mm/sec) without any pauses. As the beads fell onto the surface, two sublayers were deposited: a fine grained bottom layer and a coarse grained top layer. The thickness of the layers was a function of the velocity of motion. Thus the thicker fine layer formed during the reverse movement acted as the fine foreset lamina. Significant saltation was also observed during the deposition process owing to the momentum of the beads as they hit the surface. The fine bead layer deposited during saltation contributed to the formation of topset and bottomset laminae.

Finally, in step D, once the feed tube reaches the right edge of the chamber, it was brought back to the left edge and the deposition of the next layer began. All the steps were programmed in software interface (ACR-view) and the deposition of the pack was done in one go without pauses.

By manipulating the process parameters that dictate steps A-D, different kinds of cross-beds could be generated. Grayscale transmitted light images of the different cross-beds generated using our technique are shown in Figures 3.4 and 3.5 (for comparison see Figure 3.1a,b). Beds of different thickness were generated by adjusting the height of the initial pile and the pause period

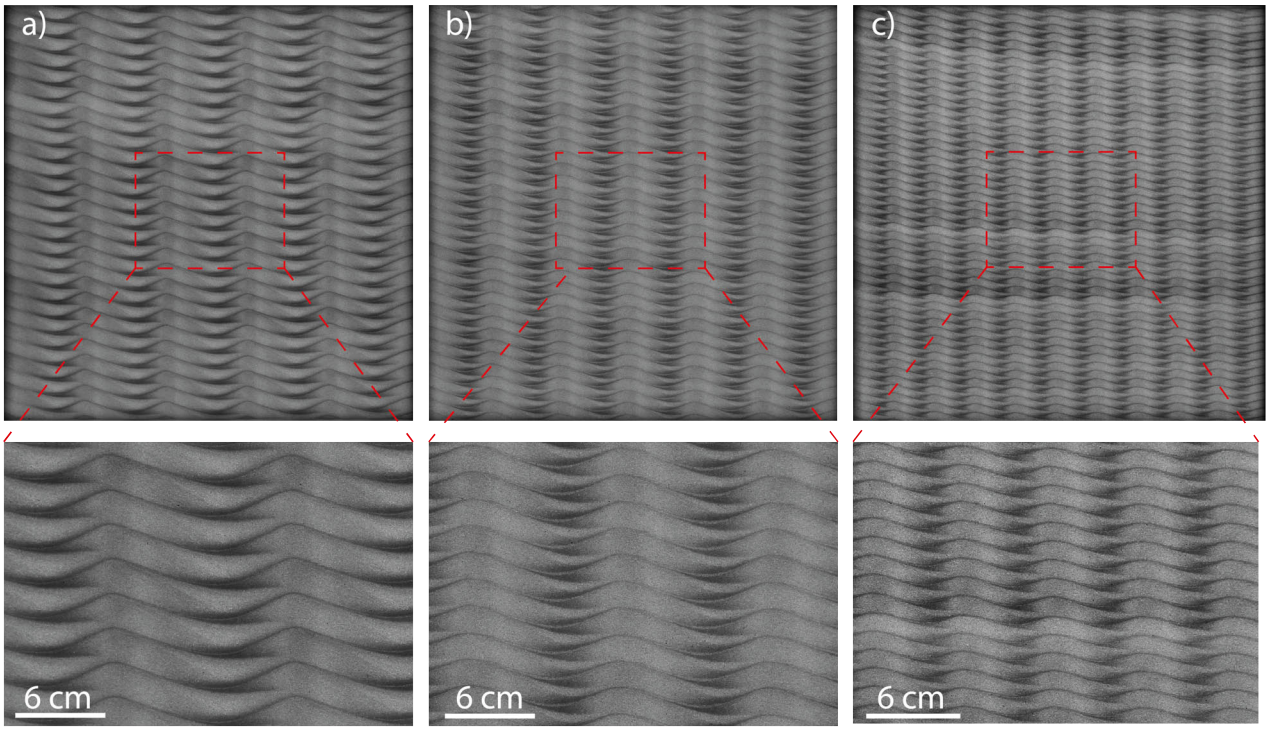

Figure 3.6: a) Climbing cross-beds (Coarse: Marco 20-30, Fine: Marco 40-50) b) Herringbone cross-strata (Coarse: Marco 20-30, Fine: Potter 50-70) c) Climbing ripple laminae (Coarse: Marco 20-30, Fine: Marco 40-50). Magnified section from the center of the packing shown beneath each image. Compare to patterns in Fig 1c,e-f.

during the lateral motion. The length of the forward motion decided the slope of the fine foreset laminae. By travelling farther than the toe of the bed, fine foreset laminae with increasing concavity could be generated. Climbing cross-beds (Figure 3.1f) were generated by depositing upward sloping bedding layers by gradually increasing the pause duration along the length of the bed (Figure 3.6a). Herringbone cross-strata (Figure 3.1c) were generated by alternatingly reversing the direction of deposition (Figure 3.6b). In these images, regions with the coarser material are bright since they allow light to be transmitted compared more easily compared to the fine grained sections.

3.4.1.2 Ripple Lamination

Ripple laminae were generated in two different ways. Asymmetric laminae were generated by modifying Steps A and B from the procedure used for cross-beds (Figure 3.4). Starting with an initial pile with a height equal to the amplitude of the ripples (Step A), the lateral motion was continued with very short pause intervals (Step B). At distances corresponding to the wavelength of the ripples, the pause duration was increased so that beads can accumulate to form a crest (Figure 3.7a). To generate symmetric ripples (Figure 3.1d), the lateral motion between the crests was programmed to be continuous without intermittent pauses . Wavelength and amplitude of the ripples could be changed easily (Figure 3.7b & c). Climbing ripples (Figure 1e) were generated by progressively depositing symmetric ripples slightly out of phase from the previous layer (Figure 3.7c).

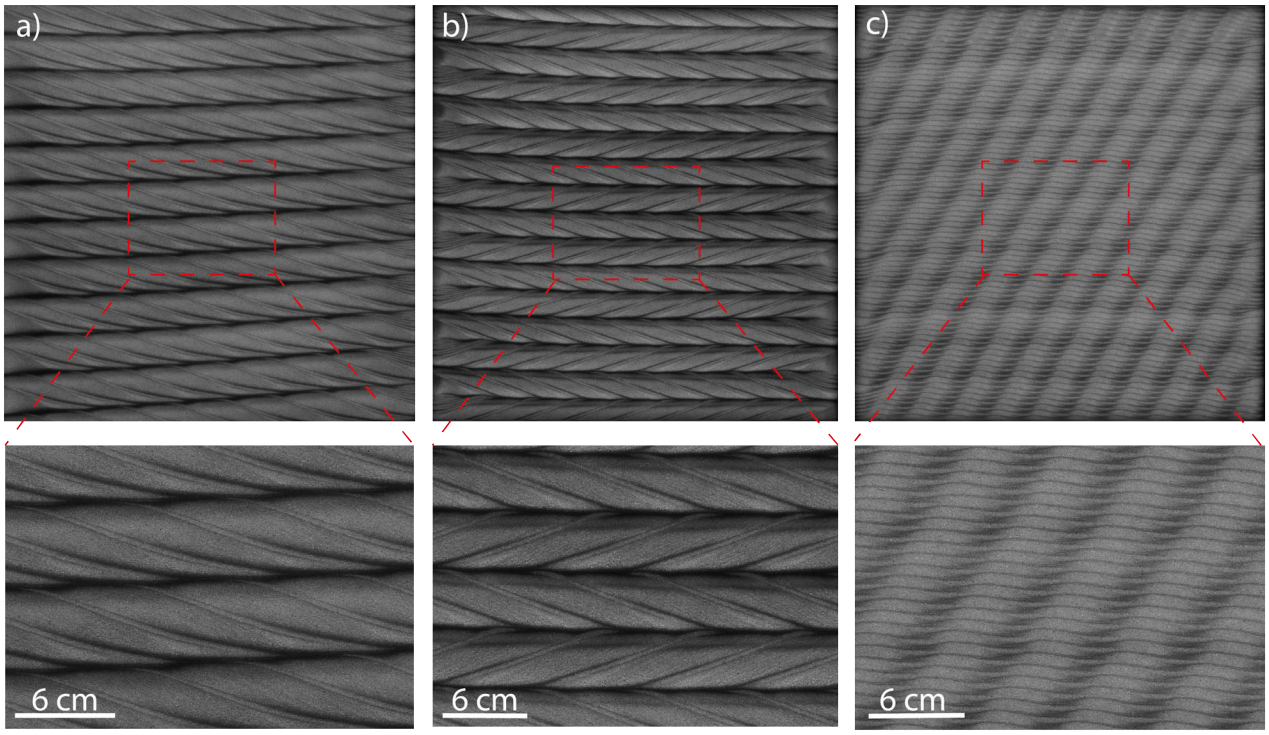

Figure 3.7: Ripple laminations generated using the automated filler. In all cases Marco 20-30 was used as the coarse fraction and Marco 40-50 as the fine fraction in the volumetric ratio of 80:20. a) Asymmetrical ripples b) & c) Symmetric ripples with decreasing amplitude and wavelength. Magnified section from the center of the packing shown beneath each image. Compare to patterns in Fig 1d.

3.4.2 Heterogeneity Generation: Grain Sorting Processes

Heterogeneity within cross strata arises due to the sorting processes occurring during the avalanching of grains on the lee side (foreset laminae) of migrating dunes or ripples. Two predominant sorting processes have been found (Makse et al., 1998; Kleinhans,2004) to occur during the rolling or flow of grains : a) segregation, wherein the coarser grains are deposited downstream (bottom) of the finer grains (reverse tangential sorting) and b) stratification, which results in high frequency, alternating fine and coarse grained laminae (reverse perpendicular sorting, with finer grains beneath the larger grains). Sorting during avalanching of grains along a slope has been studied extensively from the perspective of geology (Reesink and Bridge, 2009) as well as granular matter physics (Makse et al., 1998). Variations in the size and angle of repose of the grains, and the flow rate (momentum) are commonly (Makse et al., 1997b) identified as the factors that influence the onset of such sorting processes. Phase diagrams that characterize the patterns formed as a function of grain properties and flow variables have been developed previously (Koeppe et al., 1998; Robinson and Friedman, 2002). A detailed analysis of the various sorting mechanisms and the particle flow physics is beyond the scope of this chapter. We describe here some of our observations over the course of the experiments and qualitatively draw parallels to the findings reported previously.

Reverse graded micro-layering was observed in our experiments when grain mixtures were deposited during lateral motion (Step C), onto a surface to form a layer. This resulted in the formation of two sublayers: a fine-grained

bottom layer and a coarse-grained one at the top. This reverse perpendicular sorting was previously reported by Griffith et al. (2013). They attributed this behavior to vibration induced segregation (Rosato et al., 2002). Vibrations caused by the motion of the feed tube, the impact of collision of the falling grains and saltation result in the percolation of the fines and rising up of the coarse particles where the smaller grains filling the voids generated beneath the larger grains. The thickness of the layer is dictated by the velocity of lateral motion and the pause duration. The sublayer thickness is a function of the volumetric ratio of fine to large grains in the mixture.

Reverse perpendicular sorting (stratification) during the avalanching of grains after deposition onto the apex of the slope (Step B) (Makse et al., 1998) was also observed in some of the cross strata generated. Stratification has been attributed to kinetic sieving (Joplin, 1964) and percolation like processes (Makse et al., 1997a) where fines fall through the interstices formed by the larger grains. Grain size ratio and differences in angle of repose have been reported to be the main factors that determine the occurrence of stratification. While we did not investigate the effect of grain shape and angle of repose of the glass beads, we found that amongst the bead size pairings used during the course of the experiments, stratification became prominent when the ratio of the means (d50) of two bead types was 2 and above. Figure 3.9a shows the formation of stratification during crossbed generation. Stratified beds formed using different grain size mixtures are shown in Figures 3.8b & c. The height of the deposited beds also affected the formation of stratified layers. In the

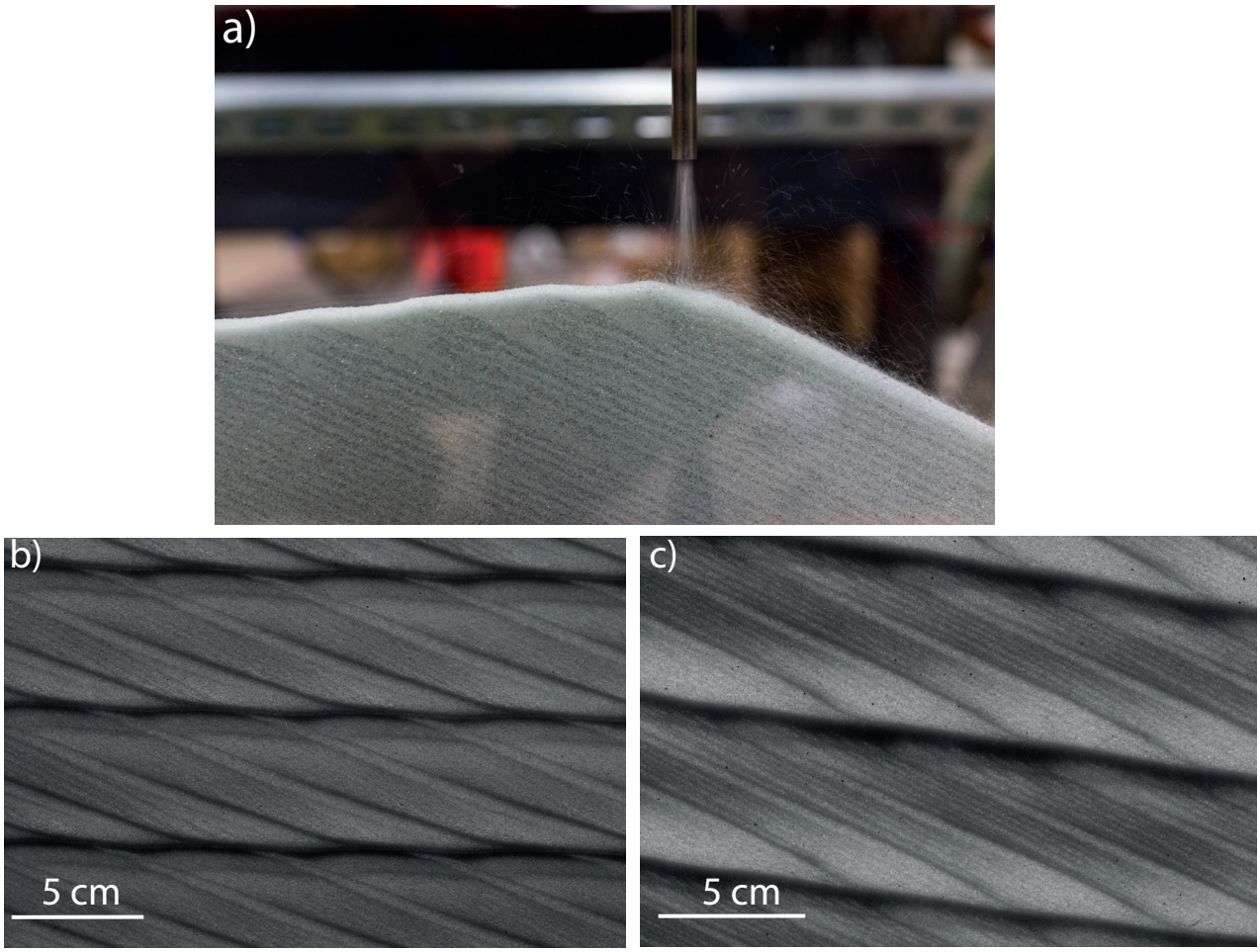

Figure 3.8: a) Stratification during grain avalanche along the lee sides of the cross-beds. b) & c) Stratification observed in cross-beds with coarse to fine grain size ratio of 2.6 and 3.3 respectively.

case of short beds, the height was not sufficient enough for an avalanche to develop completely, resulting in well mixed deposits in between the bounding fine foreset laminae. Other factors such as width of the chamber and grain flow rate have been reported (Koeppe et al., 1998) to affect formation of stratified layers. Employing feed tubes with two different I.D. and chamber widths of 1 cm and 21.8 cm, we found that they had no effect when the bed height was sufficient and grain size ratio was maintained above 2. We speculate that the effect of these factors can become apparent when the sizes of the coarse and fine fractions are closer to each other.

Segregation of grains with large beads at the bottom and fine beads at the top was observed along with stratification in our results. Large grains on account of their momentum are able to roll down further, over on top of fine grains. Retention of fines at the top led to the formation of the fine topset laminae. The bright regions at the toe of the foreset laminae in the light transmitted images (Figure 3.6a,b; 3.8b,c) indicate the aggregation of coarser beads towards the bottom.

3.4.3 Reproducibility

In order to evaluate the reproducibility of the packings generated using the developed technique, multiple realizations of different fabrics were generated and compared. Here we present results from five realizations of cross-beds, generated consecutively using the same input grain mixture and actuator program. A grain mixture made up of 20/30 (P230) and 50/70 (P120) glass beads

in the volumetric ratio of 80:20 was used for this exercise. Images were then captured using light transmission, of the different packs. Gray scale values from the center of each packing (900 x 2200 pixels, 24cm x 58cm) were then evaluated.

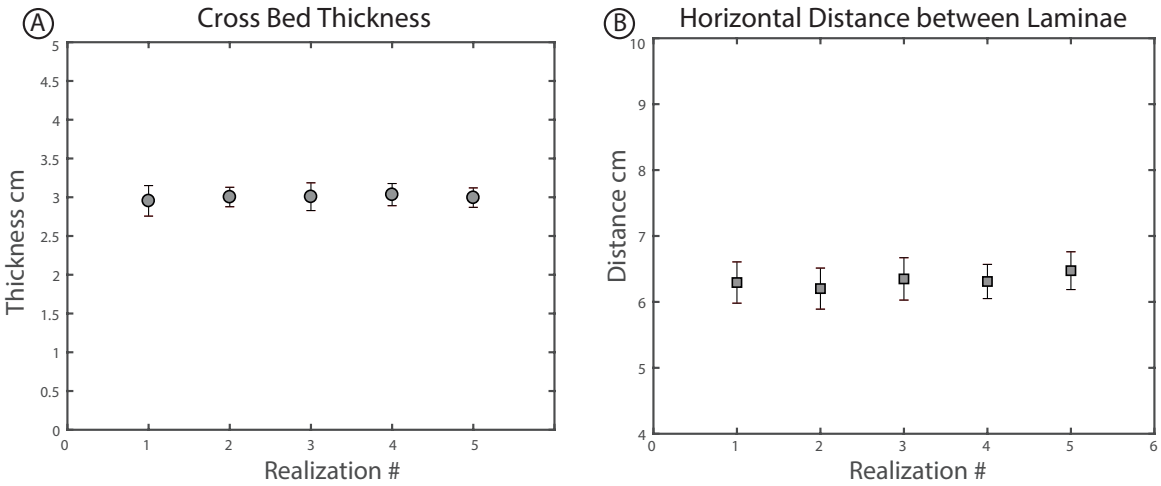

Figure 3.9: Results from measurement of extracted features in ImageJ.

Similarity between the realizations was quantified in two different ways; a) manually measuring the distances between the characteristic features (laminae) and b) using an image processing algorithm. A contrast enhancement filter (Frangi et al., 1998) was first used to extract the features from the images. ImageJ was then used to measure the height of the beds and the horizontal distance between the fine foreset laminae. Fifty measurements were made for each of the two metrics at the same relative position of all five images. Figure 3.9 shows the measurement results. The variation in measures within each realization was found to be less than 1 cm, and in between realizations the

mean values showed little variation.

The filtered images were then compared using the complex wavelet structural similarity index (Sampat et al., 2009). Commonly used extent of spatial overlap measures or mean square error type metrics were avoided since they penalize for differences at the pixel scale. The feed mixture was made from two different sieve fractions. While the beads were mixed well to obtain a homogenized feed, small aberrations in the uniformity of mixing, especially after being introduced into the silo (Rosato et al., 1987), could not be avoided. This resulted in minor spatial variations between realizations. Structural similarity index compares the correlated patterns of intensities locally to determine similarity. The complex wavelet variant allows for minor rotations and translations of the features and thus was well suited to analyze our results. The index ranges from 0 to 1 where 1 indicates the images are identical. Figure 3.10 shows the plot of the similarity index for different image pairs. The similarity index averaged at 0.89 with a standard deviation of 0.01 which indicated very good reproducibility.

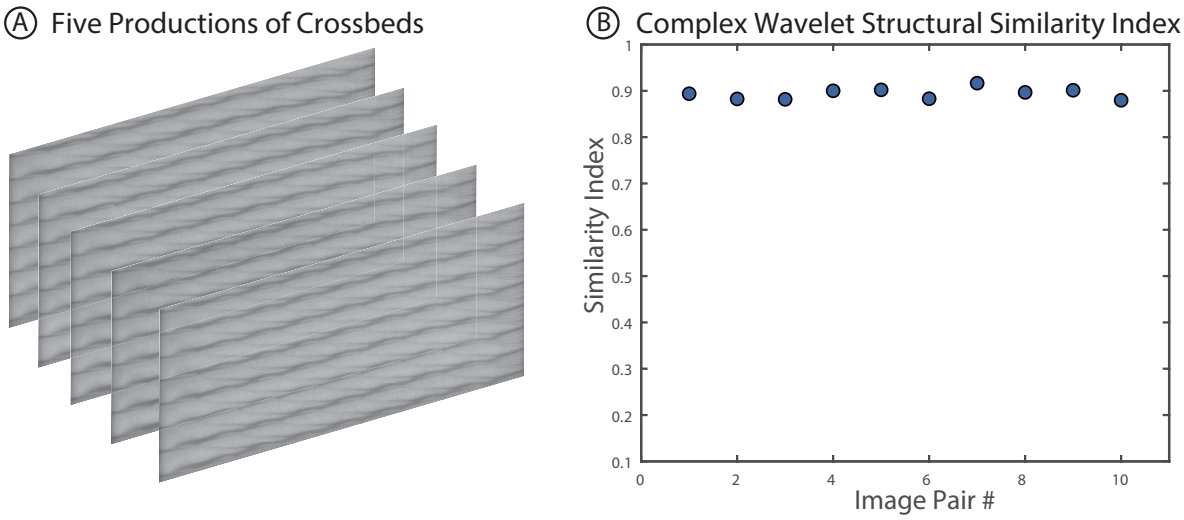

Figure 3.10: Stacked image of the five productions of the cross beds B) Results from the complex wavelet structural similarity index analysis for comparing the different realizations.

3.5 Conclusions and Implications

We have developed a novel automated technique to generate 2D meter scale bead/sand packs with geologically realistic features in a reproducible manner. By combining the avalanching action of grains along a slope, with controlled horizontal and vertical motion, commonly observed sedimentary features like cross strata and ripples laminae could be mimicked in 2D beadpacks. By tuning simple process parameters a range of different geometries were deposited in a facile manner. Reproducibility was evaluated by comparing the prominent features between 5 productions of cross-beds, the results of which showed minimal variability.

The ability to visualize and quantify multiphase flow dynamics in the bedform REV scale has not been ubiquitous. The automated technique presented here enables the study of flow through bedform mimicking meter scale bead/sand packs under controlled laboratory conditions. The ability to generate such packs very efficiently ($<$2 hours) and reproducibly offers a unique opportunity to independently vary the two main factors that contribute to geological heterogeneity: grain size and geometry. This enables a systematic exploration of a wider parameter space while studying different subsurface transport problems.

Chapter 4

Influence of Small Scale Geologic Heterogeneities: Experiments

In Chapters 1 and 2, we discussed the impact of sub-meter scale sedimentological features on the long term migration and immobilization of the injected CO_2. Capillary heterogeneity trapping has been estimated to contribute up to 60 percent of the total residual trapping capacity (Gershenzon et al. 2016). While simulations have been useful in understanding the effect of heterogeneities at different scales, analogous experiments to corroborate these results have been lacking. In Chapter 3 we discussed how previous experimental studies have had to compromise on either the scale (core flooding, micro CT) or the nature of heterogeneity (sand packs) explored. An investigation at the bedform scale (cm to dm) with realistic heterogeneity has not been possible before.

In this chapter, we conduct gravity unstable, immiscible displacement experiments at the intermediate scale in heterogeneous beadpacks with cross-stratified geometry, generated using the automated technique developed in the previous chapter. Keeping the underlying geometry of the packing constant, we vary the grain size distribution to obtain different heterogeneity contrasts.

The experiments are aimed at reproducing CO_2 plume migration dynamics and trapping behavior that would potentially occur downstream of injection wells in actual CO_2 storage sites. The experiments are conducted at atmospheric conditions using an immiscible fluid pair that mirrors the physical properties of supercritical CO_2 and brine at reservoir conditions. Light transmission enables visualization of flow behavior and measurement of saturations in real time. We find that at low grain size contrasts the structural heterogeneity effects are negligible. Beyond a threshold contrast, the non-wetting phase saturations and breakthrough times start to quickly increase in response to the heterogeneity of the packing. The saturations when plotted as a function of the grain size heterogeneity contrast are able to be described by a 4 parameter regression model. Comparing these results with those obtained using simulations in Chapter 2 we comment on the applicability of the predictive model at large scales.

4.1 Methods and Materials

4.1.1 Experimental Setup

The immiscible flow experiments were carried out in a quasi-2D, rectangular glass flow cell/slab chamber with internal dimensions of (60cm x 60cm x 2cm). Details of flow cell construction and features, filling apparatus and pattern generation are reported in Chapter 2. In this work, four multiphase flow experiments were conducted in which the spatial configuration of heterogeneity is kept constant but the bead/grain size pairing is varied to explore

different capillary pressure/grain size heterogeneity contrasts. This becomes possible only due to the reproducibility enabled by the filling technique. The heterogeneity geometry considered here is one that is very commonly observed in clastic outcrops: crossbeddings or cross-stratification. The length scales of the characteristic features of the geologic fabrics considered here (mm to dm) are characteristic of fluvial depositional environments (Reineck and Singh, 1980).

4.1.2 Materials

Translucent glass beads acquired from Potter Industries were used to pack the chamber. The bead sizes were characterized using an image based particle analyzer (CAMSIZER, Retsch Technology). Capillary entry pressures of the different glass beads were also measured for the fluid pair used in these experiments [see Appendix 4.4.4 at end of chapter]. The glass bead sizes used in this chapter along with their properties are shown in Table 4.1.

Table 4.1: Glass Properties

Bead Type	US Sieve	Mean Diameter (mm)	Std. Deviation (mm)	Entry Pressure (Pa)
Coarse (P337)	20-30	0.689	0.086	216
Fine 1 (P280)	25-35	0.599	0.07	262
Fine 2 (P230)	30-40	0.457	0.06	293
Fine 3 (P170)	30-40	0.331	0.03	477
Fine 4 (P140)	25-35	0.259	0.03	586

For the gravity unstable multiphase flow experiment, heptane was chosen to be the non-wetting phase and a glycerol-water mixture (50:50 w/w) as

the wetting phase. The intention here was to mimic the buoyancy and capillary dominated migration of CO_2 in the subsurface. Since the experiments were conducted at atmospheric temperature and pressure conditions, we chose surrogate fluids that mimic the physical properties of supercritical CO_2 and brine under reservoir conditions (Nordbotten et al., 2005). The heptane was dyed with Oil-Red O (40mg/L) (Alfa Aesar) in order to introduce a contrast in the transmitted light intensities while imaging. The fluid properties are given in Table 4.2. The viscosity of the fluids was measured using a spinning disc viscometer. The interfacial tension between the two phases was measured using Rame-Hart sessile drop tensiometer.

Table 4.2: Fluid Properties

Fluid	Density (kg/m3)	Viscosity (cP) 22° C
Glycerol+Water (50:50 W/W)	1115.4	6.25
Heptane	684	0.41
Interfacial Tension	36 mN/m	

4.1.3 Design of Heterogeneity

The heterogeneity geometry, designed to mimic crossbeddings is kept constant throughout the four experiments performed in this chapter. The bead size pairs used to generate the patterns however are varied across experiments. This variability in the textural contrast of the fabrics is designed on the same lines as our previous 3D modeling work (Chapter 1)(Trevisan et al., 2017a). The crossbeds are considered to constitute of two facies: matrix (coarse grained) and laminae (fine grained). In these experiments, the ma-

trix grain size makeup is kept fixed while the laminae constitution is changed. Thus, using the five bead size fractions available, 4 different matrix-laminae pairings are obtained. This is summarized in Table 4.3. In all cases, the coarse to fine volumetric ratio is kept constant at 80:20 which is again drawn from our previous work. Going from experiment 1 to 4, the distance between the size distributions of the grain size pairs and hence the heterogeneity contrast increases. To quantify this grain size heterogeneity, we introduce a dimensionless parameter δ :

$$\delta = \frac{\mu_1 - \mu_2}{|\sigma_1 + \sigma_2| / 2} \tag{4.1}$$

Where, μ_1 and μ_2, and σ_1 and σ_2 are the means and standard deviations of the bead sizes of the matrix and lamina respectively. This metric is slightly different compared to what was introduced in Chapter 1. There the matrix and laminae grain sizes had different means, but the sorting or standard deviation remained the same. In this case, since both grain size distributions have different spreads, accounting for them becomes essential.

4.1.4 Flow Invasion Experiment

A schematic drawing of the experimental setup illustrating the packing arrangement and boundary conditions is shown in Figure 4.1. The flow cell was packed using the automated filling system (Krishnamurthy et al., 2017a, 2017b, 2019) with grain size pairs shown in Table 4.3. In all cases, the cross-stratified media made up about two thirds (approximately 42 cm) of the height

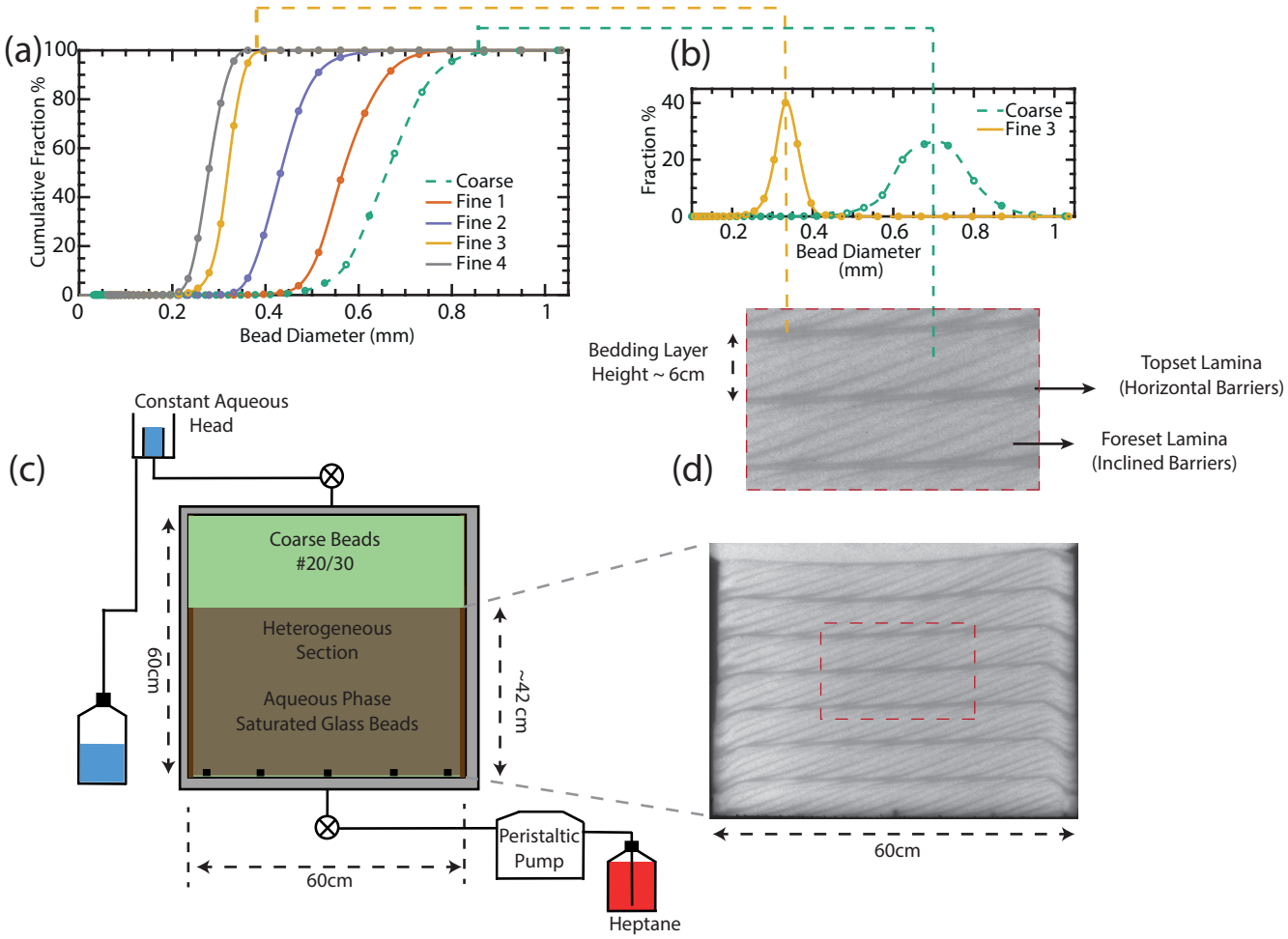

Figure 4.1: (a) Ensemble cumulative size distributions of the glass beads used in this study. (b) The packing is made up of a mixture of two bead sizes. Across experiments, the coarse size fraction is kept constant, while different fine bead fractions are used. Image shows one such pair. (c) Schematic of the experimental setup.(d) Beadpack with cross-stratified geometry generated using the bead mixture shown in b.

of the flow cell while the remaining portion at the top was packed with the coarse beads (20/30). This was done so as to avoid capillary end effects and visualize the flow at the boundary of the heterogeneous section. During the packing process, a layer of very fine beads (100 micron mean diameter) was deposited on the edges of the cell manually in order to prevent preferential flow of the non-wetting phase along the lateral boundaries. The dry pack was then purged slowly with CO_2 gas (5 LPM) for 72 hours, by injecting via all five inlet ports at the bottom so as to displace all the air with CO_2. Each inlet port consisted of a steel tube (internal diameter: 5 mm) with a metal mesh screen attached at the top to prevent the glass beads from falling out. Following this, the packing was saturated with the aqueous phase (glycerol-water) by gravity stable flooding. The CO_2 purging step ensured that packets of air don't remain trapped in the beadpack during the aqueous phase flooding. After sealing the chamber with the top plate, it was flushed with one pore volume of the aqueous phase in order to displace the CO_2 saturated aqueous phase with a fresh one. At the top, the outlet tube from the central port was connected to the constant aqueous head. During the invasion, Oil Red-O dyed heptane was injected through the central inlet port using a peristaltic pump (Masterflex series, Cole Parmer). Pressure transducers (Omega PX409-005G) were connected to the inlet and outlet flow lines to log real time pressure data (0.03 Hertz)

The experiments were designed to have 4 stages. The first stage consisted of injection until the leading edge of the non-wetting phase had reached

Table 4.3: Design of Experiments

Exp. No.	Matrix μ (mm)	Lamina μ (mm)	Porosity	δ	Ca	Bo
A	Coarse (0.689)	Fine 1 (0.599)	35.2	1.154	1.11E-5	4.21E-2
B	Coarse (0.689)	Fine 2 (0.457)	34.4	3.165	8.82E-6	2.45E-2
C	Coarse (0.689)	Fine 3 (0.331)	34.6	6.037	6.4E-6	1.29E-2
D	Coarse (0.689)	Fine 4 (0.259)	33.7	6.677	7.5E-6	9.95E-3

the far edge of the heterogeneous section breakthrough of the NWP through the heterogeneous section of the packing. During the second stage, injection of the NWP continued for 12 hours post breakthrough after which injection was stopped. During the third stage the inlet valves were shut in and the fluid redistribution was monitored for 72 hours. The final stage consisted of aqueous phase injection for 24 hours. The first two stages combined form the drainage phase which is analogous to the post injection migration of CO_2. The redistribution stage was meant to act as a proxy for the imbibition that occurs at the tail of the migrating CO_2 plume. The fourth stage mimics forced imbibition and was meant to test the integrity of trapping. The NWP injection was carried out at small flow rates (0.2ml/min) in order to reduce the influence of viscous forces. The aqueous phase was injected at a higher rate (0.5 ml/min) during forced imbibition.

4.1.5 Image Acquisition

To visualize the NWP migration, the flow cell was backlit by a LED panel. The 25" x 25" panel (Evo-Lite Industries) was made up of LED strips (5700K) on all four edges with a diffuser on the face. The panel was mounted

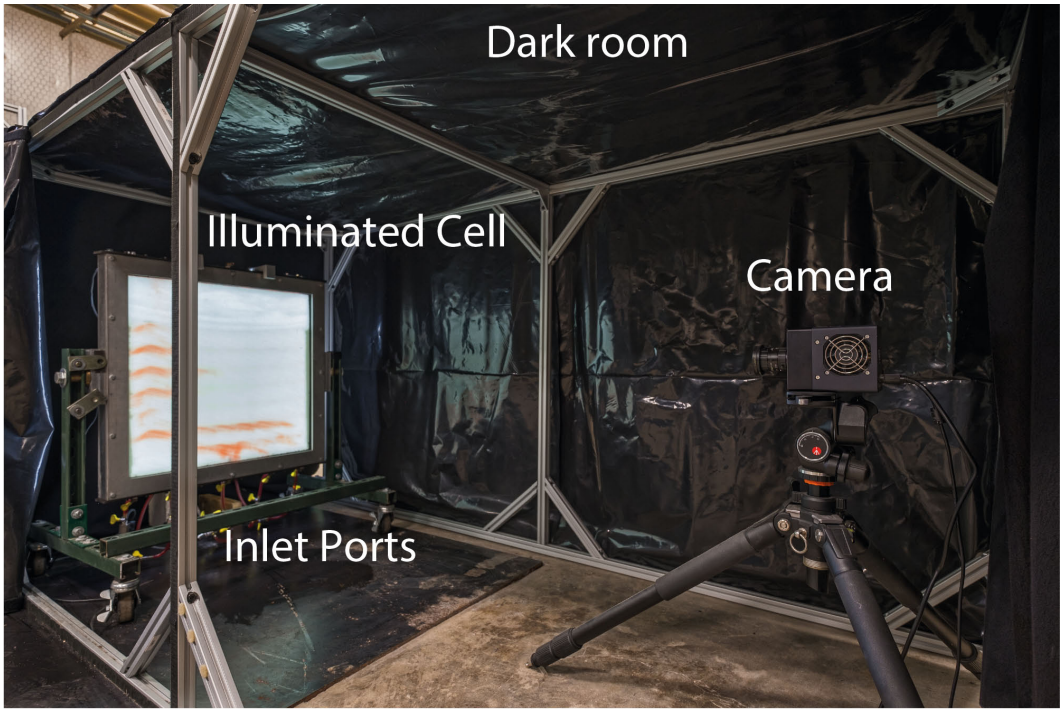

Figure 4.2: The experiments are conducted in a dark room setup to aid visualization. The LED light panel is mounted on the back of the packed chamber and the camera is placed in front. Dyed heptane is introduced from the ports at the bottom.

onto the cell against the back window. Once mounted, the flow cell was moved to the dark chamber with the imaging system in place (Figure 4.2).

For imaging the flow and quantifying the attenuation of the transmitted light by the non-wetting phase, a thermoelectrically cooled charge-coupled device (CCD) camera (Finger Lakes Instrumentation, NY, Model MLX814) is used. The camera consists of a 9 megapixel (3388 x 2712 pixels) monochrome Sony ICX814 sensor (12.48 mm $\times$9.9 8mm) with 3.69 $\times$ 3.69 micron sized pixels. The thermoelectric cooling of the CCD (maintained at 0^o Celsius during acquisition) helps reduce the noise and increase the dynamic range. With an electron well of 15000e- and RMS noise of 2e-, the sensor is able to register 7500 different gray values. The camera is mounted with a low distortion 25 mm fixed focal length lens (Edmund Optics, NJ). Using a computer interface, 16-bit images (65536 greyscale values) were acquired in 30 second intervals throughout the flow experiment. The distance between the camera and flow cell changed between experiments resulting in a spatial resolution of around 0.250 mm/pixel. This number varies slightly, since the relative position distance between the camera and glass cell changes from experiment to experiment.

A bandpass filter with a 520 nm center wavelength and a bandwidth (Full Width at Half Maximum) of 10 nm is attached to the lens during imaging. The filter thus only allows light with wavelengths between 500 to 530 nm to pass through. The filter was chosen such that its center wavelength is close to the absorption peak of Oil-Red O dyed heptane in order to enhance the

contrast between the non-wetting and wetting phases (See Appendix 4.4.3.1 for more on contrast enhancement). The aperture of the lens was kept fixed at f-8 to achieve a larger depth of field. The exposure time of each frame was kept constant at 0.3 seconds.

4.1.6 Image Analysis and Saturation Quantification

The Light Transmission Visualization (LTV) technique (Bob et al., 2008; Tidwell and Glass, 1994; Darnault et al., 1997; Nimet and Selker, 2001) enabled recording of the non-wetting phase migration patterns at high resolution and in real time along with saturation quantification. The details are provided in the appendix 4.4.3 at the end of the chapter.

4.2 Results and Discussion

4.2.1 Heterogeneity Effects on Invasion Patterns

Figure 4.3 shows the invasion patterns at the end of breakthrough and drainage; from left to right, the grain size of the laminae decreases as shown in the top inset. The invasion sequence is color coded with cooler colors representing earlier times. The breakthrough times are also shown in the figures. With fining of the lamina (increasing heterogeneity contrast), the footprint of the invading non-wetting phase dramatically increases.

At the lowest heterogeneity contrast, the invading phase traverses the system quickly. The flow is dominated by the propagation of a single finger until breakthrough. During the post breakthrough injection phase, fragmen-

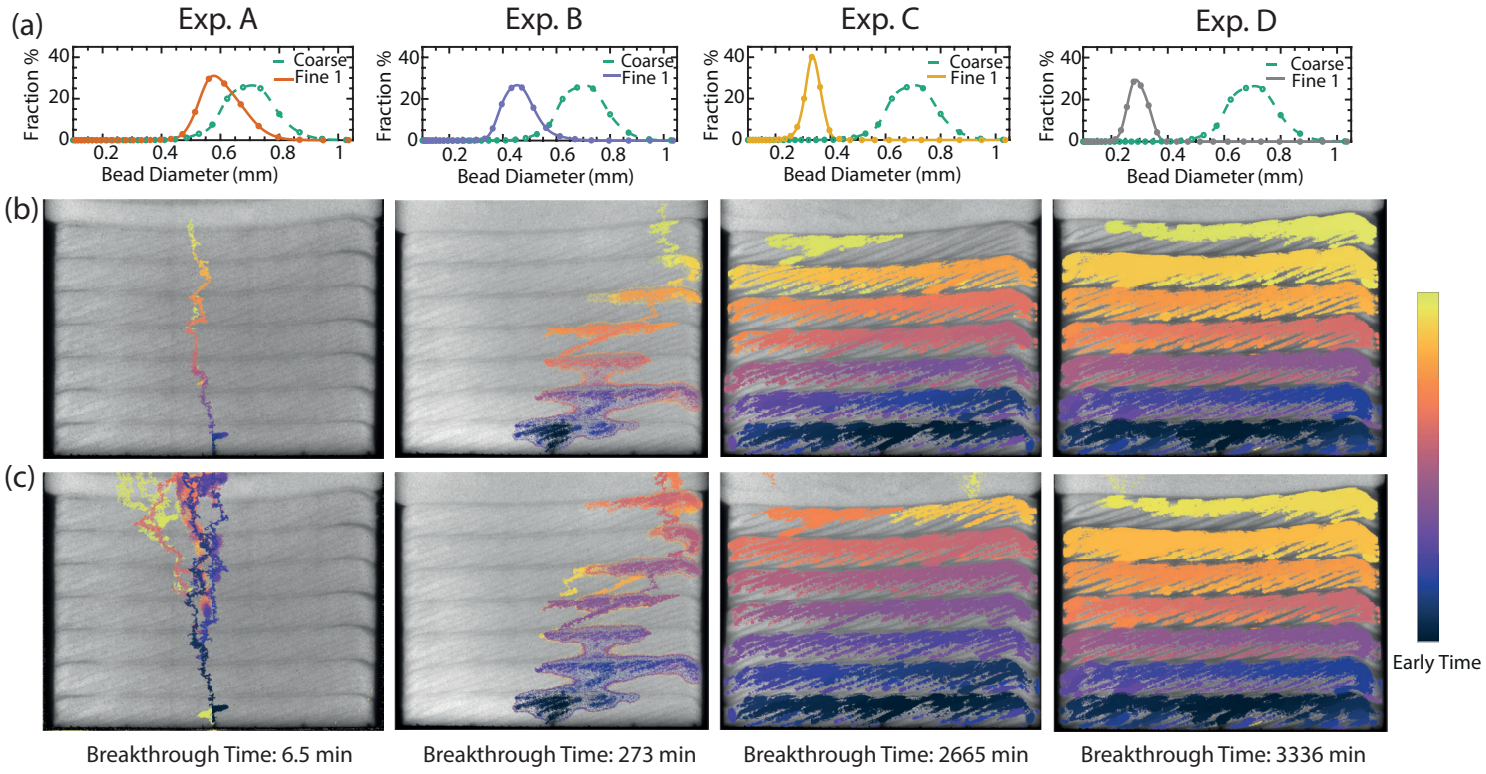

Figure 4.3: (a) Size distributions of the bead pairs used in the 4 experiments. Moving from left to right, the grain size contrast increases. Time sequence maps of invasion showing the evolution of non-wetting phase flow at the end of (b) breakthrough and (c) drainage. The cooler colors represent early time.

tation events are observed, often followed by new branches or fingers forming. At the next level of grain size contrast, the heterogeneity fabric/geometry of the medium alters the invasion pattern. Here the invading phase is held up beneath the laminae – both the horizontal and cross-beds – causing lateral spreading before eventually breaking through each layer. With increasing grain size contrast, the invading fluid accesses increasing portions of the pore space, and the pattern exhibits greater pooling and back filling beneath set of laminae. The intermittency in flow and formation of alternative pathways is reduced with increasing heterogeneity contrast; the invasion pattern undergoes slight variation post breakthrough in experiments B and C, and stays almost constant in experiment D.

There are two main geologic features that influence the migration pathways: the laterally spanning horizontal barriers bounding each bedding layer and the cross-strata within each layer. The fine-grained laminae act as capillary barriers causing the non-wetting phase to get trapped beneath them. The extent of influence of these features however is determined by the grain size contrast. The amount of overlap between the grain size distribution of the facies can be seen as a reasonable proxy for trapping behavior. As the overlap increases (going from case D to A) more pathways become accessible for the invading phase to circumvent the high capillary entry pressure regions.

In experiment A, owing to the overlap between the two grain size distributions, the invading phase experiences almost no opposition in terms of capillary entry pressure barriers and is able to span the system quickly. With

the effect of capillary heterogeneity subdued, the destabilizing gravity gradient dominates, resulting in the propagation of a single finger or branch initially. As the fingers grow vertically, in the direction of the gradient, withdrawal and local imbibition events are observed leading to fragmentation and loss of connectivity. When the non-wetting phase cluster height builds such that the buoyancy gradient surpasses the local capillary thresholds, fragmentation occurs with the cluster migrating upwards and the wetting phase re-invading those pores. Sometimes, the non-wetting phase is replenished and connectivity is restored quickly by the constant inflow of heptane while in some instances, these fragmentation events lead to the formation of new pathways (Stohr and Khalili, 2006; Wagner et al., 1997; Birovljev et al., 1995).

With increasing grain size contrast, the structural heterogeneity effects become more prominent. Once the invading phase enters the system, vertical migration ensues but is influenced by the cross-strata, with the heptane moving along the coarse-grained regions between the fine foreset laminae. The NWP migration occurs in the form of fingers or stringers until a capillary barrier is encountered. This could be the prominent horizontal laminae or small-scale heterogeneities that exist along the cross-strata. In the case of the latter, some back filling occurs but more often than not, the NWP finds an alternative pathway which could lead to lateral or even downward migration along adjacent coarse-grained zones. When it reaches the fine-grained horizontal laminae, the NWP starts pooling and back-filling downward. During this phase, the NWP also invades adjacent regions with capillary entry pressures

lower than that of the laminae if the appropriate pressure is exceeded, leading to lateral migration. The back filling and lateral migration continue until the horizontal barrier is breached. The breach occurs at a location accessible to the NWP that is most favorable in terms of capillary entry pressure. Typically, the barrier is breached at only place, however in experiments C and D, additional breaches were observed albeit not simultaneously. Once the NWP enters the next layer similar dynamics are observed.

Overall the vertical invasion across layers does not occur in a linear, piston like fashion. The invasion sequence maps show that, while invading a particular layer or especially when backfilling beneath a capillary barrier, the non-wetting phase at times also concurrently invades regions at lower elevations that probably have smaller entry pressures. This behavior of growth behind the invasion front is characteristic of low capillary number flows (Zacharoudiou et al., 2018; Zhang et al., 2011; Tsuji et al., 2016; Wang et al., 2012).

4.2.2 Back-Filling and Pool Heights

As discussed in the previous section, the non-wetting phase back-filling height beneath the horizontal laminae increases from experiment A through D, as the heterogeneity contrast increases. The non-wetting phase breaks through the horizontal capillary barriers when the back-filled depth is sufficient to overcome the capillary entry pressure of the fine-grained laminae. To explore this dependence of back-filling on capillary entry pressure, we plot the experimentally observed pool heights as a function of the mean radius of the fine fraction

beads (Figure 4.4).

Comparing the observed values with those obtained from capillary entry pressure tests, we find that the two curves follow the same upward trend as expected. However, we find varying levels of discrepancy between the two curves. The error bars also indicate that there is quite some variability in the observed heights.

The main reason for this discrepancy and error bars is the heterogeneity of the system. Owing to the fact that segregation occurs naturally during packing, the matrix and laminae most likely will not constitute of the pure coarse and fine fractions respectively. This mixing of the beads can lead to lower entry pressure contrast than that when the properties were measured, leading to smaller back-filling heights. This intra-facies heterogeneity also means that the breach can occur relatively quickly in some areas compared to others. The variability can also be attributed to non-uniform laminae thickness. The geometry of the packing also has a direct effect here, especially in experiment D, where the maximum possible back-filling height is limited by the bedding layer height. This has repercussions which we discuss further down the line.

4.2.3 Flow regimes

Considering the large scale behavior of these experiments, going from A through D, we find that the non-wetting phase invasion starts to look like frontal displacement with increasing heterogeneity. Gravity fingering and dynamical effects like intermittency and fragmentation are prevalent in experi-

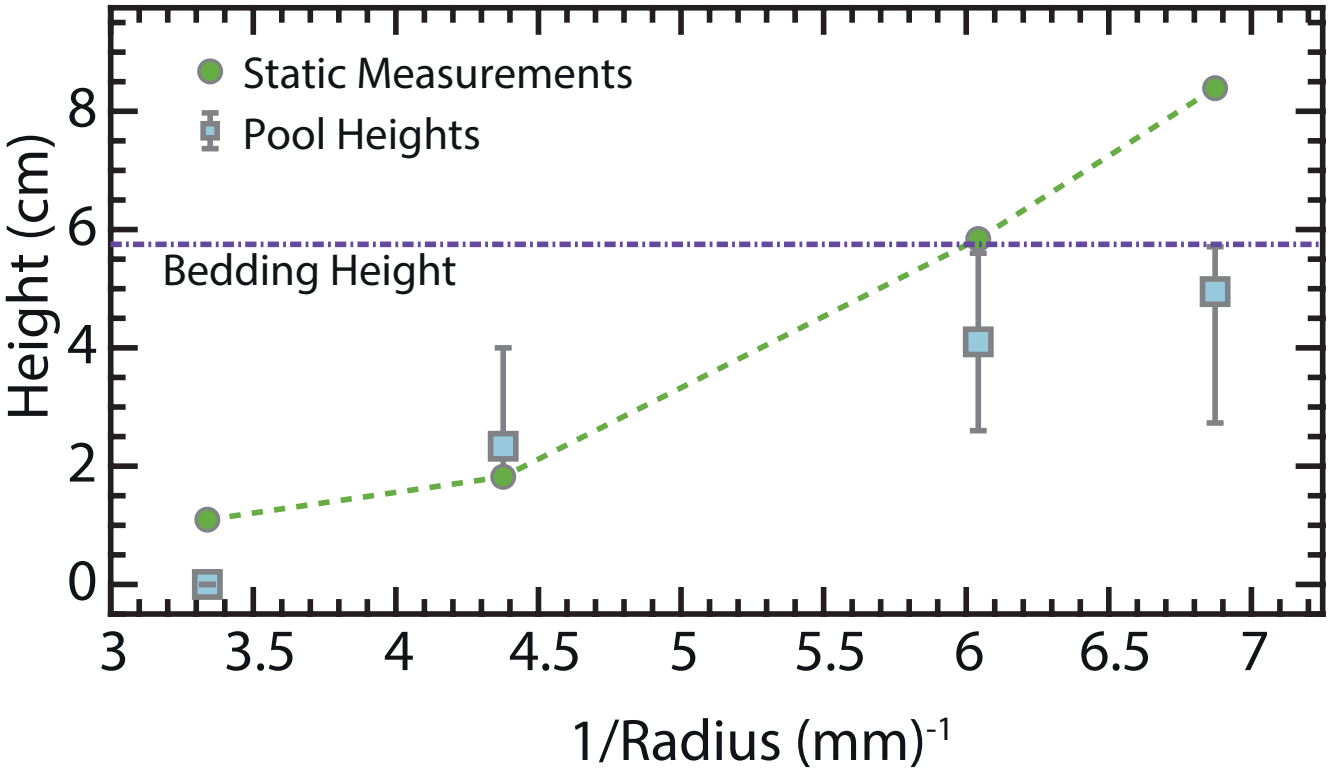

Figure 4.4: Non-wetting phase back-filled pool heights observed in flow experiments and displacement pressure head from static capillary entry pressure measurements plotted as a function of inverse of the mean radii of the fine glass bead fraction used in each experiment.

ments A and B, whereas C and D display invasion percolation type behavior. In other words, we find that the influence of capillary forces increases and relative influence of gravity reduces going from experiment A through D. To put this in context of traditional metrics of immiscible displacement we use dimensionless ratios (Ewing and Berkowitz, 1998) that have been commonly used for characterizing flow behavior: Capillary number (Ca) and Bond number (Bo)

$$\text{Ca} = \frac{\text{Viscous Force}}{\text{Capillary Force}} = \frac{\mu_i v_i}{\sigma} \tag{4.2}$$

$$\text{Bo} \ = \frac{\text{Gravity Force}}{\text{Capillary Force}} = \frac{\Delta\rho \cdot g \cdot d^2}{\sigma} \tag{4.3}$$

Where μ_i and v_i are the viscosity and velocity of the invading phase, σ is the interfacial tension, d is characteristic length scale, and $\Delta\rho$ is the density difference.

In a system like ours with multi-scale heterogeneity, these numbers will vary temporally and spatially. We acknowledge this limitation while reporting these numbers. Averaged, front finger velocities determined using image analysis for each experiment, are used to calculate the capillary numbers. We expect this to be the upper bound since during back-filling, the velocities can be lower. The capillary number is found to decrease from A through C and increases slightly in experiment D (Table 4.3)

The characteristic length scale in the Bo calculations is assumed to be the grain diameter following Herring et al. (2015). We use the fine fraction

mean grain sizes for our calculations since that is the differentiating parameter between experiments. We find that the Bo decreases going from experiment A through D. Thus, these trends agree with the observations from the experiments. The increase in non-wetting phase trapped saturations with decreasing influence of gravity seen here, follows previous observations by Bandara et al. (2011) at the pore scale and Ide et al. (2007) at the reservoir scale.

Evidence for these experiments being capillary controlled can also be inferred from the pressure response. We plot the difference between the inlet and out pressures as a function of time for these experiments (See Appendix Figure 4.14). The pressure signal displays repeated fluctuations indicative of capillary pressure variations as the non-wetting phase invades the pore space. These fluctuations have been reported previously during slow drainage (Maloy et al., 1992; Furuberg et al., 1996; Moeibus and Or, 2014; Primkulov et al., 2019), low capillary number core flooding (Reynolds et al., 2017), slow gas expansion(Mumford et al., 2008), vertical gas injection (Geistlinger et al., 2006) and drying in porous media(Biswas et al., 2018). For a relatively homogeneous medium (Case A) low capillary pressure flows result in fluctuations about the same mean (Biswas et al., 2018) (Figure 4.14 and 4.15, Appendix). In cases B through D, owing to the correlated pore geometry, we observe an intermittent pressure response(Borgman et al., 2017).

4.2.4 Redistribution Dynamics

When the non-wetting phase injection is stopped, the gravity driven counter current flow of the wetting phase ensues. The wetting phase subsequently reinvades some of the non-wetting phase containing pores thereby mobilizing them. In all four experiments, we observe displacement of the non-wetting phase during fluid redistribution. Non-wetting phase saturation maps at the end of drainage and redistribution are shown in Figure 4.5a & b respectively. The difference between the two saturations is shown in Figure 4.6b, which shows the non-wetting phase displaced more clearly.

The figures show that in all experiments, the extent of the non-wetting phase displacement is not the same in the different layers with certain layers retaining almost all of the invading phase intact. This could be due to a variety of reasons like local heterogeneities, layer specific non-wetting phase connectivity and the nature of the imbibing phase flow pathways. However, a commonality across experiments is that, as the elevation increases, the non-wetting phase displacement diminishes. To understand this, we plot fluid displacement sequence maps (Figure 4.6a). Here, cooler colors indicate early time imbibition. Looking at the sequence maps and the time-lapse videos we find that non-wetting phase from the lower layers tend to be displaced first. The immobilized invading phase, while migrating vertically, at times gets trapped in the overlying layers leading to replenishment of the drained regions and occasional invasion of new pore space. Similar to invasion, pulsation due to cyclic invasion and draining of the non-wetting phase occurs during

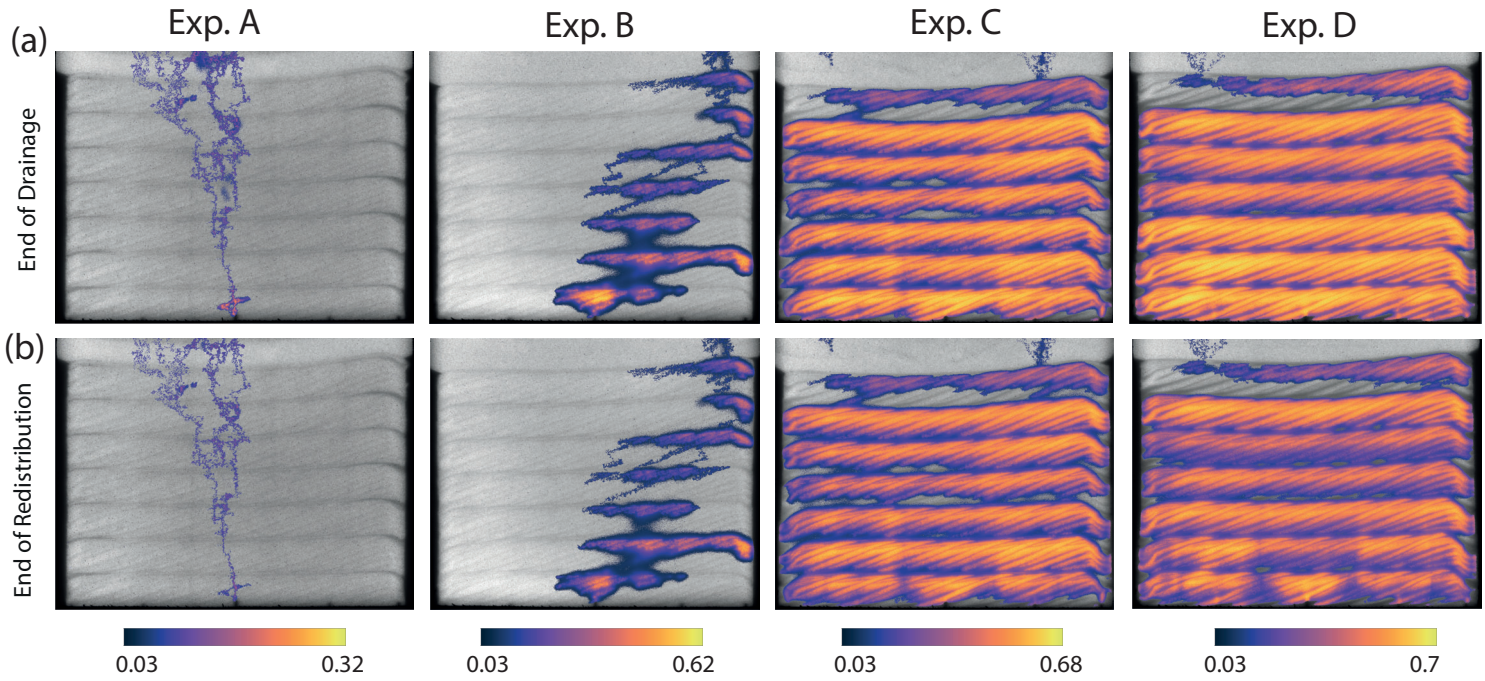

Figure 4.5: Non-wetting phase saturation for the four experiments at (a)End of Drainage and (b) End of Redistribution. From left to right (A to D) the grain size contrast increases and so do the invasion saturations. The drainage saturation has a first order effect on the redistribution saturation.

redistribution as well. Certain layers being bypassed, saturation increase at the upper layers due to trapping, and the cyclicity in saturations become apparent in the plots the showing the non-wetting phase volume variation with time during redistribution (Appendix Figure 4.16)

4.2.5 Heterogeneity and Immobilization

As Figures 4.5 and 4.6 show, the saturations at the end of imbibition for each of the cases vary as per the initial state of the system i.e. the end of drainage saturation. Thus, as the grain size contrast increases, the imbibition saturation increases but at the same time, we also find that more NWP volume gets displaced and leaves the system. To better understand this seemingly disparate behavior, we plot the final to initial saturation ratio (commonly known as trapping efficiency) as a function of heterogeneity (Figure 4.7a). We find that the efficiency initially increases with the heterogeneity contrast as expected, but falls in case of experiment D.

One possible explanation for this observation can be gained by considering the capillary heterogeneity contrast, non-wetting phase connectivity and the height of the bedding layers. Figure 4.4 shows that in the case of experiment D, the height of the back-filled pools is much smaller than that of the static measurements, and that their average height is very close to that of the bedding layers. This can lead to increased vertical connectivity of the non-wetting phase thereby leading to more buoyant migration during the redistribution phase (Herring et al., 2015). Another possibility is that the

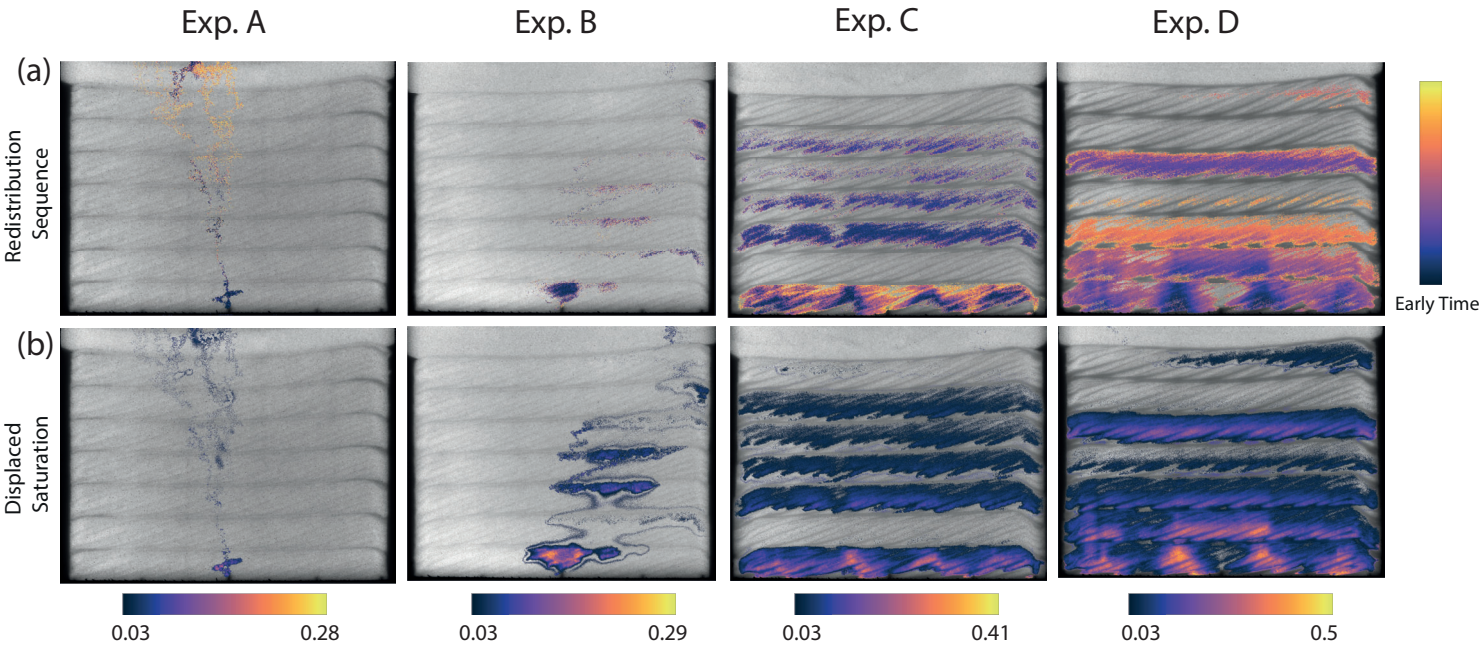

Figure 4.6: (a) Time sequence maps of redistribution. The cooler (darker) colors indicate early time. (b) Difference between drainage and redistribution saturations. The image shows the non-wetting phase that has been displaced and left the system (heterogeneous section).

non-wetting phase, during back-filling behind a high contrast barrier, ends up invading the smaller pores, which get imbibed quickly during redistribution (Pentland et al., 2010). This increase in NWP and fall in the efficiency is reflected in the trapping curve and explains the reason behind plateauing of the saturation values (Figure 4.9).

4.2.6 Trapping Efficiency and Storage Capacity

Non-wetting phase saturations at end of the forced imbibition are given in Table 4.4. Comparison with post-redistribution values show that non-wetting phase volume displaced during the forced imbibition step is minimal leading to a saturation reduction of about 1% or less. Most of this displacement occurs near the inlet.

Separate tests (not shown here) where the injected wetting phase was dyed to help track its movement showed that in experiments with low invaded saturations, the non-wetting phase saturated regions get bypassed during imbibition. In cases like experiments C and D, where the non-wetting phase spans across the width of the system, the wetting phase is able to move through these regions with little effect on the in-situ heptane saturations. The persistence of non-wetting phase trapping can possibly be attributed to relative permeability effects (causing bypassing) and wetting phase movement via film flow. With increasing flow rates (larger imbibition Ca), we observed more desaturation, as reported by previous studies (Herring et al., 2015).

Observing the images in Figure 4.6 closely, we find that the non-wetting

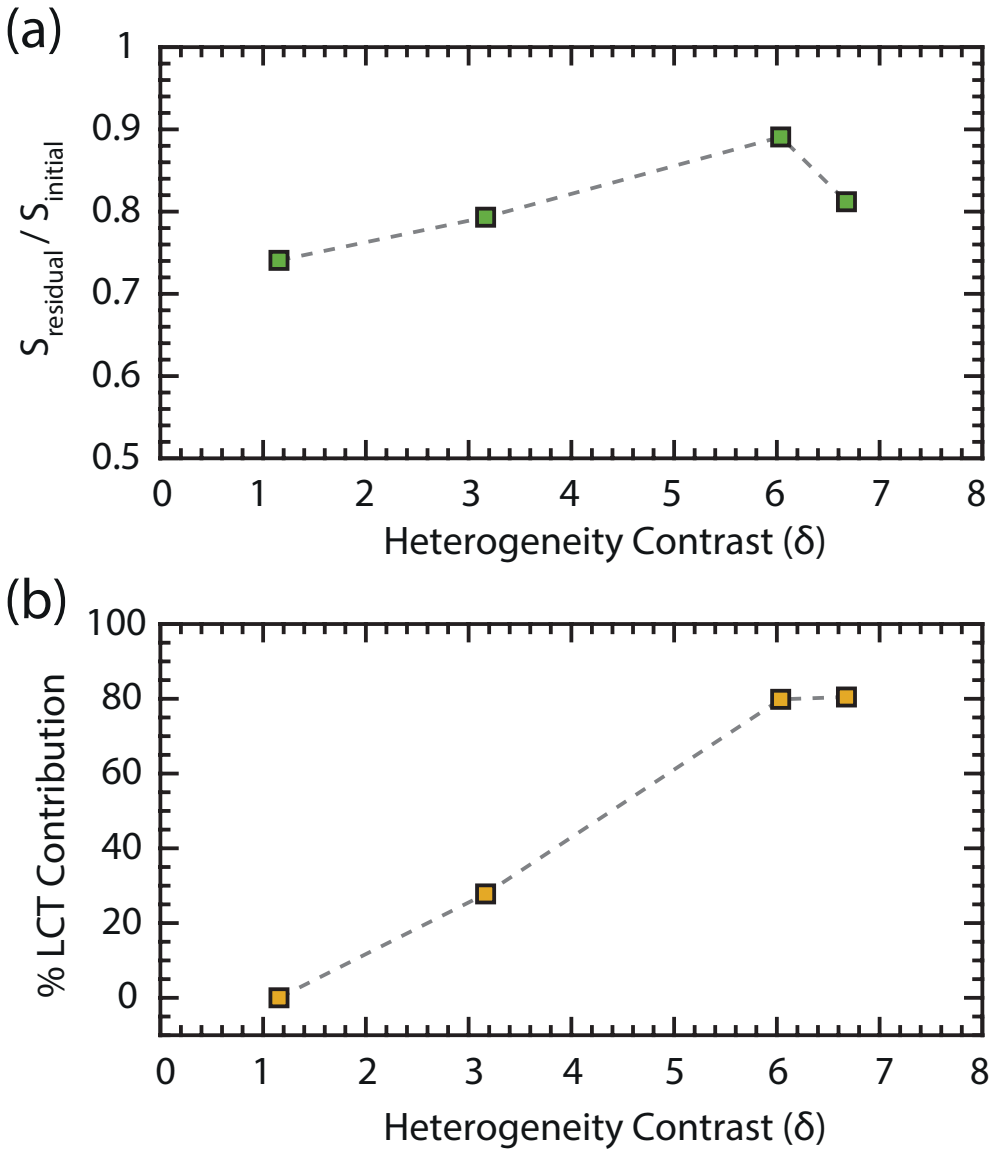

Figure 4.7: (a)Ratio of the average non-wetting phase saturations at the redistribution to that at the end of drainage (efficiency of trapping) plotted against the grain size heterogeneity contrast (b) Contribution of local capillary trapping (capillary heterogeneity trapping) to the overall trapping capacity (rest is residually trapped) as a function of heterogeneity contrast.

Table 4.4: Slab Averaged Saturations at the End of Different Stages

Exp.	Breakthrough Sat.	Drainage Sat.	Redistribution Sat.	Imbibition Sat.	Sr/Si
A	0.00086	0.0027	0.002	0.002	0.74
B	0.029	0.0324	0.0257	0.025	0.79
C	0.308	0.315	0.280	0.277	0.89
D	0.370	0.368	0.298	0.295	0.81

phase is immobilized in two distinct forms: as isolated blobs or ganglia at residual saturations in the finger/stringer pathways and regions where the mobilization has occurred, and majorly in the form of high saturation, back-filled pools. Such higher than residual saturation, non-wetting phase clusters, trapped behind capillary barriers, known as Local Capillary Traps (LCT) (Saadatpoor et al., 2010; Li and Benson, 2015; Trevisan et al., 2017a; Ren et al., 2019) have been shown to be significant contributors to the overall trapping capacity (Gershenzon et al., 2016). Using a conservative saturation cutoff value of 0.25 (maximum non-wetting phase residual saturation) to demarcate residually trapped and local capillary trapped regions, we plot the contribution of these mechanisms for the four experiments as a function of the heterogeneity contrast (Figure 4.7b). As expected, we find that the LCT contribution increases with increasing heterogeneity contrast. In experiment A, due to the lack of capillary barriers, all the non-wetting phase is residually trapped. The LCT contribution increases in experiments B and C, but plateaus after experiment C mirroring the trend shown by trapping efficiency.

We also plot the non-wetting phase saturations (pixel wise) at the end

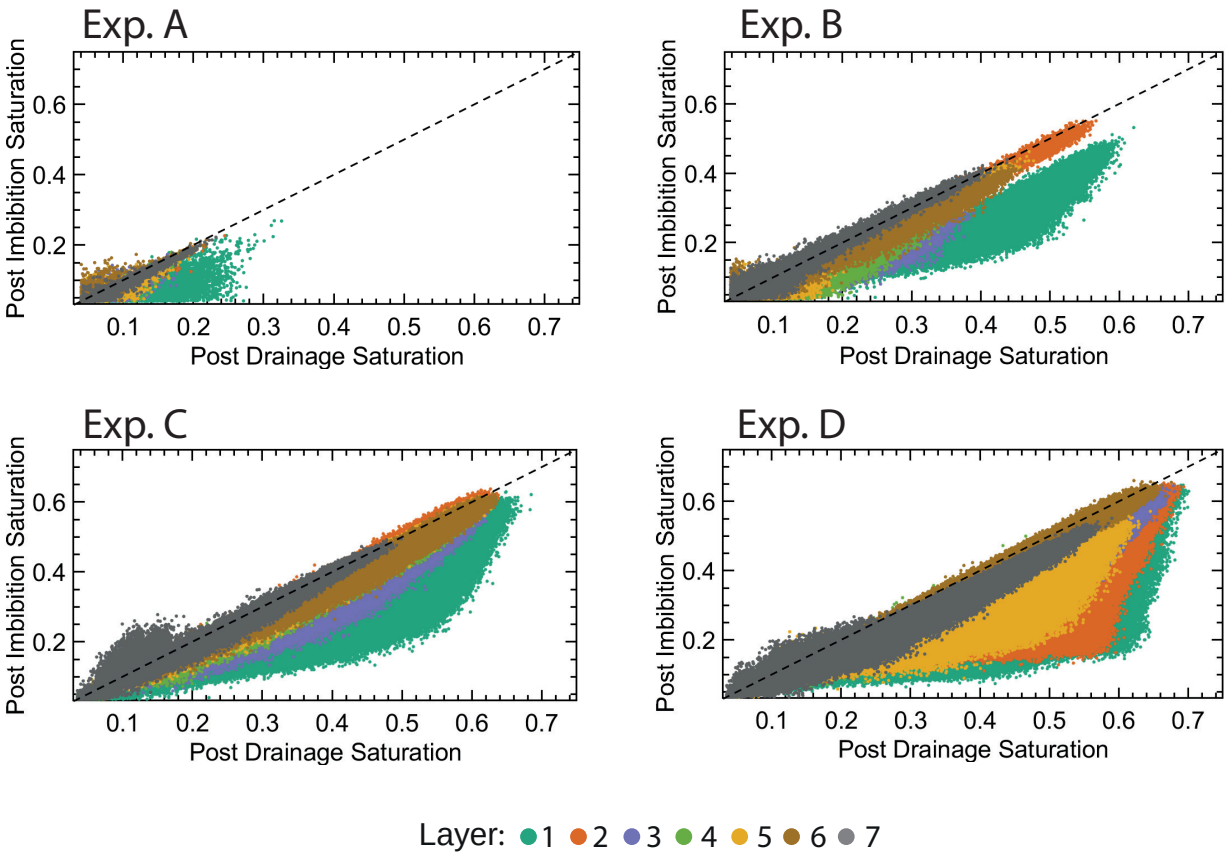

Figure 4.8: (a) Pixel-wise trapped non-wetting phase saturation as a function of maximum initial saturation reached at the end of drainage for the four experiments (Initial-Residual curves). The dashed line shows 100% trapping (Land trapping co-efficient C=0). The colors of the circles indicate the bedding layer starting from the bottom.

of imbibition versus the saturations at the end of drainage (maximum initial saturation) to visualize and evaluate trapping performance (Figure 4.8). These initial-residual plots have been used conventionally to generate parametric trapping models by fitting empirical data(Krevor et al., 2015; Spiteri et al., 2008). In this case, we fit the results to the most widely used Land trapping model:

$$S_r = \frac{S_i}{1 + CS_i} \tag{4.4}$$

Where S_i is the initial saturation (post drainage), S_r is the final saturation (post imbibition) and C is the Land trapping coefficient. We also plot the 1:1 line (C=0) in which all the invaded non-wetting phase remains trapped at the end of imbibition. Thus, lower values of C, indicate better trapping efficiency. The data in the plots (Figure 4.8) show a large amount of scatter. To understand this spread, we segregate and color code the data layer-wise. We also fit the model to data from each layer rather than the entire system (Appendix Table 4.5). We observe a common trend in all the plots: with increasing elevation, the trapping efficiency increases (decreasing C values). This follows our observations from the previous section (Figure 4.6) where we noted that the lower layers experience more non-wetting phase displacement and the upper layers re-trap some of the non-wetting phase displaced from the bottom. These results also highlight the shortcomings of using the Land trapping model to characterize systems where the trapped saturations achievable are a strong function of rock heterogeneity.

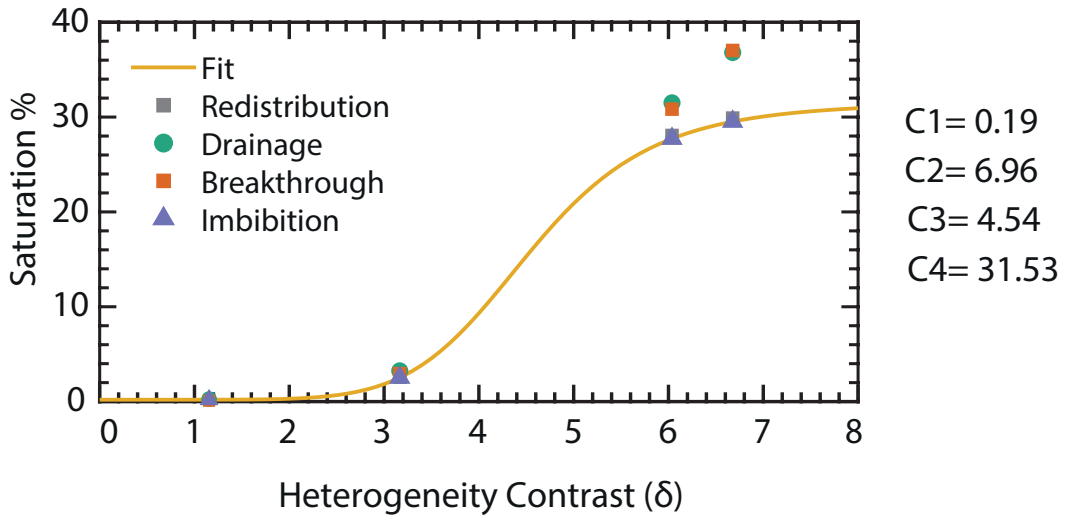

Figure 4.9: Non-wetting phase saturations measured at the end of the four stages of the experiments as a function of the grain size heterogeneity contrast. The trapped saturation (Imbibition) data can be described by a 4 parameter regression model

4.2.7 One model to describe them all?

After conducting a series of experiments with systematically varying heterogeneity, we plot (Figure 4.9a) the trapped saturations as a function of the grain size heterogeneity contrast (δ). These results can be described by a 4-parameter regression model very similar to the one used in the second chapter (Figure 4.9b) to fit the results from the numerical simulations.

$$\langle S_{NWP} \rangle(\delta) = C_4 + \frac{C_1 - C_4}{1 + \left(\frac{\delta}{C_3}\right)^{C_2}} \tag{4.5}$$

There, we hypothesized that the coefficients C3 (inflection point) and C4 (maximum asymptote) are a function of the geometry of the system. While we could not verify this claim by conducting experiments with different geometries, we comment on this dependence in light of our observations in this chapter. We also plot the saturations at the end of breakthrough, drainage and redistribution in this figure. Observing the drainage and breakthrough saturations we find that they do not plateau and instead display an upward trend. The final, trapped saturations reach a stable plateau due to the non-wetting phase being displaced in the case with the highest heterogeneity contrast during redistribution. As we discussed in section 5, this drastic reduction is brought about possibly due to the height of the bedding layers restricting the back-filling height and the resulting increase in vertical connectivity of the non-wetting phase during redistribution. This is one example of how geometric features can influence trapped saturations, and we believe, a partial validation

of our hypothesis that the asymptotic saturation is controlled by the structural aspects of heterogeneity.

4.2.8 Comparison with Numerical Simulation Results

Figure 4.10 shows the regression model fitted to the experimental (0.6 m $\times$ 0.6 m $\times$ 0.02 m) results alongside those from the REV (0.202 m $\times$ 0.202 m $\times$ 0.202 m) and full scale invasion (0.99 m $\times$ 0.8 m $\times$ 0.28m) percolation simulations from Chapter 2. The structure of the beadpacks is closest to the architecture of Model No. 5 from the simulations. We observe that the maximum asymptotic saturations from the experiments are lower than that the REV scale simulations and slightly higher than those from full scale simulations. The inflection point of the experimental predictive model is closer to the full scale simulations and higher than that of the REV scale. These observations can be understood considering the boundary effects and the difference in dimensionality between experiments and simulations.

As discussed in Chapter 2, the REV scale saturations are higher and the inflection point values are lower compared to full scale experiments since the smaller lateral extents combined with the closed boundaries at the REV scale cause more back-filling (see section 2.8). Similarly, the closed boundaries (also see: experimental limitations section in appendix, section 4.4.1) and the lack of connectivity along the third dimension leads to larger saturations in experiments compared to full scale simulations. A point to be noted is that the experiments account for non-wetting phase lost during redistribution and

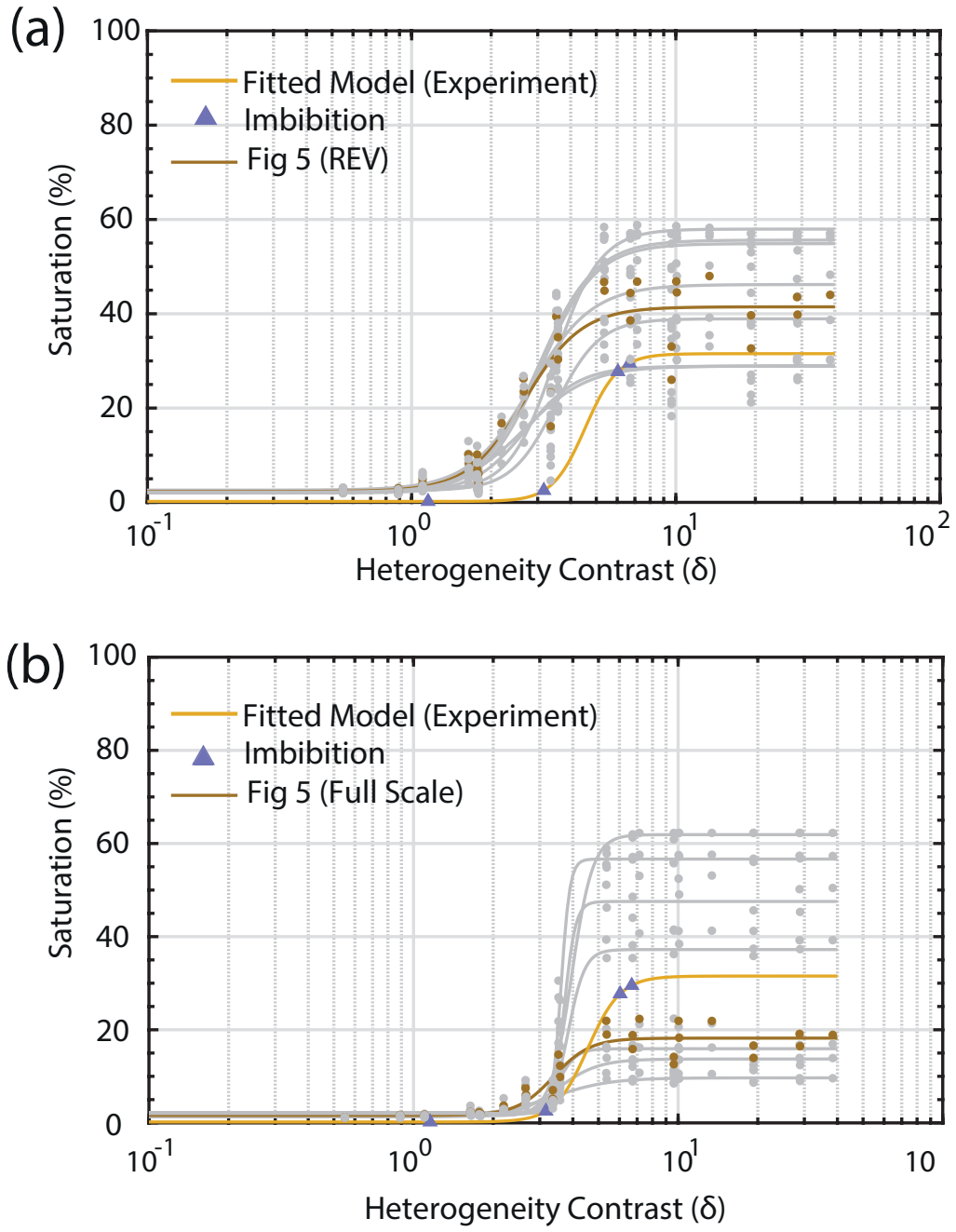

Figure 4.10: Regression model fitted to experimental data plotted alongside results from invasion percolation simulations of CO_2 migration in different bedform models (borrowed from Chapter 1) at the (a) REV scale (0.202 m $\times$ 0.202 m $\times$ 0.202 m) and (b) Full scale (0.99 m $\times$ 0.8 m $\times$ 0.28m)

imbibition whereas the simulations don't.

4.2.9 Implications for Large Scale Storage

Until now we have seen how the inherent heterogeneity of clastic rocks can impart complex spatial and temporal variability to buoyant CO_2 migration behavior at the intermediate scale (mm to dm). Will these small scale heterogeneities however impact large scale (reservoir to basin) CO_2 storage?

The most obvious takeaway from our results is the significant effect of such heterogeneities on non-wetting phase trapped saturations. Considering how commonly these depositional features (ripples, dunes and cross beds) occur in fluvial depositional environments (Reineck and Singh, 1980) at length scales ranging from 10 to 1000s of feet, combined with previous evidence from field observations, we feel safe to speculate that their impact on trapped saturations will scale up. Hence, we believe that accounting for the contribution of local capillary trapping (LCT) on storage capacity estimates is essential. CO_2 storage capacities are usually estimated using volumetric calculations (static) or reservoir simulations (dynamic). The predictive model proposed in this dissertation falls into the former category. Previously proposed static capacity estimation methods rely on an efficiency factor to determine the final storage capacity. This efficiency factor accounts for the plume footprint and the CO_2 displacement efficiency which is a function of the brine residual saturation. The efficiency factor proposed by USGS in 2010 which has been used in numerous studies (Gorecki et al., 2015) does not account for any trapping

mechanisms. Juanes et al. (2010) proposed a storage efficiency factor based on residual trapping capacity. This also accounted for the plume footprint (1D) which was calculated analytically. Iglauer et al. (2011) similarly proposed a capillary trapping capacity based simply on the porosity of the rock and the CO_2 residual saturation. Using grain size data and sedimentological descriptors of heterogeneity, storage capacity that accounts for both residual and local capillary trapping can be estimated using the model proposed in this thesis.

The other crucial influence of these heterogeneities is on the large scale migration pathways. The experimental results show how the foreset laminae orientation dictate the direction of plume development. In our experiments, the vertical migration of the NWP is partly influenced by the closed lateral boundaries. In real saline aquifers or reservoirs, the plume will continue to move laterally and vertically in the direction of the foreset laminae. Thus even at the highest heterogeneity contrasts, the sweep efficiency may not be as high as observed in our experiments. Thus ascertaining the plume footprint in such complex heterogeneous formations becomes necessary before using the trapping efficiency factor to determine the trapped capacity. Our full scale simulations in Chapter 1 mitigate this shortcoming reasonably, but are unable to capture the dynamic effects (seen in experiment A and B) that can lead to the formation of new pathways, as well as the effect of imbibition on trapped saturations. Integrating the trapping efficiency factors (Figure 4.7a) obtained from experiments with the regression model coefficients from the full scale 3D

simulations, similar to how trapping models are used to parameterize relative permeability curves (Krevor et al., 2015), is one way to overcome this limitation .

4.3 Conclusions

In this chapter, we perform gravity unstable, two-phase flow experiments at the intermediate scale in complex heterogeneous media that mimic natural depositional fabrics. We use the light transmission visualization technique to quantify fluid saturations. The most striking observation from this work is the dramatic effect subtle changes in the grain size contrast can have on non-wetting phase saturations and migration pathways. From the lowest to the highest grain size contrast explored in these experiments, the capillary entry pressure contrast spans merely from 50 to 350 Pa, but the corresponding saturation response and breakthrough times range from 0.2 to 36 %, and from 6.5 to 3300 minutes respectively. These experiments underscore the importance of accounting for capillary entry pressure variability when studying such flows. At low grain size contrasts, gravity fingers dominate and the non-wetting phase contacts very little of the pore space before breakthrough resulting in poor saturations (<1%). With increasing grain size contrast, capillary heterogeneities subdue the destabilizing gravity forces, and effects of the underlying geometry of the packing start to become apparent, causing backfilling and lateral migration of the invading phase which subsequently leads to larger saturations. The trapped saturations post redistribution are also seen

to increase with increasing grain size contrasts, but at high saturations, connectivity effects lead to reduction in trapping efficiency. The minimal effect of forced imbibition on trapped saturations seen here illustrates the persistence of local capillary trapping in such complex heterogeneous media. We find that the non-linear relationship between non-wetting phase trapped saturations and the heterogeneity contrast can be described by a 4-parameter regression model, like the one employed in the first chapter. After accounting for the effects of boundary conditions and difference in dimensionality, the experimental and simulation results seem to be reasonably comparable. The observations from the experiments presented in this chapter can help bridge understanding between core scale and reservoir scale observations.

4.4 Appendix

4.4.1 Experimental Limitations

The height of back-filling and pooling typically reduces as the invading phase moves to the upper bedding layers in these experiments. This is an artifact of dry packing and is caused by differential compaction of the layers. This effect can be seen in experiments B to D, especially in the top most layer.

In these experiments, due to the closed lateral boundaries the displaced wetting phase is forced to exit the system from the top. In natural settings however, the lateral or downward movement of the in-situ brine is likely to be more favored. This downward movement of the brine causing re-invasion of the pore space at the tail end of the migrating CO_2 plume results in residual

trapping. The redistribution phase of the experiment was designed to mimic this flow behavior.

Batch to batch differences in surface properties/impurities were observed in the glass beads obtained from potter industries. This affected the wettability and capillary entry pressure of these beads. All the experiments in this chapter were conducted using beads from the same batch. However repeat experiments could not be done since the beads from the original batch were exhausted. The compulsion to use beads from the same batch also influenced the choice of bead sizes in the next chapter.

4.4.2 Effect of Competing Heterogeneity

In Chapter 1 (section 1.8), we pointed out that the inclination or the dipping angle of the bedding planes in the REV and Full scale models can impact the end saturations. The CO_2 will migrate preferentially in the up dip direction and build buoyancy head more easily compared to the models where the beds are horizontal. This eventually leads to faster breakthroughs and lower saturations. This can be seen in the full scale model saturations (Figure 2.10). Bryant et al. (2006), in their reservoir scale simulations report similar behavior in the case with anisotropic dipping formations.

In order to test these simulation results, we generated a cross-stratified beadpack with dipping bedding layers (Figure 4.11). The cross-strata are formed in the up-dip direction like in natural environments. The bead pair used for this experiments is the same as in Case B (coarse μ =0.689 mm and

fine $\mu = 0.457$), resulting in a heterogeneity contrast (δ) of 644.

Figure 4.11a and b shows the invasion sequence at the end of breakthrough and drainage along with the breakthrough time. The saturation map at the end of drainage is shown in Figure 4.11c. The breakthrough time here is higher than that in Case B. Post breakthrough, the non-wetting phase pathways get ramified resulting in a higher saturation (4 %) compared to case B (3.2%). While the non-wetting phase pathway did get re-directed because of the dip in the bedding layers, the end saturation turned out contrary to what was observed in the IP simulations. This is because of the opposing orientations of the cross-strata laminae and the bedding layers. The competing laminae (foreset vs horizontal) directions lead to more branches and increase in lateral migration.

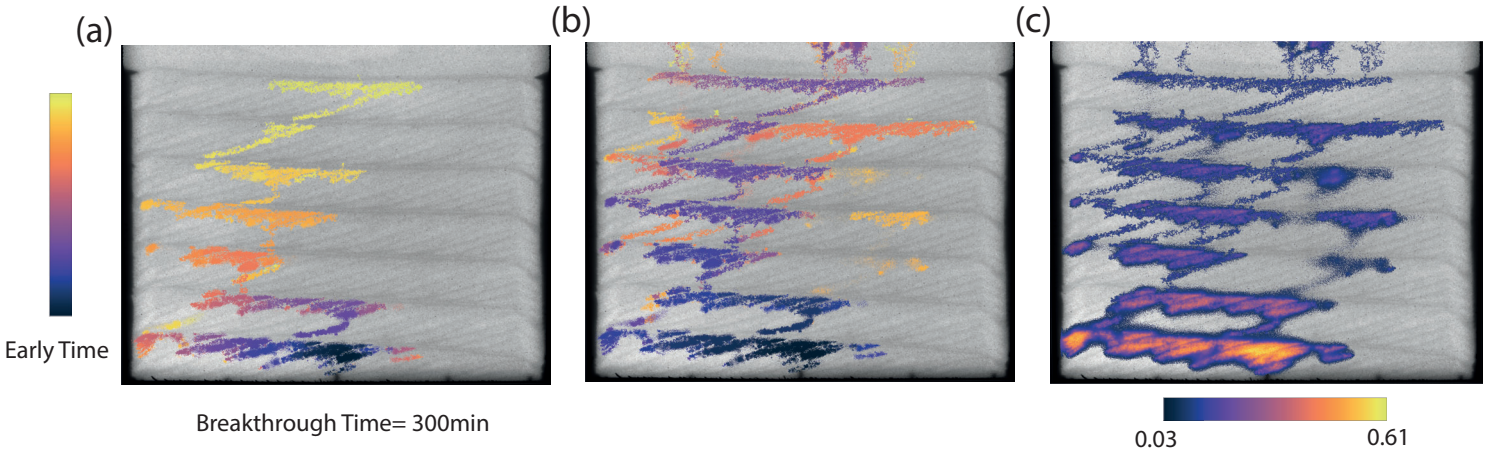

Figure 4.11: Time sequence maps of invasion showing the evolution of non-wetting phase flow at the end of (a) breakthrough and (b) drainage. The cooler colors represent early time. (c) Saturation map at the end of drainage

However, one thing to keep in mind is that the IP simulations are

performed in 3D domains whereas the experiments are 2D. In IP, the coarse regions between the foreset laminae are connected in the 3D dimension, as a result of which the invading phase is able to move along the direction of the dip without any interruptions. That is not the case in 2D. Thus the disparity in the behavior between REV scale models, full scale models and experiments is a combination of boundary effects and connectivity due to difference in dimensionality.

4.4.3 Light Transmission Visualization

The non-wetting phase saturation was measured using the light transmission visualization (LTV) method. In this technique, the extent of attenuation of light intensity due to the presence of the dyed non-wetting phase is used as a proxy for saturation. LTV was originally developed by Tidwell and Glass (1994) and later reworked by Niemet and Selker (2001) to account for both absorption and refraction of light. We use a modified formulation proposed by Bob et al. (2008) Previously, LTV called for an initial calibration step, wherein the packing needed to be completely saturated with the non-wetting phase to acquire the reference image. The modified method replaces this with a simpler calibration step that is done during the experiment. Without a calibration curve, the modified LTV method allowed the calculation of saturations, pixel wise across the 2-D packing. A complete development of the method is provided elsewhere (Niemet and Selker, 2001; Bob et al., 2008). We describe some of the important assumptions along with the corresponding

equations.

When light passes through the slab chamber, the different phases absorb different amounts of light. Absorption by the transparent aqueous phase is negligible but the glass beads and and dyed non-wetting phase absorb light depending on their optical properties. At the interface between these phases, the light gets refracted. The losses due to absorption and refraction can be determined using Beer's law and Fresnel's law. For a two phase system, the light intensity is given as:

$$I = I_{\mathrm{in}}\, \tau_{\mathrm{pw}}^{2K} \tau_{\mathrm{wo}}^{2K(1-S)} \mathrm{e}\left(-\alpha_{\mathrm{p}} d_{\mathrm{p}} k_{\mathrm{p}} - \alpha_{\mathrm{o}} d_{\mathrm{o}} k_{\mathrm{o}}\right) \tag{4.6}$$

Where I and I_{in} are the emergent and incident light intensities, $T_p w$ and $T_w o$ are the transmission factors at the particle-aqueous phase and water-heptane interface, α_p and α_o are the absorption coefficients of the particles and oil respectively, d_p is the average particle diameter, d_o is the average pore diameter, k_p is the number of particles across the chamber, k_o is the number of non-wetting phase filled pores, K is the number of pores across the thickness of the chamber and S is the fraction of pores filled with the aqueous phase. The pores are assumed to be filled completely either with the wetting or the non-wetting phase.

Substituting $S = 1$ and $S = 0$, in the above equation, we obtain the expressions for light intensities when the pores are filled with completely with the aqueous phase and non-wetting phase respectively.

$$I_{\mathrm{s}} = I_{\mathrm{in}} \tau_{\mathrm{pw}}^{2K} \mathrm{e}\left(-\alpha_{\mathrm{p}} d_{\mathrm{p}} k_{\mathrm{p}}\right) \tag{4.7}$$

$$I_{\mathrm{oil}} = I_{\mathrm{in}}\, \tau_{\mathrm{pw}}^{2K} \tau_{\mathrm{wo}}^{2K} \mathrm{e}\left(-\alpha_{\mathrm{p}} d_{\mathrm{p}} k_{\mathrm{p}} - \alpha_{\mathrm{o}} d_{\mathrm{o}} K\right) \tag{4.8}$$

Dividing equations 7 and 8, we obtain an expression for the non-wetting phase intensity as a function of the wetting phase intensity:

$$I_{\mathrm{oil}} = I_{\mathrm{s}} \tau_{\mathrm{wo}}^{2K} \mathrm{e}\left(-\alpha_{\mathrm{o}} d_{\mathrm{o}} K\right) \tag{4.9}$$

With further algebraic manipulation, an expression for the non-wetting saturation at each pixel can be obtained as :

$$S_{\mathrm{o}} = \frac{\ln I_{\mathrm{s}} - \ln I}{\ln I_{\mathrm{s}} - \ln I_{\mathrm{oil}}} \tag{4.10}$$

Where I_S is intensity when the chamber is fully saturated with the aqueous phase, I_{Oil} is the intensity when the chamber is completely saturated with the non-wetting phase and I is the intensity map of the chamber at which the saturation needs to be measured.

I_S was measured at the initial state of the system prior to drainage. Experimentally measuring I_{Oil} required saturating the packing entirely with dyed heptane before each run. To circumvent this cumbersome and impractical step, I_{Oil} was calculated theoretically using equation 9. The other parameters needed for this calculation are obtained as follows.

The total number of pores across the thickness of the chamber K was calculated using the dry and saturated intensities as given by (Neimet and Selker):

$$K = \frac{\ln\left(\frac{I_{\mathrm{a}}}{I_{\mathrm{a}}}\right)}{2\ln\left(\frac{\tau_{\mathrm{FS}}}{\tau_{\mathrm{p}}}\right)} \tag{4.11}$$

The transmission factor between the two phases can be obtained from their respective refractive indices using Fresnel's's law:

$$\tau = \frac{4n_1 n_2}{(n_1 + n_2)^2} \tag{4.12}$$

The total length of the pores or voids across the thickness was given by the product of the porosity and the thickness of the chamber (2 cm). This divided by the total number of pores K gave the pixel averaged pore diameter.

4.4.3.1 Absorbance Measurement

To calculating the I_{Oil} theoretically, the absorption coefficient (cm^{-1}) of the non-wetting phase is needed. The absorption coefficient is given by:

$$\alpha_o = \frac{2.303A}{L} \tag{4.13}$$

Where A is the absorbance of the dyed heptane and L is the path length of light. The absorbance was measured using a UV-Vis spectrophotometer. The path length was determined by the cuvette used for the measurement. The

value at peak absorbance wavelength (520 nm) was used for the calculations. This combined with the 520nm bandwidth filter used during imaging, helped ensure accuracy of the calculations.

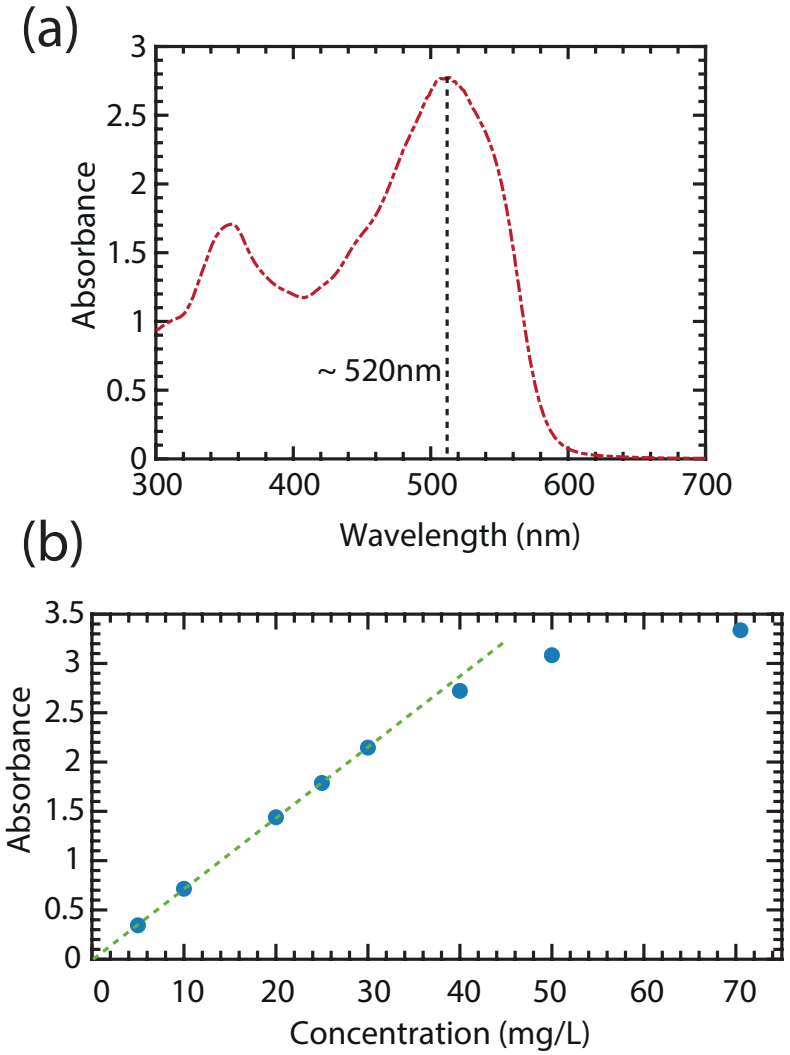

Figure 4.12: (a) Absorbance curve of Oil Red O dyed heptane (40 mg/L). The peak absorbance occurs around 520 nm. (b) Absorbance as a function of dye concentration. Linearity is lost after 40 mg/L

Since the saturation calculation relied on the absorption coefficient, necessary care was needed while deciding the dye concentration to ensure error free absorbance measurement. At high concentrations, the Beer Lambert's law that correlates absorbance and dye concentration loses its linearity and the measurements become noisy. To maximize the contrast while imaging, the concentration chosen had to be close to the highest possible value in the linear range. To determine the maximum usable value, the absorbance-concentration curve was generated for cuvettes of different path lengths. The concentration at which the curve deviated from linearity was chosen (Figure 4.12), which in this case was 40 mg/litre.

4.4.3.2 Calibration and Accuracy

The only remaining unknown for the calculations was the refractive index of Oil Red O dyed heptane, needed to determine the transmission factor between the aqueous and non-wetting phases. To overcome this, the transmission factor was determined using a mass balance calibration, against a known amount of heptane that enters the system at the beginning of the invasion. This value of T_wo was then used for the rest of the experiments. When the major constituent of the bead mixture was changed (Chapter 4), T_wo had to be re-calibrated.

One of the main source of errors in LTV is the random noise in the camera signal. To reduce this we follow a solution proposed by Bob et al., 2008. The equations developed in the previous section were used to determine the

pixel wise saturation when just a single pore is saturated with the non-wetting phase (by substituting $K=1$) for each experiment. This value was then used as the threshold, below which the saturations calculated were neglected. CCD camera sensors usually have imperfections like hot pixels which can manifest as noise or false positive saturations. To avoid this, a baseline correction for hot pixels was done by subtracting an image taken with the same exposure time but with the lens cap on.

The accuracy of the LTV method was evaluated by a simple mass balance. Figure 4.13 shows the plot of the measured values of the non-wetting phase volumes against the injected volumes for three experiments. Across all experiments, measurement accuracy in the range of 90 to 95% was achievable using this technique.

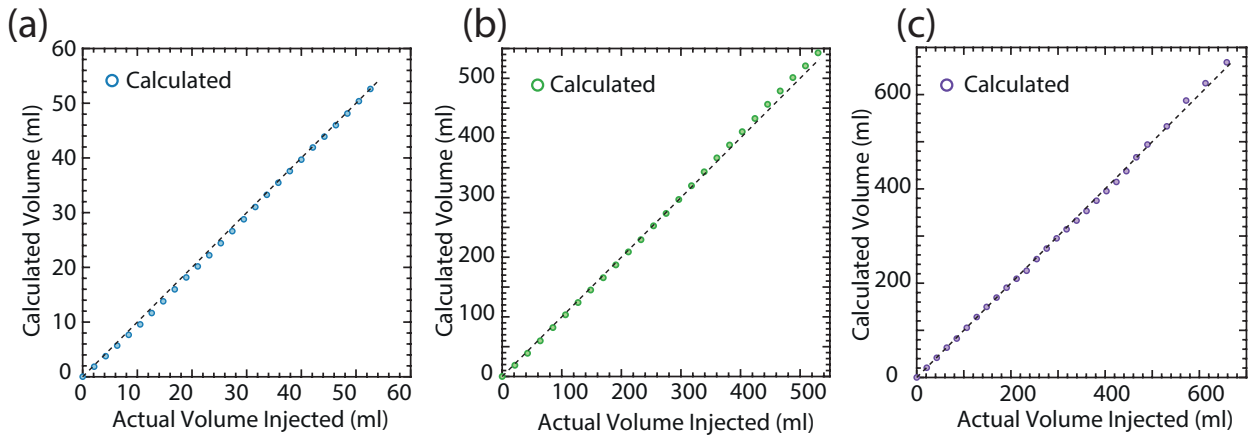

Figure 4.13: (a)-(c) Heptane volume calculated using LTV versus actual heptane volume injected in experiments B,C and D

4.4.3.3 Image Analysis: Image Registration

In this technique, we dry pack the slab chamber using the filling apparatus and later saturate the pack with the aqueous phase. During the flooding step, due to the hydrostatic pressure and cohesive forces of the wetting phase, the packing undergoes compaction. Since the difference between the dry and saturated images is required in the LTM calculations, the compaction of the packing results in pixel-wise mismatch resulting in deviations up to 1.5 to 2 cm during the calculations. In order to overcome this challenge, we use image registration to align the dry and wet images. We use the imwarp and imregister functions in MATLAB to correlate the pixels in the two images based on the structural features and apply a geometric transform to register the dry image with the saturated one.

4.4.4 Capillary Entry Pressure Measurements

The capillary entry pressures of the glass beads used in the flow experiments were measured using a technique proposed by Mori et al., (2015). The method was developed specifically to measure the entry pressures of fluids less dense than water (LNAPLs). The experimental setup consists of a 1 litre borosil measuring cylinder modified to have an outlet at the bottom, connected to a constant head device (25 ml glass measuring cylinder with an outlet at the bottom). The cylinder was wet packed tightly with the glass beads. A fritted glass disc was placed at the bottom to prevent entrainment of the beads. The position of the connected constant head cylinder was adjusted

such that it has the same height as the saturated beads. The dyed heptane was then added to the cylinder in increments of 1 cm height every 6 hours. As the heptane pressure increases, it begins to invade the beads and the aqueous phase gets displaced and overflows from the constant head device. At a certain height, the volume displaced suddenly increases which is then identified as the displacement/entry pressure.

4.4.5 Land Trapping Model Coefficients

Table 4.5: Land Trapping Model Coefficients

Layer No.	Experiment A	Experiment B	Experiment C	Experiment D
1	10.79	1.32	0.55	0.71
2	2.35	0.18	0.04	0.6
3	1.36	1.97	0.30	0.33
4	1.72	2.43	0.26	0.21
5	1.63	0.39	0.16	0.07
6	1.35	0.52	0.16	0.07
7	1.98	-0.04	0.1	0.41

4.4.6 Supplementary Images

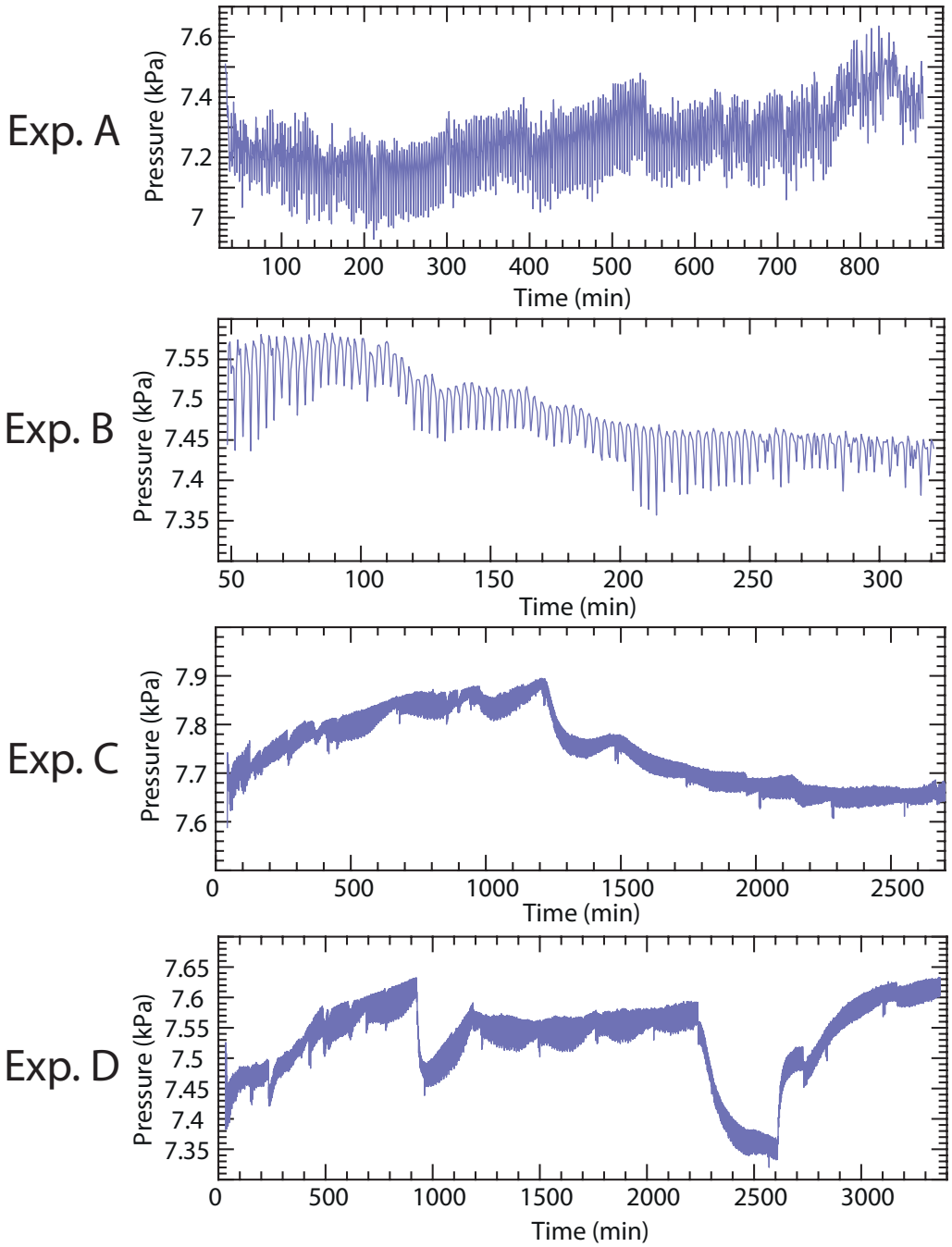

Figure 4.14: Difference between inlet and outlet pressures as a function of time for the four experiments

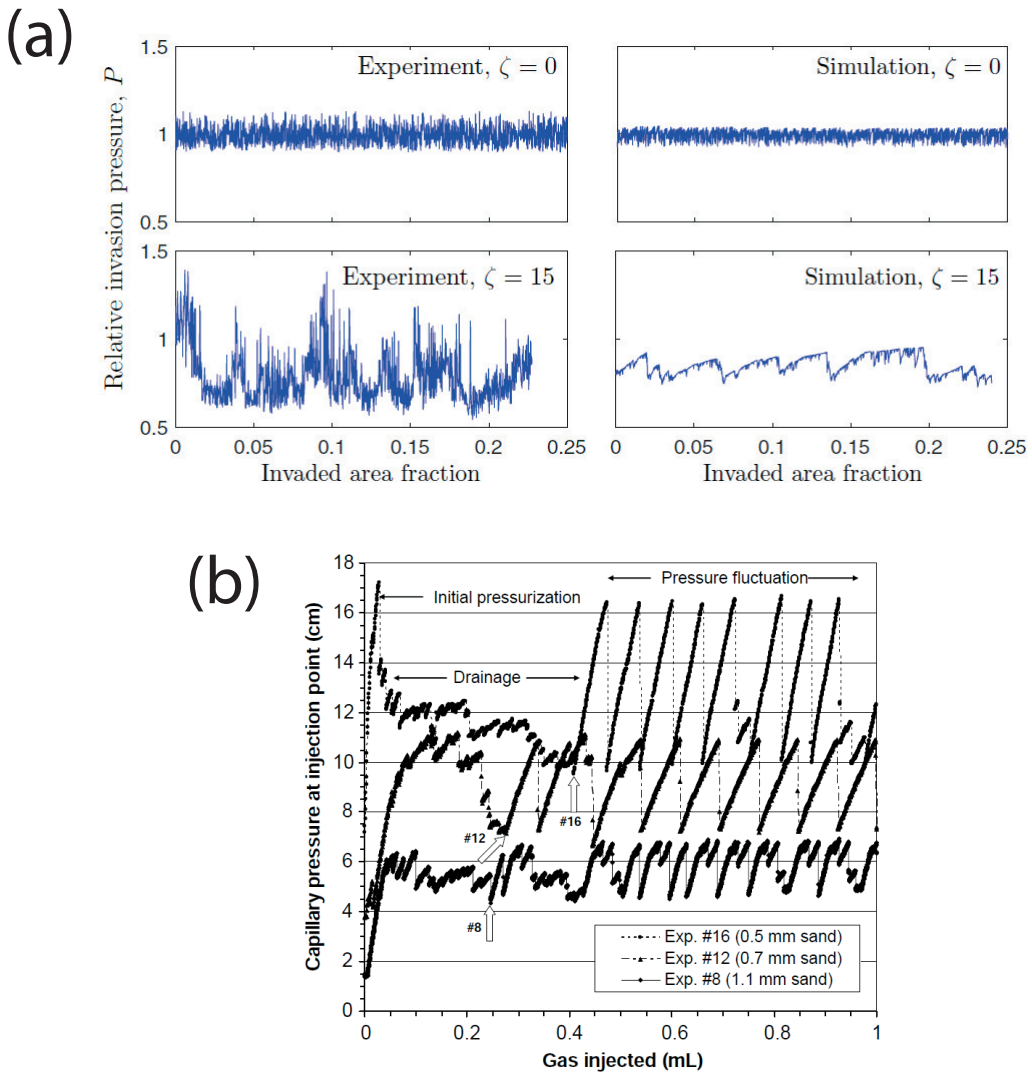

Figure 4.15: (a) Fluid pressure fluctuations during drying in a porous medium with uncorrelated and correlated pore sizes in experiments and invasion percolation model. Adapted from Biswas et al., 2018 (b) Inlet pressure readings during slow gas injection in porous media. The three curves indicate three experiments with different grain sizes. Adapted from Mumford et al. 2008

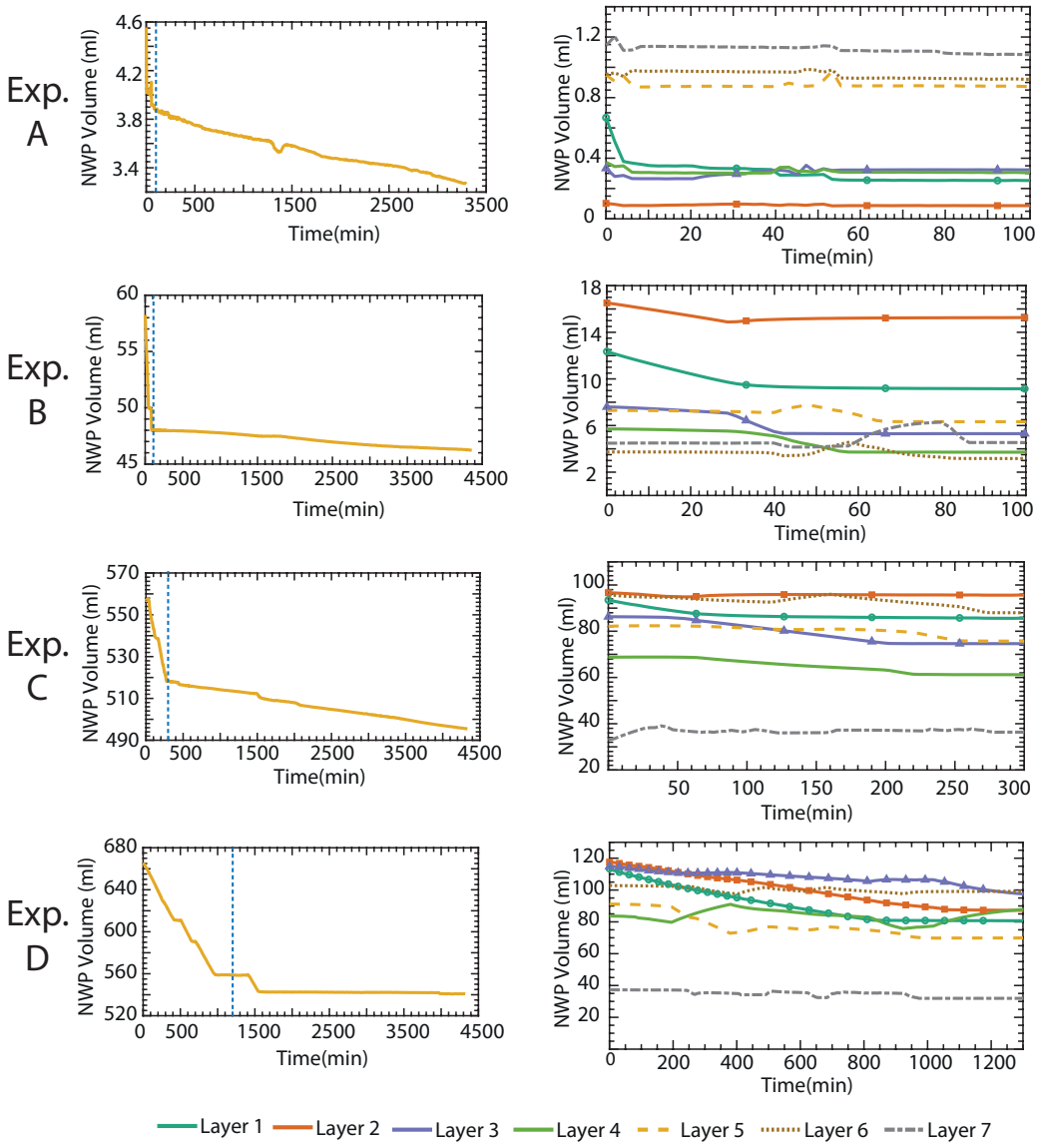

Figure 4.16: Left Column: Total non-wetting phase volume as a function of time during the redistribution phase. The blue dotted line indicates the point in time when there is marked change in the displacement/escape rate. Right column: Layerwise non-wetting phase volume as a function of time during high displacement rate regime

Chapter 5

The Effect of Flow Rate on Displacement Efficiency and Trapping

In the previous chapter, we experimentally studied the effect of geologic heterogeneities on invasion patterns and trapping behavior of CO_2 during vertical migration. Using the same experimental techniques, in this chapter, we investigate the effect of flow rate / capillary number on gravity unstable immiscible displacement. Traditionally, the effect of capillary number on subsurface multiphase flows has been studied in the context of water flooding (Imbibition) for oil recovery. The effectiveness of water flooding is usually described by a plot between the imbibition capillary number and the residual non-wetting phase saturation left behind, known as the capillary desaturation curve. In this chapter we consider the opposite case: a capillary number-based assessment of the effectiveness of buoyant, non-wetting phase displacement (drainage) and subsequent immobilization to better understand its implications for CO_2 sequestration.

5.1 Introduction

Immiscible displacement in porous media depends on a variety of factors like viscosity, density, interfacial tension, wettability and heterogeneity. Starting from the work by Lenormand et al. 1988 there has been tremendous interest to characterize such flows based on dimensionless numbers derived by force balance: Capillary Number, Bond Number and Viscosity Ratio. The major focus of these works has been to demarcate flow regimes where one of these forces is dominant, and identifying when the transition between these regimes occurs (Ferrer et al., 2004; Wang et al.,2012; Holtzmann and Juanes, 2010; Chen et al., 2017). Our focus here however, is on the final state of the system with regards to non-wetting phase distribution and saturation, during gravity unstable vertical displacement at different flow rates/capillary numbers, in the context of CO_2 sequestration.

Majority of the previous work in this area has been done at the pore scale using micromodels (Wang et al.,2012; Zhang et al., 2011; Zheng et al., 2017; Chang et al., 2019) and microCT based core flooding experiments (Herring et al., 2015; Kimbrel et al., 2015) and Lattice Boltzmann simulations (Tsuji et al., 2016; Yamabe et al., 2015; Zacharaoudiou et al. 2018; Bakhshian et al., 2019). The common observation amongst these reports is that the CO_2 saturation at breakthrough decreases with increasing capillary numbers, while transitioning from capillary fingering to viscous fingering regime (Zacharoudiou et al. 2018, Zhang et al., 2011). At low capillary numbers, the displacement is characterized by fingers developing in directions

perpendicular and even opposite to the applied gradient, dictated by the capillary entry pressures of the pores. In the viscous fingering regime, the non-wetting phase forms discrete pathways preferentially along high permeability regions. Thus, the displacement efficiency is higher in the capillary fingering regime (Tsuji et al., 2016). Post breakthrough, the saturation at low Ca flows remains unchanged while new fingers continue to develop in the viscous fingering regime thereby resulting in higher saturations at late times or when steady state is reached. The flow regime phase diagram and the displacement efficiency however, was seen to vary as per the dimensionality and the heterogeneity of the system (Tsuji et al., 2016). Thus, how these flow patterns scale up and manifest themselves at the larger scales remains unclear.

Few studies have accounted for gravity in such flows. Muharrik et al.(2018) conducted vertical flooding in centimeter scale beadpacks and investigated capillary and buoyancy effects. They found that saturation reduced with increasing Bond number owing to gravity driven fingering. At low Bond numbers, they reported increasing saturations with increasing capillary numbers. These results are similar to those reported by Polak et al., (2011) and Cinar and Riaz (2007) who investigated vertical flooding of CO_2 into intermediate scale homogenous sandpacks. At low flow rates they observed gravity fingering and increasing the flow rate led to ramified flows with increasing displacement efficiency.

Thus, the instabilities found at the pore scale studies are found to persist at the sub-meter scale, at least in homogenous domains. Bryant et

al. (2006) simulated buoyancy dominated flows in heterogeneous domains at the reservoir scale (400 ft) and found that at the large scale, geologic heterogeneities rather than flow instabilities exert influence on flow behavior. Thus, heterogeneity representation becomes important.

Oh et al.,2015 conducted vertical CO_2 floods on heterogenous cores at different flow rates. While they observed increasing saturation, no drastic changes in the flow patterns could be observed. This was mainly due to the boundary effects and the size limitations of a rock core

In this chapter we focus on the intermediate scale behavior of such flows in heterogeneous porous media and try to answer the question: How do displacement efficiency and trapping efficiency change with flow rates. We address the three main deficiencies in previous works: a larger domain size, effect of buoyancy and realistic heterogeneity.

5.2 Methods and Materials

The experimental setup, choice of fluids, packing procedure and image analysis work-flow are all similar to that reported in the previous chapter. Here we describe only the deviations from the previous experiments.

5.2.1 Design of Heterogeneity

The heterogeneity geometry of the beadpacks is kept the same as before: crossbeddings. However, a new grain size pairing is used to generate the packs (Figure 5.1). The grain size contrast(δ=5.22) lies in between that of

experiments B and C from the previous chapter.

5.2.2 Invasion Experiments

In these experiments, the capillary number was varied by changing the flow rates. Four different flow rates ranging from 0.02 ml/min to 20 ml/ min were used. The experiments were designed to have 3 stages instead of four: 1) Injection until breakthrough; 2) End of injection after a specified time post breakthrough and 3) 72 hours of redistribution. Forced imbibition was omitted in these experiments.

In the previous chapter the injection was stopped 12 hours post breakthrough. Here that time duration varies as per the experiments. The injection

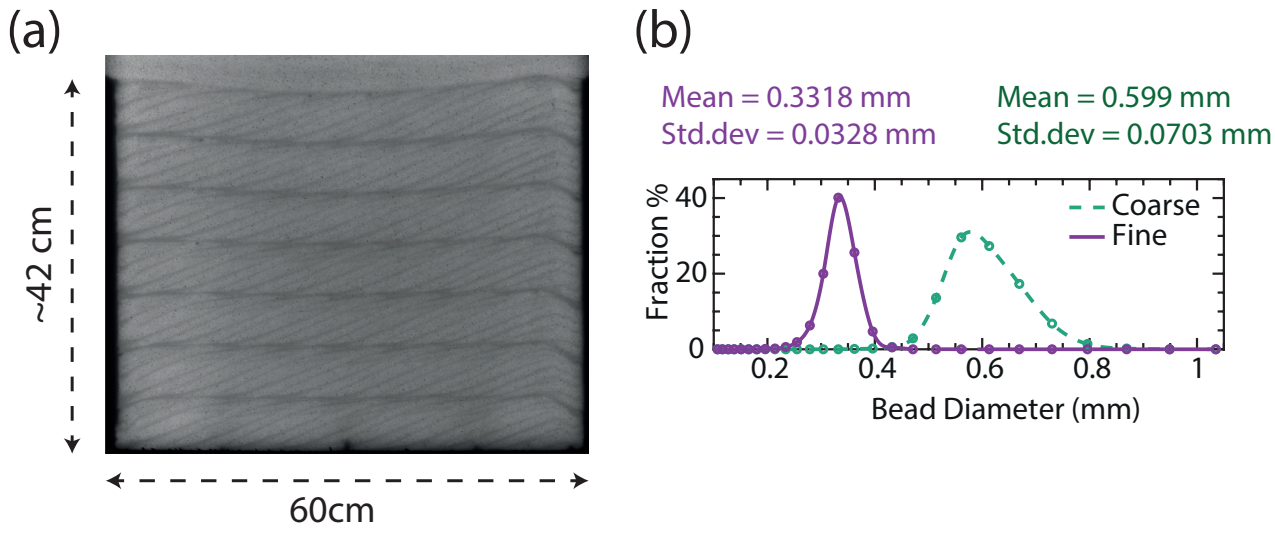

Figure 5.1: (a) Crossbedding generated using the automated packing technique for flow experiments (b) The size distributions of the bead pairs used to generate the packing

Table 5.1: Design of Experiments

Exp. No.	Matrix μ (mm)	Lamina μ (mm)	Q (ml/min)	Imaging interval (seconds)
A	Coarse (0.599)	Fine 1 (0.331)	0.02	60
B	Coarse (0.599)	Fine 2 (0.331)	0.2	30
C	Coarse (0.599)	Fine 3 (0.331)	2	5
D	Coarse (0.599)	Fine 4 (0.331)	20	5

time is changed in such a way that the non-wetting phase volume injected during the 2nd stage remains constant across experiments. The details of the experimental conditions are provided in Table 5.1.

We note an aberration in these set of experiments: In experiment B (q=0.2 ml/min), stage 2 injection could not be implemented due to unavoidable experimental challenges.

5.2.3 Imaging

In the previous chapter, the imaging was done at a constant interval of 30 seconds. Here this interval varies as per the flow rate. (Table 5.1)

5.3 Results and Discussion

5.3.1 Flow Rate Effects on Displacement

Figure 5.1 shows the invasion patterns at the end of breakthrough and drainage; from left to right, the flow rate increases by an order of magnitude in each consecutive experiment. The invasion sequence is color coded with cooler colors representing earlier times. The corresponding breakthrough times are also shown in the figures. With increasing injection flow rate, the sweep

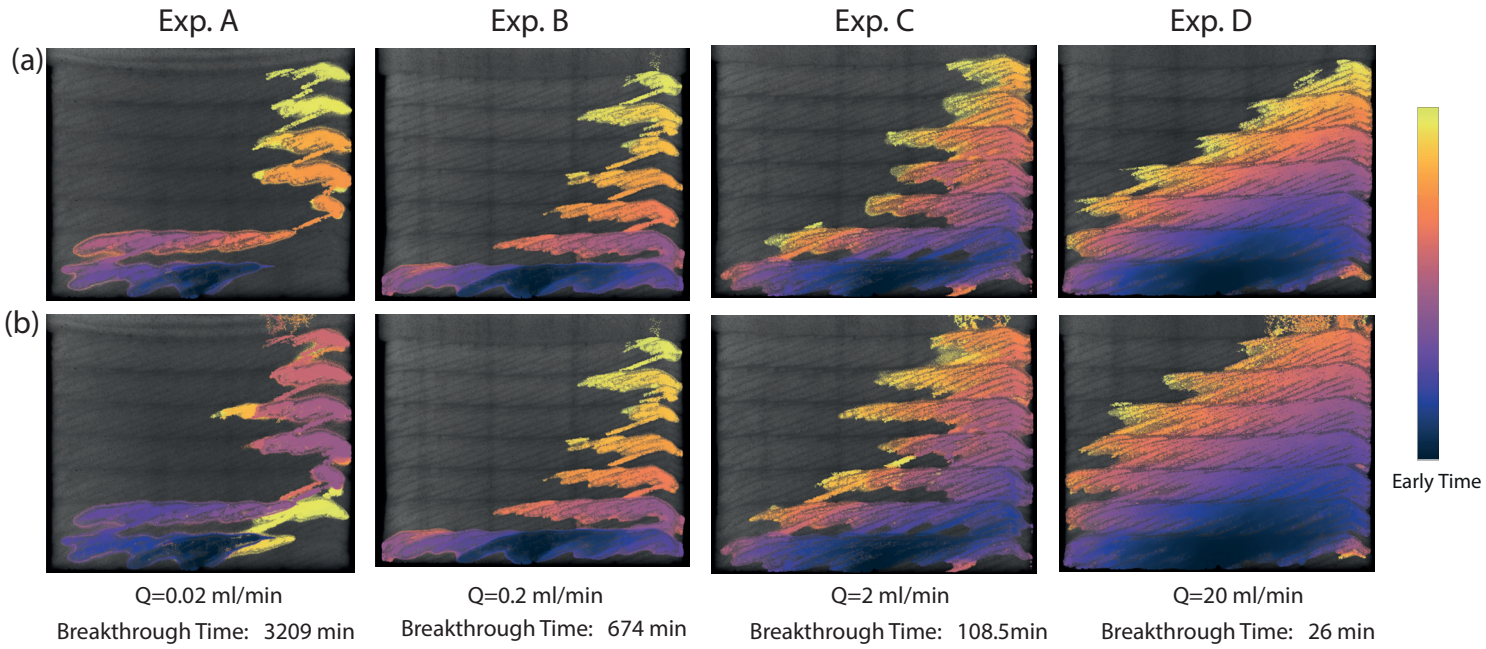

Figure 5.2: Time sequence maps of invasion showing the evolution of non-wetting phase flow at the end of (a) breakthrough and (b) drainage. Moving from left to right, the injection flow rate increases. The cooler colors represent early time.

efficiency increases, with the invasion pattern changing from capillary fingering to compact displacement.

Across all experiments, we find that the underlying geologic structure of the medium shapes the large-scale invasion behavior. There are two main heterogeneous features that influence the flow pathways: the thicker horizontal laminae bounding each bedding layer which causes backfilling; and the thinner cross-strata laminae which direct the flow to the right. Both laminae are enriched in the finer fraction of glass beads, yielding smaller pore sizes and higher capillary entry pressures than the surrounding media.

In experiments A and B, the invasion behavior is very similar to what we observed in the previous chapter: gravity unstable fingers with pooling, lateral migration and backfilling behind foreset and horizontal laminae, with each layer being breached once the capillary entry pressure is overcome. The horizontal barriers are breached at only spot (where capillary entry pressure conditions are most favorable), with a singular vertical flow front driving the migration. The breakthrough time and saturations increase from to from A to B for an order of magnitude increase in the flow rates.

When the flow rate is increased to 2ml/min (experiment C) the invading phase footprint increases, resulting in faster breakthrough and a larger saturation. Here, the flow is characterized by the front growing vertically and at the same time laterally at lower elevations. Thus, a large portion of a particular bedding layer is invaded during lateral migration after the overlying barrier has been breached, rather than during backfilling like in experiments A and

B. In this case, fingers freely develop (Figure 5.3b), branching out anywhere along the migrating plume, usually along the coarse-grained zones. Close to the inlet, the invading phase fingers are thick, spanning the width of the coarse-grained laminae, while thinner (a few pores wide) ones develop higher up. In contrast to the previous two cases, here some horizontal barriers are breached concurrently at multiple locations. The fingers entering a bedding layer from different spots merge during lateral migration and backfilling.

At the highest flow rate, the displacement efficiency is very high and the breakthrough is quick. In this case, the flow front grows in all directions with the barriers being breached easily compared to that at lower flow rates. Fingers (Figure 5.3c) at two distinct length scales are observed: a) thick fingers that propagate along the coarse-grained regions between the foreset laminae and b) a large number of thin fingers that emanate from the former. These fingers are able to break-through the foreset laminae, unlike other cases, which then grow and merge, thereby propagating lateral migration. Like in the previous case, lateral propagation occurs concurrently with vertical migration.

Even at the highest flow rates, the influence of the underlying geometry is preserved. Time lapse videos show that the vertical migration is always directed to the right due to the orientation of the cross-strata and the ensuing lateral flow within a bedding layer occurs from right to left. Thus, at the end of drainage we find that the left most portions of the packing remain un-swept. The extent of left-ward invasion increases with flow rate.

During the post breakthrough injection phase, in all three cases (A,

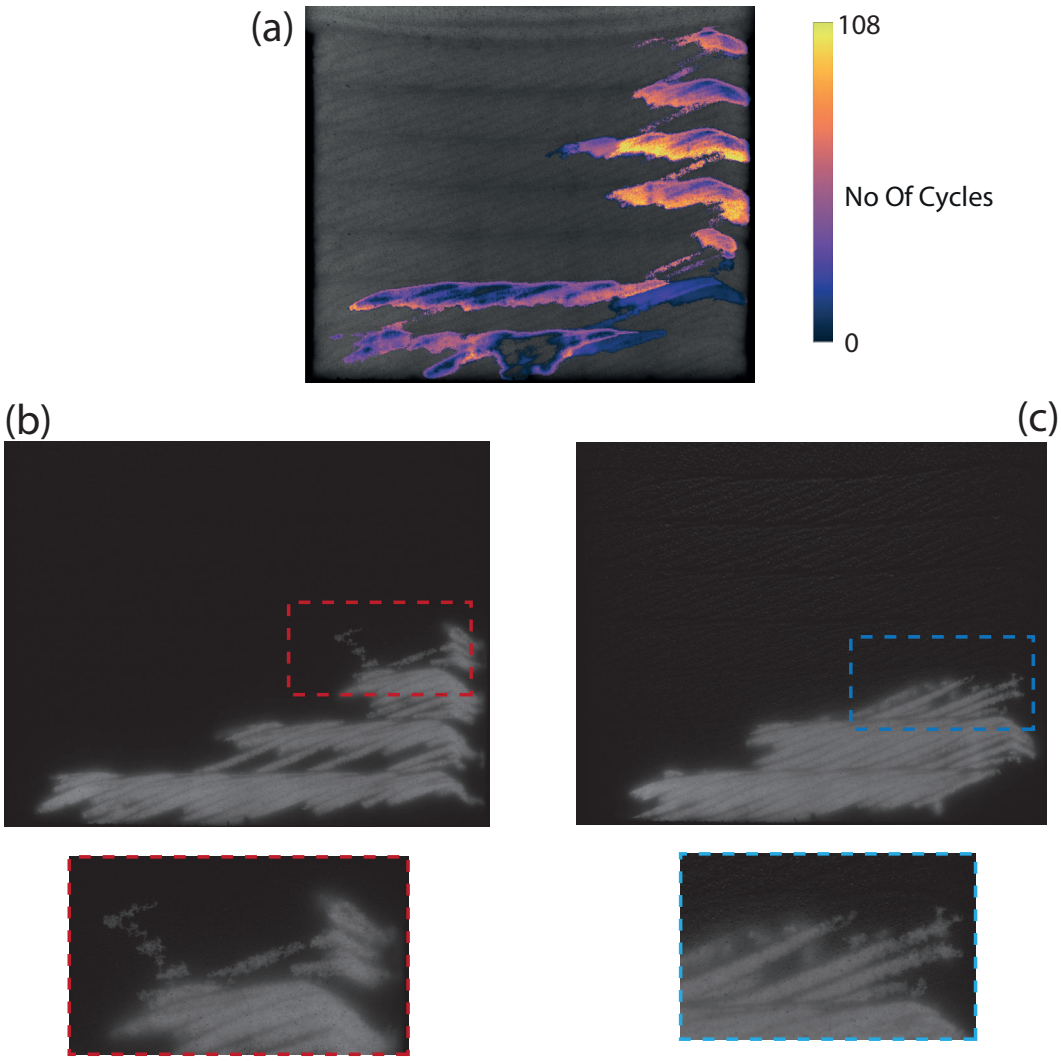

Figure 5.3: (a) Map showing cyclicity in the saturations during post breakthrough injection in experiment A. (b) Digital image of non-wetting phase migration in experiment C. The inset shows the growth of fingers (c) Digital image of non-wetting phase migration in experiment D. The inset shows finger development at two different length scales

C and D; flow was stopped after breakthrough in B) the non-wetting phase saturation continues to grow. At high flow rate experiments (case C and D), this is due to the non-wetting phase invading new pore space driven by viscous forces (Zhang et al., 2011). At the lowest flow rate however, this increase is due to the intermittency in flow. We discuss this in the next section.

5.3.2 Invasion Dynamics: Intermittency

During slow, vertical immiscible flows, local imbibition events can result in the non-wetting phase connectivity to be lost. Sometimes the connectivity is re-established and the flow continues along pre-existing pathways, while other times, the invading phase finds alternative routes and the migration pattern undergoes a change. This cyclic disconnection and reconnection of nonwetting phase leads to pulsating behavior, also known as intermittency. This intermittency due to fragmentation has been reported widely in low capillary number, buoyant flows in homogeneous media (Mumford et al., 2008; Wagner et al., 1997; Meakin et al., 1992). Glass et.al (2000) reported pulsations in their study of gravity unstable migration of CO_2 and Tetrachloroethylene (TCE) in heterogeneous sandpacks. We observe similar behavior in our lowest flow rate experiment (Case A), especially during the post breakthrough injection phase.

Pulsations occur at two scales: finger scale and pool scale. At late times, high frequency pulsations are observed in the back-filled pools beneath all seven layers. This large-scale throbbing propagates starting from the bottom layers towards the top. Glass et al. (2000) reported pool scale pulsations

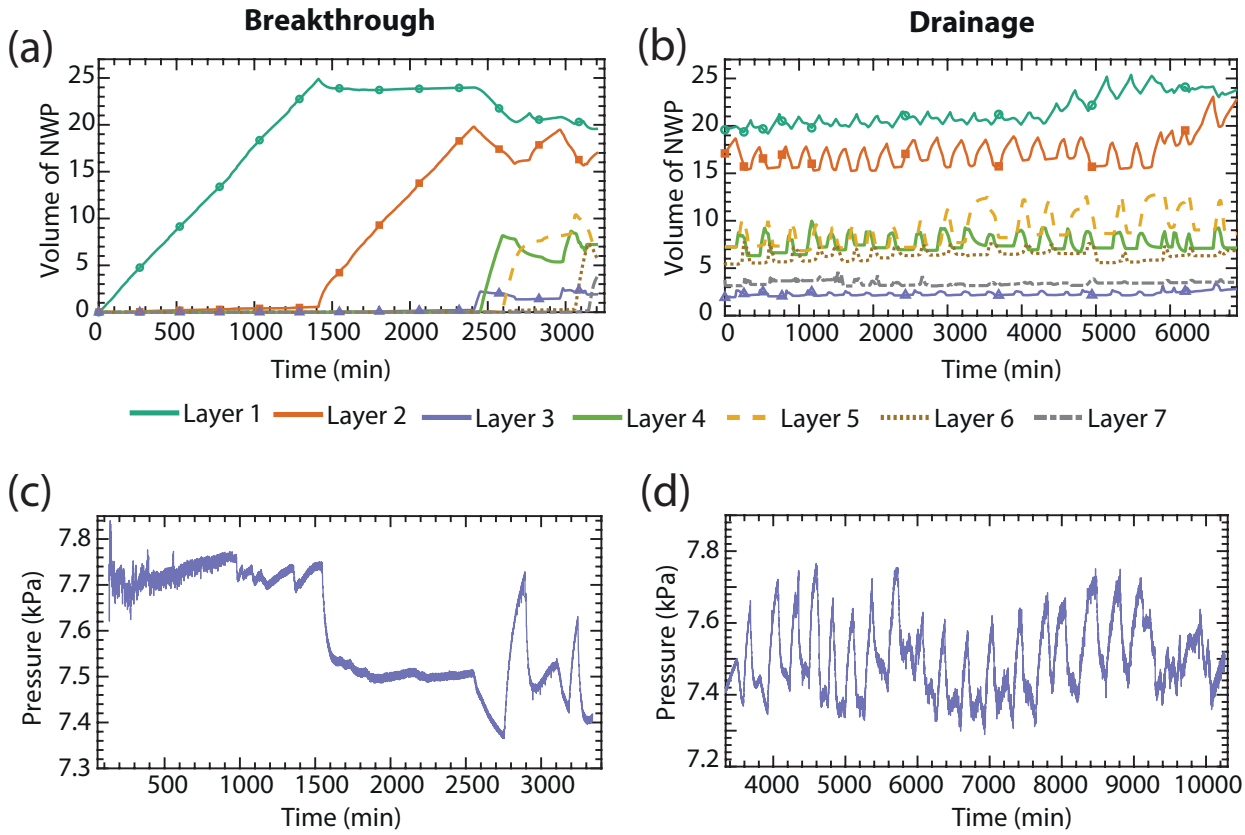

Figure 5.4: For experiment A (Q = 0.02 ml/min): Layer wise non-wetting phase volume as a function of time (a)Before breakthrough and (b)During post breakthrough injection. Pressure response signal (difference between inlet and outlet pressures) as a function of time (a)Before breakthrough and (b)During post breakthrough injection

only in the low viscosity CO_2 gas experiments and not TCE. Our experiments however were conducted at much lower flow rates (0.02 ml/min compared to 1ml/min) compared to theirs. The fluctuations in the light intensity due to intermittency in the flow during the post breakthrough injection period is visualized in Figure 5.4. The cyclic saturation variations during pulsation can also be seen in the plot showing the evolution of layer-wise non-wetting phase volumes. We also plot the difference between the inlet and outlet pressures as a function of time. The loss of connectivity and the capillary pressure buildup during reconnection is reflected in the pressure response curves.

Intermittency also leads to the formation of new pathways. This causes the older pathway to get isolated and the flow continues via the newly the formed one. New pore space being invaded contributes to the overall non-wetting phase saturation. Large scale (cm scale) intermittency was also seen in our low heterogeneity contrast experiments in the previous chapter. Here it gets manifested at higher heterogeneity contrasts, but only at flow rates lower than that of previous experiments.

5.3.3 Flow Regimes

We attempt to characterize the flow regimes based on solely the capillary number (Ca) since the bond number (Bo) remains unchanged across these experiments. In experiments A and B, we used the average front finger velocity to calculate Ca. In the case of C and D, since the non-wetting phase grows asymmetrically in all directions at the same time, we were unable to calcu-

late the front velocities. The average capillary number in Case A (6.48E-7) is lower than that of B (3.65E-6), reflecting the lower flow rate. In experiment A, we occasionally observed sudden bursts of finger growth, where the velocity increased by an order of magnitude or more. We discard these values when averaging since they skew the results. The calculated values clearly indicate that experiments A and B lie in the capillary dominated regime. Based on visual cues such as the development of increasing number of fingers (indicative of viscous fingering), we speculate that the cases C and D operate close to the capillary to viscous crossover regimes.

5.3.4 Redistribution and Trapping

During redistribution, the counter current flow of the aqueous phase leads to reinvasion of some of the pore space occupied by the invading phase. Non-wetting phase saturations at the end of drainage and redistribution are shown in Figure 5.5. The saturation difference between the two stages is shown in Figure 5.6.

As the figures show, the non-wetting phase retained by the capillary heterogeneities decreases progressively with increasing flow rates. However, at the lowest flow rate (case A), we see almost no change in the saturations after redistribution. Thus, all the non-wetting phase remains trapped at the end of redistribution or natural imbibition. Comparing this to our results from the previous chapter, there, even at higher capillary entry pressure contrasts, we found non-wetting phase being mobilized during redistribution.

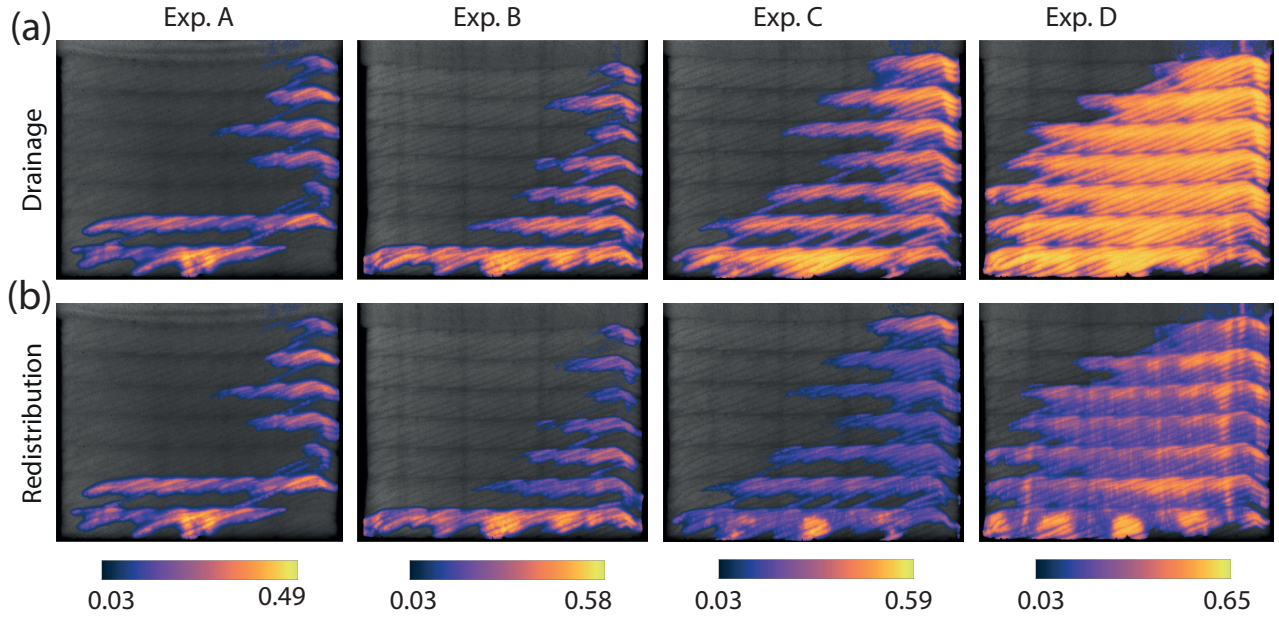

Figure 5.5: Non-wetting phase saturation for the four experiments at (a)End of Drainage and (b) End of Imbibition. From left to right (A to D) the injection flow rate increases.

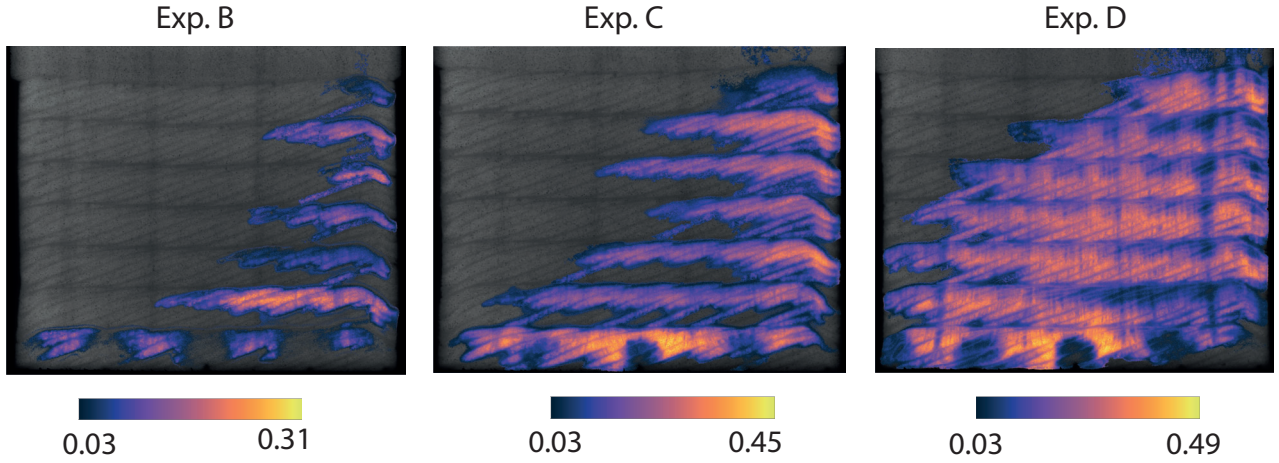

Figure 5.6: Difference between drainage and redistribution saturations for three experiments. In experiment A, non-wetting phase in not displaced during redistribution. The image shows the non-wetting phase that has been displaced and has left the system.

Glass et al. while studying CO_2 and TCE migration in heterogeneous porous media found that viscous dissipation led to increase in backfilling heights of TCE than that predicted by the capillary entry pressures of the barriers. Subsequently during redistribution, the excess TCE escaped leading to smaller pool heights. This is a plausible explanation as to why in the lowest capillary number flows (low viscous influence), we find no loss in the non-wetting phase and at higher capillary pressures, as the viscous forces grow significant, the losses increase during redistribution.

Another possible explanation for the increase in losses is the enhanced vertical connectivity of the non-wetting phase at the end of invasion in experiments C and D.

5.3.5 Storage and Trapping Efficiency

To quantify the observations in the previous section, we plot the ratio of average final to initial saturations (trapping efficiency) as a function of flow rates (Figure 5.7a). As we discussed, the trapping efficiency is highest (100 percent) at the lowest flow rate and starts to fall as the flow rate increases. But after a certain point, the increasing displacement efficiency tips the scale and the slope changes to positive and the efficiency starts to increase.

Next, we plot the average saturations at the end of drainage and natural imbibition as a function of flow rate (Figure 5.8). As we saw in Figure 5.5 , the drainage saturation increases with increasing flow rate. In the case of trapped saturations, the same trend is seen to be preserved. Thus, even if efficiency

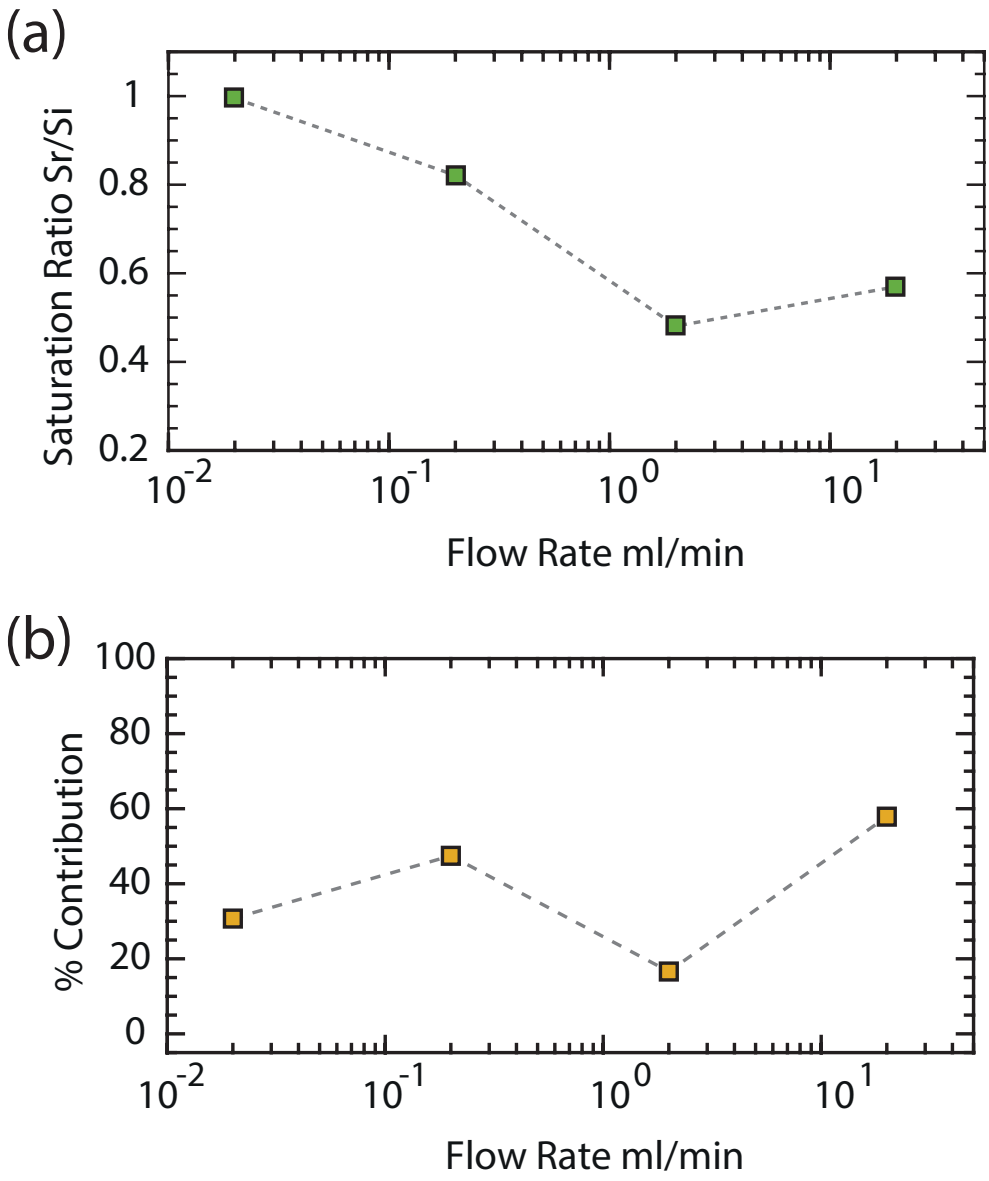

Figure 5.7: (a)Ratio of the average non-wetting phase saturations at the redistribution to that at the end of drainage (efficiency of trapping) plotted as a function of flow rate (b) Contribution of local capillary trapping (capillary heterogeneity trapping) to the overall trapping capacity (rest is residually trapped) as a function of flow rate.

Table 5.2: Slab Averaged Saturations at the End of Different Stages

Exp.	Breakthrough Sat.	Drainage Sat.	Redistribution Sat.	Sr/Si
A	0.033	0.04	0.04	0.99
B	0.071	0.06	0.049	0.82
C	0.12	0.13	0.06	0.48
D	0.26	0.33	0.19	0.56

falls, the trapped saturation increases with increasing flow rate.

To understand the impact of capillary heterogeneity, we plot the contribution of LCT (Local Capillary trapping) towards the overall trapped saturation, using a conservative maximum non-wetting phase residual saturation value (0.25) as the cut off (Figure 5.7b). The observations do not show a particular trend. At low flow rates, the contribution of LCT is lower compared to what was observed in the previous chapter for comparable grain size contrast. In experiment C, the contribution of LCT drops whereas in D, at the highest flow rate, its contribution is maximized (60%). The LCT contribution depends on the choice of our cutoff value, so that may be the reason behind this variability. But in spite of that, what these results emphasize is the persistence of the impact of heterogeneities even at flow regimes that are not capillary dominated.

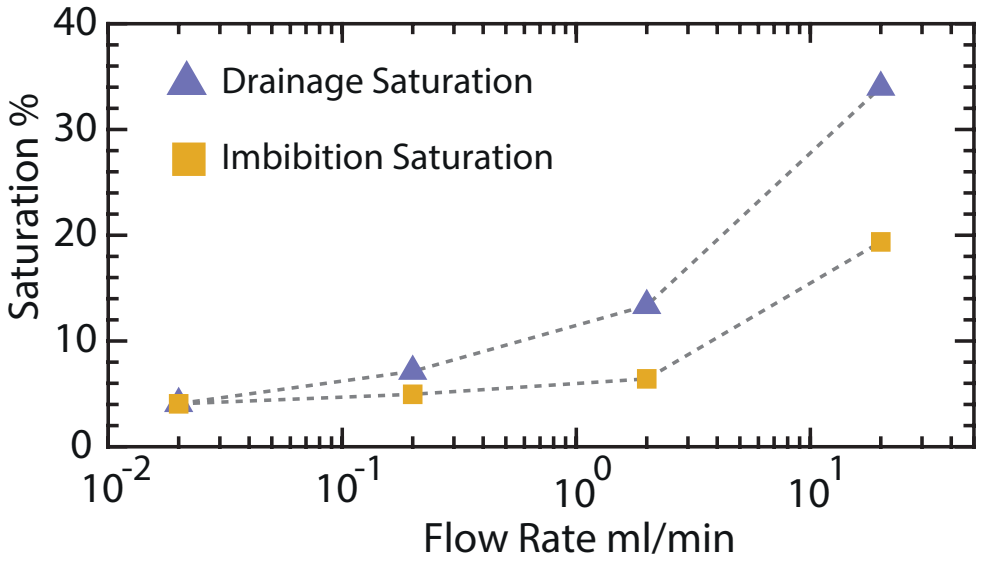

Figure 5.8: Non-wetting phase saturations at the end of (a) drainage and (b) redistribution plotted as a function of flow rate

5.4 Conclusions

In this chapter, we study the impact of flow rate on gravity unstable immiscible displacement in complex heterogeneous media. We find that the competing effects of capillary heterogenities and gravity, and viscous forces lead to a non-linear relationship between the flow rate and invasion and trapping behavior. With increasing flow rates, the sweep efficiency and non-wetting phase saturations increase as expected. At the same time, enhanced vertical connectivity and viscous dissipation lead to more non-wetting phase escaping during redistribution. But in this trade-off, the effect of flow rate comes out on top, ultimately leading to larger trapped saturations. The main takeaway from these experiments is how the underlying rock heterogeneity continues to influence displacement behavior irrespective of three orders of magnitude variation in the flow rates. At the lowest flow rate, the interplay between capillary and gravity effects, combined with the heterogeneity of the medium results in invasion behavior characterized by fragmentation, intermittency and dynamically evolving flow paths. At long timescales this can lead to higher saturations and even redirection of large scale invading phase migration pathways. As the flow rate increases, the viscous effects start to become prominent. In the crossover from capillary to viscous fingering regime, the sweep efficiency has conventionally been known to decrease (Tsuji et al., 2016, Zhang et al., 2011). However, in these experiments the stratified geometry supersedes the effects of viscous instabilities. The large scale invasion pattern at the end of drainage starts to resemble that of stable, piston like displacement and the

sweep efficiency increases with increasing flow rate. Results from these experiments can be used to describe the implications of flow regimes close to the injection wells (experiments C and D) and that in far field conditions (experiments A and B) during CO_2 sequestration. The findings presented here show that the influence of capillary heterogeneities on non-wetting phase trapping is not limited to post injection, far field conditions and that local capillary trapping can persist at viscous dominated flows close to the injection wells.

5.5 Appendix

5.5.1 Pressure Response

We plot the difference between the inlet and out pressures as a function of time until breakthrough for the four experiments (Figure 5.9). From experiment A to D, the flow rate increases, but the pressure drop across the porous medium does not increase correspondingly. Only at the highest flow rate is a conspicuous increase in the pressure drop observed. The fluctuations in pressures indicative of intermittent behavior in low capillary number experiments (experiments A and B) has been discussed previously. In the case of experiment A, as seen in section 5.3.2, the large scale pressure fluctuations follow the non-wetting phase connection and disconnection events. Such large scale fluctuations are absent in the high flow rate experiments while local (small-scale) fluctuations persist. This could be attributed to the pulsations induced by the peristaltic pump. To test this, the pressure response was recorded during displacement of the wetting phase by the invading phase in a vertical tube.

No periodic variations in the pressure was observed during such tests. Further work is needed to understand the disparity in pressure drops and fluctuations in pressure response at high flow rates.

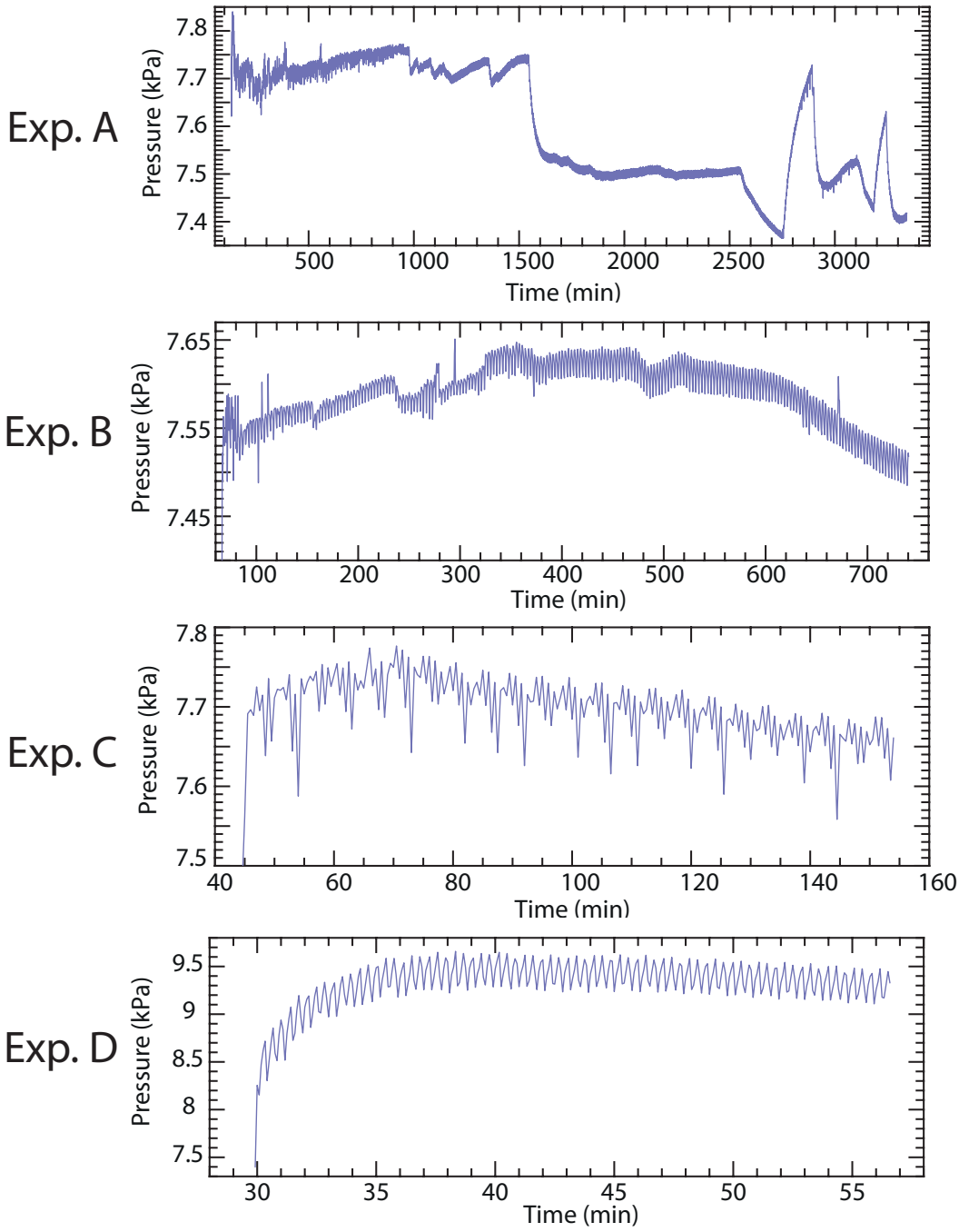

Figure 5.9: Difference between inlet and outlet pressures as a function of time until breakthrough for the four experiments

Chapter 6

Conclusion

6.1 Summary and Conclusions

In this dissertation, we studied gravity unstable immiscible displacements in complex heterogeneous porous media, experimentally and using numerical simulations, to understand and quantify the effect of small scale geologic heterogeneities on such subsurface flows in the context of CO_2 sequestration.

In our investigations, we placed emphasis on accurate representation of natural geologic heterogeneity. We chose to study flows at the intermediate scale (cm to dm); scales larger than that of rock cores so as to be able to capture the full extent of the effect of depositional features, and smaller than the reservoir scale for practical reasons. To achieve this we developed new methods to generate 3D numerical domains and 2D beadpacks that mimic natural geologic features. The automated bead/sand packing technique described in chapter 3 is one of the important contributions of this PhD.

In this study, we considered heterogeneity to be made of two components: 1) the fabric or geometry, which relates to the spatial organization of depositional features and 2) lithology, which describes the grain size variability.

The use of synthetic domains wherein the heterogeneity could be engineered helped delineate the contributions of the two components towards impacting CO_2 flow behavior.

We first numerically simulated CO_2 migration in the said 3D domains to investigate the impact of heterogeneities on CO_2 trapping capacity. Using macroscopic invasion percolation, a computationally efficient reduced physics simulation technique, we explored a large parameter space: 8 depositional architecture or fabric models populated with 40 different grain size pairings. We used Monte Carlo simulations to constrain the variability in grain size assignments. Analyzing the results model wise, we found that the invaded saturations vary with the grain size/capillary entry pressure contrast in a non-linear fashion. To describe this lithologic heterogeneity contrast we introduced a metric that accounted for the mean and standard deviations of the two constituent grain size distributions. We then fitted the saturation results to a four parameter regression model as a function of this metric. At low contrasts, the saturations were negligible. After a certain threshold contrast, the invaded saturations started to increase and then plateaued beyond another threshold. The ensemble behavior of all eight models showed that the asymptotic saturations were different for the different models. This highlighted the fact that the maximum invaded saturation was not simply dependent on the physical limits (1-residual brine saturation) but was dictated by the geometry of the system. While we were unable to come up with a combined descriptor of both the geometric and lithologic aspect of heterogeneity, we hypothesized that the

slope of the curve and maximum asymptote of fitted model was dependent on the geometry of the system.

The simulations were first conducted at the REV scale. This REV was determined by considering the volumetric ratio of the coarse to fine grained cells in the models. Comparing the simulation results at the REV (0.202 m $\times$ 0.202 m $\times$ 0.202 m) and full scale (0.99 m $\times$ 0.8 m $\times$ 0.28m) highlighted the challenges in determining a REV in such complex heterogeneous domains especially in the context of low capillary number flows. In light of this observation, millimeter scale REVs that have been previous proposed while studying CO_2 migration in heterogeneous media (Li and Benson, 2015; Jackson et al., 2020) seem inadequate. This also elucidates the need for connectivity/percolation based technique to identify the intermediate scale REV rather than intrinsic rock parameters like porosity or permeability.

To validate our numerical observations, we next conducted vertical displacement experiments in beadpacks with cross-stratified geometry generated using the above mentioned packing technique. The experiments were carried out at room temperatures and pressures using surrogate fluids that mimic the relevant physical properties (density contrast, viscosity ratio and interfacial tension) of reservoir brine and supercritical CO_2. The resulting saturations were visualized and quantified using light transmission. We were able to investigate only a single geometry, but the ensemble behavior of four experiments conducted using four different grain size contrasts displayed similar non-linear behavior like our simulations. Subtle increase in grain size and capillary en-

try pressure contrasts (50 to 350 Pa) led to drastic changes in non-wetting phase trapped saturations (0.2 to 29 %). The experiments also highlighted flow physics like fragmentation, intermittency and fluid redistribution that could not be captured by our quasi-static flow simulations. Some of this flow behavior in such complex heterogeneous media has not been visualized before at these length scales. Additionally, the height of the crossbeds dictating the asymptotic saturations post redistribution was a subtle validation of our hypothesis that it is geometry controlled.

Finally we explored the effect of flow rates on capillary trapping behavior. The results once again highlighted some of the complex flow dynamics at low capillary numbers. It was observed that at high flow rates the capillary heterogeneity of the medium subdues viscous and gravity instabilities leading to higher sweep efficiency. A major takeaway was the persistence of capillary heterogeneity trapping even at high flow rates which has repercussions when studying close to well bore flow behavior.

The results from Chapter 2 and 4 together verify the critical contribution of local capillary trapping towards overall storage capacity (upto 80% at high heterogeneity contrasts) and lay the foundations to developing predictive models that can help constrain the effect of complex natural heterogeneity on CO_2 trapping.

Overall the observations from our numerical simulations ans experiments underscore the importance of a) accounting for capillary heterogeneities when studying CO_2 plume migration and estimating storage capacities, b)

using capillary pressure and relative permeability imbibition curves that account for hysteresis to capture trapping and flow dynamics accurately and c) estimating the correct REV scales based on flow patterns rather than static parameters.

6.2 Future Directions

The novel experimental technique developed during the course of this PhD along with the necessary workflow to use light transmission for quantitative image analysis opens up a lot of research possibilities. Here we catalog a set of interesting ideas to pursue in the future.

In this dissertation we were able to experimentally test the predictive model developed in Chapter 1 only with a single geometry. So a natural extension of this work would be to run similar set of experiments in other geometries. One such example was shown in Chapter 4, section 4.4.2. The results from these experiments could help us better understand if and how the fabric geometry affects the maximum asymptotic saturations.

The experimental results conducted here demonstrate the effect of grain size contrast on trapped saturations. Invasion Percolation simulations tell us that as long as the contrast remains the same, the trapping and flow behavior remains unchanged, and that the absolute values of the grain sizes do not make a difference. However we believe that the change in permeability with grain size and hence the Bond number will affect the flow. The most obvious effect will be the change in migration times as the matrix permeability changes. It

will be interesting to test how this affects the trapping capacity. Keeping the grain sizes used constant, a change in the Bond number can also be brought about by using different fluid pairs. Comparing the two methods can help us delineate the effect of gravity and permeability.

The variable flow rate experiments were conducted for a single geometry and grain size contrast. It would be worthwhile to explore a wider parameter space. Varying the heterogeneity contrast, capillary number and Bond number, a phase diagram like the one proposed by Ewing and Berkowitz (1998) could be generated. It would be intriguing to see if large scale flow behavior in heterogeneous media can be demarcated based on the flow regimes as demonstrated by Lenormand et al. (1988) for pore scale flows in homogeneous porous media.

The wettability of the porous medium has gathered a lot of attention in the past decade in the context of CO_2 relative permeability and capillary trapping potential (Chaudhary et al., 2013; Al-Menhali et al., 2015; Al-Khdheeawi et al. 2018). Considering the observations from our experiments, probing the effect of wettability on invasion dynamics and trapped saturations is an interesting future research direction. By using beads of different materials and surface properties the contact angle between the grains and fluids can be changed. The experimental technique developed here provides a unique opportunity to selectively engineer the surface properties of different portions of the porous medium.

We used a point source in our experiments which may not be always the

case in the subsurface. Instead if a line source were used, the invasion profile may be different depending on the geometry and heterogeneity contrast of the system. In high contrast cases, since the connectivity of the invading phase is not always established between the the different bedform layers, a line source may not ultimately result in a different flow profile. But in a low contrast system, numerous gravity fingers may develop over time leading to larger saturations. Thus it would be worthwhile to conduct experiments on these lines to verify our hypothesis.

The experiments in this work intended to mimic the post injection migration of CO_2. However, since the experiments were conducted at constant flow rate conditions, we cannot claim that the flow is completely buoyancy driven, as it would likely be in the subsurface. It would be worthwhile to re-do these experiments at constant pressure conditions like Trevisan et al. (2015,2017).

Another question that is worth pursuing is the effect of intermittent injection either in the form of periodic bursts of non-wetting phase or a chase brine scenario as proposed by water alternating gas studies (Spiteri and Juanes, 2006). In either case, once the injection is stopped and non-wetting phase vertical connectivity is disrupted, it would be interesting to see if the existing pathways get rejuvenated or new pathways form. Especially in the low to mid contrast cases, this technique could possibly lead to a larger non-wetting phase footprint which ultimately increases the likelihood of trapping.

A shortcoming of these experiments is that the petrophysical properties

of the glass beads used were not characterized. This prevents the experimental results obtained here from being used for validating and calibrating pore and continuum scale flow models, so as to improve their ability to capture the rich hysteresis and trapping behavior. Going forward, using the more widely used Unimin Accusands that have been extensively characterized previously, can help further the use of this experimental dataset.

Bibliography

[1] Morteza Akbarabadi and Mohammad Piri. Relative permeability hysteresis and capillary trapping characteristics of supercritical co_2/brine systems: An experimental study at reservoir conditions. *Advances in Water Resources*, 52:190–206, 2013.

[2] Emad A Al-Khdheeawi, Stephanie Vialle, Ahmed Barifcani, Mohammad Sarmadivaleh, and Stefan Iglauer. Effect of wettability heterogeneity and reservoir temperature on co_2 storage efficiency in deep saline aquifers. *International Journal of Greenhouse Gas Control*, 68:216–229, 2018.

[3] Ali Al-Menhali, Ben Niu, and Samuel Krevor. Capillarity and wetting of carbon dioxide and brine during drainage in b erea sandstone at reservoir conditions. *Water Resources Research*, 51(10):7895–7914, 2015.

[4] John R.L. Allen, editor. *Sedimentary Structures Their Character and Physical Basis Volume I.* Elsevier, 1982.

[5] John R.L. Allen, editor. *Sedimentary Structures Their Character and Physical Basis Volume II.* Elsevier, 1982.

[6] Yusuf B Altundas, TS Ramakrishnan, Nikita Chugunov, Romain de Louebens, et al. Retardation of co_2 caused by capillary pressure hysteresis: A new

co_2 trapping mechanism. *Spe Journal*, 16(04):784–794, 2011.

[7] J Cavanagh Andrew, R Stuart Haszeldine, and Bamshad Nazarian. The sleipner co_2 storage site: using a basin model to understand reservoir simulations of plume dynamics. *First Break*, 33(6):61–68, 2015.

[8] Stefan Bachu, WD Gunter, and EH Perkins. Aquifer disposal of co_2: hydrodynamic and mineral trapping. *Energy conversion and management*, 35(4):269–279, 1994.

[9] Sahar Bakhshian, Seyyed A Hosseini, and Nima Shokri. Pore-scale characteristics of multiphase flow in heterogeneous porous media using the lattice boltzmann method. *Scientific reports*, 9(1):1–13, 2019.

[10] Uditha C Bandara, Alexandre M Tartakovsky, and Bruce J Palmer. Pore-scale study of capillary trapping mechanism during co_2 injection in geological formations. *International Journal of Greenhouse Gas Control*, 5(6):1566–1577, 2011.

[11] John Baxter, Ugur Tuzun, David Heyes, Igan Hayati, and Per Fredlund. Stratification in poured granular heaps. *Nature*, 391(6663):136–136, 1998.

[12] Jacob Bear. *Dynamics of fluids in porous media*. Courier Corporation, 2013.

[13] Niels Bech and Peter Frykman. Trapping of buoyancy-driven co_2 during imbibition. *International Journal of Greenhouse Gas Control*, 78:48–61, 2018.

[14] Hamid Behzadi and Vladimir Alvarado. Upscaling of upward co_2 migration in 2d system. *Advances in water resources*, 46:46–54, 2012.

[15] Sally Benson. Underground geological storage. *IPCC Special Repot on Carbon Capture and Storage*, pages 195–276, 2005.

[16] Sally M Benson and David R Cole. Co_2 sequestration in deep sedimentary formations. *Elements*, 4(5):325–331, 2008.

[17] Perry D Bergman and Edward M Winter. Disposal of carbon dioxide in aquifers in the us. *Energy Conversion and Management*, 36(6-9):523–526, 1995.

[18] Soumyajyoti Biswas, Paolo Fantinel, Oshri Borgman, Ran Holtzman, and Lucas Goehring. Drying and percolation in correlated porous media. *Physical Review Fluids*, 3(12):124307, 2018.

[19] Mustafa M. Bob, Michael C. Brooks, Susan C. Mravik, and A. Lynn Wood. A modified light transmission visualization method for DNAPL saturation measurements in 2-D models. *Advances in Water Resources*, 31(5):727–742, 2008.

[20] Oshri Borgman, Paolo Fantinel, Wieland Luhder, Lucas Goehring, and Ran Holtzman. Impact of spatially correlated pore-scale heterogeneity

on drying porous media. *Water Resources Research*, 53(7):5645–5658, 2017.

[21] Steven Lawrence Bryant, Srivatsan Lakshminarasimhan, Gary Arnold Pope, et al. Buoyancy-dominated multiphase flow and its impact on geological sequestration of co_2. In *SPE/DOE Symposium on Improved Oil Recovery*. Society of Petroleum Engineers, 2006.

[22] Dan Carruthers and Philip Ringrose. Secondary oil migration: oil-rock contact volumes, flow behaviour and rates. *Geological Society, London, Special Publications*, 144(1):205–220, 1998.

[23] Dan Carruthers and Philip Ringrose. Secondary oil migration: oil-rock contact volumes, flow behaviour and rates. *Geological Society, London, Special Publications*, 144(1):205–220, 1998.

[24] Daniel J Carruthers. Modeling of secondary petroleum migration using invasion percolation techniques. *Multidimensional basin modeling: AAPG/Datapages Discovery Series*, 7:21–37, 2003.

[25] Daniel JF Carruthers. *Transport modelling of secondary oil migration using gradient-driven invasion percolation techniques*. PhD thesis, Heriot-Watt University, 1998.

[26] Andrew Cavanagh and Bamshad Nazarian. A new and extended sleipner benchmark model for co_2 storage simulations in the utsira formation. *Energy Procedia*, 63:2831–2835, 2014.

[27] Andrew J Cavanagh and R Stuart Haszeldine. The sleipner storage site: Capillary flow modeling of a layered co_2 plume requires fractured shale barriers within the utsira formation. *International Journal of Greenhouse Gas Control*, 21:101–112, 2014.

[28] Andy Chadwick, Gareth Williams, Nicolas Delepine, Vincent Clochard, Karine Labat, Susan Sturton, Maike-L Buddensiek, Menno Dillen, Michael Nickel, Anne Louise Lima, et al. Quantitative analysis of time-lapse seismic monitoring data at the sleipner co_2 storage operation. *The Leading Edge*, 29(2):170–177, 2010.

[29] Kuldeep Chaudhary, M Bayani Cardenas, William W Wolfe, Jessica A Maisano, Richard A Ketcham, and Philip C Bennett. Pore-scale trapping of supercritical co_2 and the role of grain wettability and shape. *Geophysical Research Letters*, 40(15):3878–3882, 2013.

[30] Yi-Feng Chen, Shu Fang, Dong-Sheng Wu, and Ran Hu. Visualizing and quantifying the crossover from capillary fingering to viscous fingering in a rough fracture. *Water Resources Research*, 53(9):7756–7772, 2017.

[31] Pierre Chiquet, Jean-Luc Daridon, Daniel Broseta, and Sylvain Thibeau. Co_2/water interfacial tensions under pressure and temperature conditions of co_2 geological storage. *Energy Conversion and Management*, 48(3):736–744, 2007.

[32] Yildiray Cinar, Amir Riaz, Hamdi A Tchelepi, et al. Experimental

study of co_2 injection into saline formations. In *SPE Annual Technical Conference and Exhibition*. Society of Petroleum Engineers, 2007.

[33] Stephen H Conrad, Robert J Glass, and William J Peplinski. Bench-scale visualization of DNAPL remediation processes in analog heterogeneous aquifers: surfactant floods and in situ oxidation using permanganate. *Journal of Contaminant Hydrology*, 58(1-2):13–49, 2002.

[34] P.W.M. Corbett, P.S. Ringrose, J.L. Jensen, and K.S. Sorbie. Laminated Clastic Reservoirs: The Interplay of Capillary Pressure and Sedimentary Architecture. In *SPE Annual Technical Conference and Exhibition*. Society of Petroleum Engineers, 1992.

[35] Dennis L Cox, Sandra J Lindquist, Connie L Bargas, Karen G Havholm, and R Mohan Srivastava. Integrated modeling for optimum management of a giant gas condensate reservoir, jurassic eolian nugget sandstone, anschutz ranch east field, utah overthrust (usa). 1994.

[36] R. A. Dawe, M. R. Wheat, and M. S. Bidner. Experimental investigation of capillary pressure effects on immiscible displacement in lensed and layered porous media. *Transport in Porous Media*, 7(1):83–101, 1992.

[37] Richard A. Dawe, Albert Caruana, and Carlos A. Grattoni. Immiscible Displacement in Cross-Bedded Heterogeneous Porous Media. *Transport in Porous Media*, 87(1):335–353, 2011.

[38] Helen E. Dawson and Paul V. Roberts. Influence of Viscous, Gravitational, and Capillary Forces on DNAPL Saturation. *Ground Water*, 35(2):261–269, 1997.

[39] Harry Dembicki Jr and Michael J Anderson. Secondary migration of oil: experiments supporting efficient movement of separate, buoyant oil phase along limited conduits. *AAPG Bulletin*, 73(8):1018–1021, 1989.

[40] Hailin Deng, Philip H Stauffer, Zhenxue Dai, Zunsheng Jiao, and Ronald C Surdam. Simulation of industrial-scale co_2 storage: Multi-scale heterogeneity and its impacts on storage capacity, injectivity and leakage. *International Journal of Greenhouse Gas Control*, 10:397–418, 2012.

[41] Christine Doughty and Karsten Pruess. Modeling supercritical carbon dioxide injection in heterogeneous porous media. *Vadose Zone Journal*, 3(3):837–847, 2004.

[42] WA England, AS Mackenzie, DM Mann, and TM Quigley. The movement and entrapment of petroleum fluids in the subsurface. *Journal of the Geological Society*, 144(2):327–347, 1987.

[43] Jonathan P Ennis-King and Lincoln Paterson. Role of convective mixing in the long-term storage of carbon dioxide in deep saline formations. *Spe Journal*, 10(03):349–356, 2005.

[44] Robert P Ewing and Brian Berkowitz. A generalized growth model for simulating initial migration of dense non-aqueous phase liquids. *Water*

Resources Research, 34(4):611–622, 1998.

[45] M Ferer, Grant S Bromhal, and Duane H Smith. Two-phase flow in porous media: Crossover from capillary fingering to compact invasion for drainage. *Physical Review E*, 71(2):026303, 2005.

[46] Matthew Flett, Randal Gurton, and Geoff Weir. Heterogeneous saline formations for carbon dioxide disposal: Impact of varying heterogeneity on containment and trapping. *Journal of Petroleum Science and Engineering*, 57(1-2):106–118, 2007.

[47] Robert L Folk. A review of grain-size parameters. *Sedimentology*, 6(2):73–93, 1966.

[48] Robert Louis Folk and William C Ward. Brazos river bar [texas]; a study in the significance of grain size parameters. *Journal of Sedimentary Research*, 27(1):3–26, 1957.

[49] Alejandro F. Frangi, Wiro J. Niessen, Koen L. Vincken, and Max A. Viergever. Multiscale vessel enhancement filtering. pages 130–137. Springer, Berlin, Heidelberg, 1998.

[50] Vidar Frette, Jens Feder, Torstein Jossang, and Paul Meakin. Buoyancy-driven fluid migration in porous media. *Physical review letters*, 68(21):3164, 1992.

[51] Liv Furuberg, Knut Jorgen Maaloy, and Jens Feder. Intermittent behavior in slow drainage. *Physical Review E*, 53(1):966, 1996.

[52] Sarah E Gasda, Halvor M Nilsen, and Helge K Dahle. Impact of structural heterogeneity on upscaled models for large-scale co_2 migration and trapping in saline aquifers. *Advances in water resources*, 62:520–532, 2013.

[53] Helmut Geistlinger, Gunnar Krauss, Detlef Lazik, and Ludwig Luckner. Direct gas injection into saturated glass beads: Transition from incoherent to coherent gas flow pattern. *Water resources research*, 42(7), 2006.

[54] Naum I. Gershenzon, Robert W. Ritzi, David F. Dominic, Edward Mehnert, and Roland T. Okwen. Capillary trapping of CO_2 in heterogeneous reservoirs during the injection period. *International Journal of Greenhouse Gas Control*, 59:13–23, 2017.

[55] Naum I Gershenzon, Robert W Ritzi Jr, David F Dominic, Edward Mehnert, and Roland T Okwen. Capillary trapping of co_2 in heterogeneous reservoirs during the injection period. *International Journal of greenhouse gas control*, 59:13–23, 2017.

[56] R. J. Glass, S. H. Conrad, and W. Peplinski. Gravity-destabilized nonwetting phase invasion in macroheterogeneous porous media: Experimental observations of invasion dynamics and scale analysis. *Water Resources Research*, 36(11):3121–3137, 2000.

[57] R. J. Glass and M. J. Nicholl. Physics of gravity fingering of immiscible

fluids within porous media: An overview of current understanding and selected complicating factors. *Geoderma*, 70(2-4):133–163, 1996.

[58] Robert J Glass and Lane Yarrington. Mechanistic modeling of fingering, nonmonotonicity, fragmentation, and pulsation within gravity/buoyant destabilized two-phase/unsaturated flow. *Water Resources Research*, 39(3), 2003.

[59] Charles D Gorecki, Scott C Ayash, Guoxiang Liu, Jason R Braunberger, and Neil W Dotzenrod. A comparison of volumetric and dynamic co_2 storage resource and efficiency in deep saline formations. *International Journal of Greenhouse Gas Control*, 42:213–225, 2015.

[60] Christopher P Green and Jonathan Ennis-King. Effect of vertical heterogeneity on long-term migration of co_2 in saline formations. *Transport in porous media*, 82(1):31–47, 2010.

[61] Christopher P Green and Jonathan Ennis-King. Residual trapping beneath impermeable barriers during buoyant migration of co_2. *Transport in porous media*, 98(3):505–524, 2013.

[62] B. Clark Griffith, Robert M. Holt, and Robert J. Glass. Generating Reproducible Microscale Heterogeneity for Transmitted-Light Flow Visualization Experiments. *Vadose Zone Journal*, 12(4):0, 2013.

[63] C.A. Hartkamp-Bakker. Capillary Oil Entrapment in Crossbedded Sedimentary Structures of Fluvial Sandstone Reservoirs. In *SPE Annual*

Technical Conference and Exhibition. Society of Petroleum Engineers, 1991.

[64] Christian Hermanrud, Gunn Mari Grimsmo Teige, Martin Iding, Ola Eiken, Lars Rennan, and Svend Ostmo. Differences between flow of injected co_2 and hydrocarbon migration. In *Geological Society, London, Petroleum Geology Conference series*, volume 7, pages 1183–1188. Geological Society of London, 2010.

[65] Anna L Herring, Linnea Andersson, Steffen Schluter, Adrian Sheppard, and Dorthe Wildenschild. Efficiently engineering pore-scale processes: The role of force dominance and topology during nonwetting phase trapping in porous media. *Advances in Water Resources*, 79:91–102, 2015.

[66] Anna L Herring, Elizabeth J Harper, Linnea Andersson, Adrian Sheppard, Brian K Bay, and Dorthe Wildenschild. Effect of fluid topology on residual nonwetting phase trapping: Implications for geologic co_2 sequestration. *Advances in Water Resources*, 62:47–58, 2013.

[67] Mark H Holtz. Residual gas saturation to aquifer influx: A calculation method for 3-d computer reservoir model construction. In *SPE Gas Technology Symposium*. Society of Petroleum Engineers, 2002.

[68] Ran Holtzman and Ruben Juanes. Crossover from fingering to fracturing in deformable disordered media. *Physical Review E*, 82(4):046305, 2010.

[69] Susan D Hovorka, Sally M Benson, Christine Doughty, Barry M Freifeld, Shinichi Sakurai, Thomas M Daley, Yousif K Kharaka, Mark H Holtz, Robert C Trautz, H Seay Nance, et al. Measuring permanence of co_2 storage in saline formations: the frio experiment. *Environmental Geosciences*, 13(2):105–121, 2006.

[70] Y. Huang, P.S. Ringrose, and K.S. Sorbie. X-Ray Imaging of Waterflood Fluid Saturations in Heterogeneous Rock Slabs. In *International Meeting on Petroleum Engineering*. Society of Petroleum Engineers, 1995.

[71] Y. Huang, P.S. Ringrose, and K.S. Sorbie. The Effects of Heterogeneity and Wettability on Oil Recovery from Laminated Sedimentary Structures. *SPE Journal*, 1(04):451–462, 1996.

[72] Yaduo Huang, P.S. Ringrose, and K.S. Sorbie. Waterflood Displacement Mechanisms in a Laminated Rock Slab: Validation of Predicted Capillary Trapping Mechanisms. *SPE Reservoir Engineering*, 10(04):287–292, 1995.

[73] S Taku Ide, Kristian Jessen, and Franklin M Orr Jr. Storage of co_2 in saline aquifers: Effects of gravity, viscous, and capillary forces on amount and timing of trapping. *International Journal of Greenhouse Gas Control*, 1(4):481–491, 2007.

[74] Tissa H Illangasekare, James L Ramsey, Karsten H Jensen, and Michael B Butts. Experimental study of movement and distribution of dense or-

ganic contaminants in heterogeneous aquifers. *Journal of Contaminant Hydrology*, 20(1-2):1–25, 1995.

[75] Marios A Ioannidis, Ioannis Chatzis, and Francis AL Dullien. Macroscopic percolation model of immiscible displacement: Effects of buoyancy and spatial structure. *Water Resources Research*, 32(11):3297–3310, 1996.

[76] AW Islam, Timothy A Meckel, AY Sun, and PG Krishnamurthy. Numerical experiments of density driven co_2 saturated brine migration in heterogeneous two-dimensional geologic fabric materials. *International Communications in Heat and Mass Transfer*, 71:148–156, 2016.

[77] Samuel Jackson, Qingyang Lin, and Sam Krevor. Representative elementary volumes, hysteresis and heterogeneity in multiphase flow from the pore to continuum scale. *EarthArXiv*, 2019.

[78] Samuel J. Jackson, Simeon Agada, Catriona A. Reynolds, and Samuel Krevor. Characterizing Drainage Multiphase Flow in Heterogeneous Sandstones. *Water Resources Research*, 54(4):3139–3161, 2018.

[79] Wei Ji, Amine Dahmani, David P. Ahlfeld, Jia Ding Lin, and Edward Hill. Laboratory Study of Air Sparging: Air Flow Visualization. *Groundwater Monitoring & Remediation*, 13(4):115–126, 1993.

[80] Alan V. Jopling. Laboratory study of sorting processes related to flow separation. *Journal of Geophysical Research*, 69(16):3403–3418, 1964.

[81] Ruben Juanes, Christopher W MacMinn, and Michael L Szulczewski. The footprint of the co_2 plume during carbon dioxide storage in saline aquifers: storage efficiency for capillary trapping at the basin scale. *Transport in porous media*, 82(1):19–30, 2010.

[82] Ruben Juanes, EJ Spiteri, FM Orr Jr, and MJ Blunt. Impact of relative permeability hysteresis on geological co_2 storage. *Water resources research*, 42(12), 2006.

[83] Elizabeth Harper Kimbrel, Anna L Herring, Ryan T Armstrong, Ivan Lunati, Brian K Bay, and Dorthe Wildenschild. Experimental characterization of nonwetting phase trapping and implications for geologic co_2 sequestration. *International Journal of Greenhouse Gas Control*, 42:1–15, 2015.

[84] Dagrun Kjonsvik, James Doyle, Torgrim Jacobsen, Alistair Jones, et al. The effects of sedimentary heterogeneities on production from a shallow marine reservoir-what really matters? In *SPE Annual Technical Conference and Exhibition*. Society of Petroleum Engineers, 1994.

[85] M. G. Kleinhans. Sorting in grain flows at the lee side of dunes. *Earth-Science Reviews*, 65(1-2):75–102, 2004.

[86] Katherine A. Klise, Vincent C. Tidwell, and Sean A. McKenna. Comparison of laboratory-scale solute transport visualization experiments with numerical simulation using cross-bedded sandstone. *Advances in Water Resources*, 31(12):1731–1741, 2008.

[87] J. P. Koeppe, M. Enz, and J. Kakalios. Phase diagram for avalanche stratification of granular media. *Physical Review E*, 58(4):R4104–R4107, 1998.

[88] Christine E Koltermann and Steven M Gorelick. Heterogeneity in sedimentary deposits: A review of structure-imitating, process-imitating, and descriptive approaches. *Water Resources Research*, 32(9):2617–2658, 1996.

[89] T.F.M. Kortekaas. Water/Oil Displacement Characteristics in Crossbedded Reservoir Zones. *Society of Petroleum Engineers Journal*, 25(06):917–926, 1985.

[90] Michael Krause, Sam Krevor, and Sally M Benson. A procedure for the accurate determination of sub-core scale permeability distributions with error quantification. *Transport in porous media*, 98(3):565–588, 2013.

[91] Samuel Krevor, Martin J. Blunt, Sally M. Benson, Christopher H. Pentland, Catriona Reynolds, Ali Al-Menhali, and Ben Niu. Capillary trapping for geologic carbon dioxide storage – From pore scale physics to field scale implications. *International Journal of Greenhouse Gas Control*, 40:221–237, 2015.

[92] Samuel Krevor, Martin J Blunt, Sally M Benson, Christopher H Pentland, Catriona Reynolds, Ali Al-Menhali, and Ben Niu. Capillary trapping for geologic carbon dioxide storage–from pore scale physics to field

scale implications. *International Journal of Greenhouse Gas Control*, 40:221–237, 2015.

[93] Samuel C. M. Krevor, Ronny Pini, Boxiao Li, and Sally M. Benson. Capillary heterogeneity trapping of CO_2 in a sandstone rock at reservoir conditions. *Geophysical Research Letters*, 38(15), 2011.

[94] Samuel C. M. Krevor, Ronny Pini, Lin Zuo, and Sally M. Benson. Relative permeability and trapping of CO_2 and water in sandstone rocks at reservoir conditions. *Water Resources Research*, 48(2), 2012.

[95] Samuel CM Krevor, Ronny Pini, Lin Zuo, and Sally M Benson. Relative permeability and trapping of co_2 and water in sandstone rocks at reservoir conditions. *Water resources research*, 48(2), 2012.

[96] Prasanna G Krishnamurthy, Tip A Meckel, and David DiCarlo. Mimicking geologic depositional fabrics for multiphase flow experiments. *Water Resources Research*, 55(11):9623–9638, 2019.

[97] Prasanna G. Krishnamurthy, Siddharth Senthilnathan, Hongkyu Yoon, Daan Thomassen, Tip Meckel, and David DiCarlo. Comparison of Darcy's law and invasion percolation simulations with buoyancy-driven CO_2-brine multiphase flow in a heterogeneous sandstone core. *Journal of Petroleum Science and Engineering*, 155:54–62, 2017.

[98] Prasanna Ganesan Krishnamurthy, Luca Trevisan, and Tip Meckel. Understanding the effects small scale heterogeneity on buoyancy driven co_2

migration for capillary trapped storage capacity estimation. *Energy Procedia*, 114:4954–4960, 2017a.

[99] Prasanna Ganesan Krishnamurthy, Luca Trevisan, and Tip Meckel. Investigating the influence of geological heterogeneity on capillary trapping of buoyant co_2 using transmitted-light flow visualization experiments. *Energy Procedia*, 114:4961–4966, 2017b.

[100] Bernard H. Kueper, Wesley Abbott, and Graham Farquhar. Experimental observations of multiphase flow in heterogeneous porous media. *Journal of Contaminant Hydrology*, 5(1):83–95, 1989.

[101] Bernard H Kueper and David B McWhorter. The use of macroscopic percolation theory to construct large-scale capillary pressure curves. *Water resources research*, 28(9):2425–2436, 1992.

[102] Chia-Wei Kuo, Jean-Christophe Perrin, and Sally M Benson. Simulation studies of effect of flow rate and small scale heterogeneity on multiphase flow of co_2 and brine. *Energy Procedia*, 4:4516–4523, 2011.

[103] I. Lebron and D. A. Robinson. Particle Size Segregation during Hand Packing of Coarse Granular Materials and Impacts on Local Pore-Scale Structure. *Vadose Zone Journal*, 2(3):330–337, 2003.

[104] U Lengler, M De Lucia, and M Kuhn. The impact of heterogeneity on the distribution of co_2: Numerical simulation of co_2 storage at ketzin. *International Journal of Greenhouse Gas Control*, 4(6):1016–1025, 2010.

[105] Roland Lenormand, Eric Touboul, and Cesar Zarcone. Numerical models and experiments on immiscible displacements in porous media. *Journal of fluid mechanics*, 189:165–187, 1988.

[106] Roland Lenormand, Cesar Zarcone, and A Sarr. Mechanisms of the displacement of one fluid by another in a network of capillary ducts. *Journal of Fluid Mechanics*, 135:337–353, 1983.

[107] Boxiao Li and Sally M. Benson. Influence of small-scale heterogeneity on upward CO_2 plume migration in storage aquifers. *Advances in Water Resources*, 83:389–404, 2015.

[108] Catalan Lionel, Fu Xiaowen, Chatzis Ioannis, and Francis AL Dullien. An experimental study of secondary oil migration. *AAPG bulletin*, 76(5):638–650, 1992.

[109] Xiaorong Luo, Caizhi Hu, Zhongyao Xiao, Jian Zhao, Baoshou Zhang, Wan Yang, Hong Zhao, Fengyun Zhao, Yuhong Lei, and Likuan Zhang. Effects of carrier bed heterogeneity on hydrocarbon migration. *Marine and Petroleum Geology*, 68:120–131, 2015.

[110] Jingsheng Ma, Gary D Couples, and Andy R Gardiner. Numerical modeling of the fluid flow impact of thin baffle laminae in cross bedding. *Water Resources Research*, 44(4), 2008.

[111] Knut Jorgen Maaloy, Liv Furuberg, Jens Feder, and Torstein Jossang. Dynamics of slow drainage in porous media. *Physical review letters*,

68(14):2161, 1992.

[112] Hernán A. Makse. Stratification instability in granular flows. *Physical Review E*, 56(6):7008–7016, 1997a.

[113] Hernán A. Makse, Robin C. Ball, H. Eugene Stanley, and Stephen Warr. Dynamics of granular stratification. *Physical Review E - Statistical Physics, Plasmas, Fluids, and Related Interdisciplinary Topics*, 58(3):3357–3367, 1998.

[114] Hernán A. Makse, Pierre Cizeau, and H. Eugene Stanley. Possible Stratification Mechanism in Granular Mixtures. *Physical Review Letters*, 78(17):3298–3301, 1997b.

[115] Hernán A. Makse, Shlomo Havlin, Plamen Ch. Ivanov, Peter R. King, Sona Prakash, and H. Eugene Stanley. Pattern formation in sedimentary rocks: Connectivity, permeability, and spatial correlations. *Physica A: Statistical Mechanics and its Applications*, 233(3-4):587–605, 1996.

[116] Hernán A. Makse, Shlomo Havlin, Peter R. King, and H. Eugene Stanley. Spontaneous stratification in granular mixtures. *Nature*, 386(6623):379–382, 1997c.

[117] Paul Meakin, Jens Feder, Vidar Frette, Torstein Jo, et al. Invasion percolation in a destabilizing gradient. *Physical Review A*, 46(6):3357, 1992.

[118] Paul Meakin, Geri Wagner, Anne Vedvik, Haakon Amundsen, Jens Feder, and Torstein Jossang. Invasion percolation and secondary migration: experiments and simulations. *Marine and Petroleum Geology*, 17(7):777–795, 2000.

[119] T. A. Meckel, L. Trevisan, and P. G. Krishnamurthy. A method to generate small-scale, high-resolution sedimentary bedform architecture models representing realistic geologic facies. *Scientific Reports*, 7(1):9238, 2017.

[120] Timothy A Meckel. Digital rendering of sedimentary-relief peels: implications for clastic facies characterization and fluid flow. *Journal of Sedimentary Research*, 83(6):495–501, 2013.

[121] Timothy A Meckel and Steven L Bryant. Buoyancy-driven flow in heterogeneous materials. *Energy Procedia*, 63:5495–5502, 2014.

[122] Timothy A Meckel, Steven L Bryant, and P Ravi Ganesh. Characterization and prediction of co_2 saturation resulting from modeling buoyant fluid migration in 2d heterogeneous geologic fabrics. *International Journal of greenhouse gas control*, 34:85–96, 2015.

[123] D Mikes and J Bruining. Standard flow cells to incorporate small-scale heterogeneity (crossbedding) in a reservoir model. *Marine and petroleum geology*, 23(9-10):979–993, 2006.

[124] Franziska Moebius and Dani Or. Pore scale dynamics underlying the motion of drainage fronts in porous media. *Water Resources Research*, 50(11):8441–8457, 2014.

[125] Norman R Morrow. *Interfacial phenomena in petroleum recovery*. CRC Press, 1990.

[126] Mushlih Muharrik, Tetsuya Suekane, and Anindityo Patmonoaji. Effect of buoyancy on fingering growth activity in immiscible two-phase flow displacements. *Journal of Fluid Science and Technology*, 13(1):JFST0006–JFST0006, 2018.

[127] Kevin G Mumford, Sarah E Dickson, and James E Smith. Slow gas expansion in saturated natural porous media by gas injection and partitioning with non-aqueous phase liquids. *Advances in water resources*, 32(1):29–40, 2009.

[128] W. F. Murphy, J. N. Roberts, D. Yale, and K. W. Winkler. Centimeter scale heterogeneities and microstratifaction in sedimentary rocks. *Geophysical Research Letters*, 11(8):697–700, 1984.

[129] Hailun Ni, Maartje Boon, Charlotte Garing, and Sally M Benson. Predicting co_2 residual trapping ability based on experimental petrophysical properties for different sandstone types. *International Journal of Greenhouse Gas Control*, 86:158–176, 2019.

[130] Kjetil Nordahl and Philip S Ringrose. Identifying the representative elementary volume for permeability in heterolithic deposits using numerical rock models. *Mathematical geosciences*, 40(7):753, 2008.

[131] Kjetil Nordahl, Philip S Ringrose, and Renjun Wen. Petrophysical characterization of a heterolithic tidal reservoir interval using a process-based modelling tool. *Petroleum Geoscience*, 11(1):17–28, 2005.

[132] Jan Martin Nordbotten, Michael A. Celia, and Stefan Bachu. Injection and Storage of CO_2 in Deep Saline Aquifers: Analytical Solution for CO_2 Plume Evolution During Injection. *Transport in Porous Media*, 58(3):339–360, 2005.

[133] Junho Oh, Kue-Young Kim, Weon Shik Han, Eungyu Park, and Jeong-Chan Kim. Migration behavior of supercritical and liquid co_2 in a stratified system: Experiments and numerical simulations. *Water Resources Research*, 51(10):7937–7958, 2015.

[134] Franklin M Orr. Onshore geologic storage of co_2. *Science*, 325(5948):1656–1658, 2009.

[135] Christopher H Pentland, Rehab El-Maghraby, Stefan Iglauer, and Martin J Blunt. Measurements of the capillary trapping of super-critical carbon dioxide in berea sandstone. *Geophysical Research Letters*, 38(6), 2011.

[136] Jean-Christophe Perrin and Sally Benson. An experimental study on the influence of sub-core scale heterogeneities on co_2 distribution in reservoir rocks. *Transport in porous media*, 82(1):93–109, 2010.

[137] Glen Peters and Ida Sognnaes. The role of carbon capture and storage in the mitigation of climate change. *CICERO Report*, 2019.

[138] Gillian E Pickup and Caroline Y Hern. The development of appropriate upscaling procedures. *Transport in porous media*, 46(2-3):119–138, 2002.

[139] Ronny Pini and Sally M. Benson. Characterization and scaling of mesoscale heterogeneities in sandstones. *Geophysical Research Letters*, 40(15):3903–3908, 2013.

[140] Ronny Pini and Sally M Benson. Characterization and scaling of mesoscale heterogeneities in sandstones. *Geophysical Research Letters*, 40(15):3903–3908, 2013.

[141] Ronny Pini, Samuel CM Krevor, and Sally M Benson. Capillary pressure and heterogeneity for the co_2/water system in sandstone rocks at reservoir conditions. *Advances in Water Resources*, 38:48–59, 2012.

[142] Szczepan Polak, Yildiray Cinar, Torleif Holt, and Ole Torsaeter. An experimental investigation of the balance between capillary, viscous, and gravitational forces during co_2 injection into saline aquifers. *Energy Procedia*, 4:4395–4402, 2011.

[143] Szczepan Polak, Yildiray Cinar, Torleif Holt, and Ole Torsaeter. Use of low-and high-ift fluid systems in experimental and numerical modelling of systems that mimic co_2 storage in deep saline formations. *Journal of Petroleum Science and Engineering*, 129:97–109, 2015.

[144] Bauyrzhan K Primkulov, Amir A Pahlavan, Xiaojing Fu, Benzhong Zhao, Christopher W MacMinn, and Ruben Juanes. Signatures of fluid–fluid displacement in porous media: wettability, patterns and pressures. *Journal of Fluid Mechanics*, 875, 2019.

[145] Avinoam Rabinovich, Kasama Itthisawatpan, and Louis J Durlofsky. Upscaling of co_2 injection into brine with capillary heterogeneity effects. *Journal of Petroleum Science and Engineering*, 134:60–75, 2015.

[146] Birger Rasmussen. Fluorescent growth bands in irradiated-bitumen nodules: Evidence of episodic hydrocarbon migration. *AAPG bulletin*, 81(1):17–25, 1997.

[147] M. Rasmusson, F. Fagerlund, K. Rasmusson, Y. Tsang, and A. Niemi. Refractive-Light-Transmission Technique Applied to Density-Driven Convective Mixing in Porous Media With Implications for Geological CO_2 Storage. *Water Resources Research*, 53(11):8760–8780, 2017.

[148] A.J.H. Reesink and J.S. Bridge. Influence of superimposed bedforms and flow unsteadiness on formation of cross strata in dunes and unit bars. *Sedimentary Geology*, 202(1-2):281–296, 2007.

[149] Arnold J.H. Reesink and J.S. Bridge. Influence of bedform superimposition and flow unsteadiness on the formation of cross strata in dunes and unit bars — Part 2, further experiments. *Sedimentary Geology*, 222(3-4):274–300, 2009.

[150] Hans-Erich. Reineck and I. B. (Indra Bir) Singh. *Depositional Sedimentary Environments : With Reference to Terrigenous Clastics*. Springer Berlin Heidelberg, 1980.

[151] Bo Ren. *Local capillary trapping and permeability-retarded accumulation during geologic carbon sequestration*. PhD thesis, 2017.

[152] Bo Ren, Steven L Bryant, and Larry W Lake. Estimating local capillary trap volume capacities using a geologic criterion. *International Journal of Greenhouse Gas Control*, 85:46–57, 2019.

[153] Bo Ren, Steven L Bryant, Larry W Lake, et al. Fast modeling of local capillary trapping during co_2 injection into a saline aquifer. In *Carbon Management Technology Conference*. Carbon Management Technology Conference, 2015.

[154] Bo Ren, Steven L Bryant, Larry W Lake, et al. Quantifying local capillary trapping storage capacity using geologic criteria. In *Carbon Management Technology Conference*. Carbon Management Technology Conference, 2015.

[155] Bo Ren, Jennifer M. Delaney, Larry W. Lake, and Steven L. Bryant. Interplay Between Permeability Retardation and Capillary Trapping of Rising Carbon Dioxide in Storage Reservoirs. *SPE Journal*, 23(05):1866–1879, 2018.

[156] CA Reynolds and S Krevor. Characterizing flow behavior for gas injection: Relative permeability of co_2-brine and n_2-water in heterogeneous rocks. *Water Resources Research*, 51(12):9464–9489, 2015.

[157] Catriona A. Reynolds, Martin J. Blunt, and Samuel Krevor. Multiphase Flow Characteristics of Heterogeneous Rocks From CO_2 Storage Reservoirs in the United Kingdom. *Water Resources Research*, 54(2):729–745, 2018.

[158] Catriona A Reynolds, Martin J Blunt, and Samuel Krevor. Multiphase flow characteristics of heterogeneous rocks from co_2 storage reservoirs in the united kingdom. *Water Resources Research*, 54(2):729–745, 2018.

[159] Catriona A Reynolds, Hannah Menke, Matthew Andrew, Martin J Blunt, and Samuel Krevor. Dynamic fluid connectivity during steady-state multiphase flow in a sandstone. *Proceedings of the National Academy of Sciences*, 114(31):8187–8192, 2017.

[160] Philip Ringrose and Mark Bentley. *Reservoir Model Design*. Springer Netherlands, Dordrecht, 2015.

[161] Philip S Ringrose, Allard W Martinius, and Jostein Alvestad. Multiscale geological reservoir modelling in practice. *Geological Society, London, Special Publications*, 309(1):123–134, 2008.

[162] P.S. Ringrose and P.W.M. Corbett. Controls on two-phase fluid flow in heterogeneous sandstones. *Geological Society, London, Special Publications*, 78(1):141–150, 1994.

[163] P.S. Ringrose, J.L. Jensen, and K.S. Sorbie. Use of Geology in the Interpretation of Core-Scale Relative Permeability Data. *SPE Formation Evaluation*, 11(03):171–176, 1996.

[164] P.S. Ringrose, K.S. Sorbie, P.W.M. Corbett, and J.L. Jensen. Immiscible flow behaviour in laminated and cross-bedded sandstones. *Journal of Petroleum Science and Engineering*, 9(2):103–124, 1993.

[165] D.A Robinson and S.P Friedman. Observations of the effects of particle shape and particle size distribution on avalanching of granular media. *Physica A: Statistical Mechanics and its Applications*, 311(1-2):97–110, 2002.

[166] Joeri Rogelj, Alexander Popp, Katherine V Calvin, Gunnar Luderer, Johannes Emmerling, David Gernaat, Shinichiro Fujimori, Jessica Strefler, Tomoko Hasegawa, Giacomo Marangoni, et al. Scenarios towards limiting global mean temperature increase below 1.5 c. *Nature Climate Change*, 8(4):325, 2018.

[167] Anthony Rosato, Katherine J. Strandburg, Friedrich Prinz, and Robert H. Swendsen. Why the Brazil nuts are on top: Size segregation of particulate matter by shaking. *Physical Review Letters*, 58(10):1038–1040, 1987.

[168] Anthony D. Rosato, Denis L. Blackmore, Ninghua Zhang, and Yidan Lan. A perspective on vibration-induced size segregation of granular materials. *Chemical Engineering Science*, 57(2):265–275, 2002.

[169] Oystein Roti and Richard A. Dawe. Modelling fluid flow in cross-bedded sections. *Transport in Porous Media*, 12(2):143–159, 1993.

[170] David M Rubin. Cross-bedding, bedforms, and paleocurrents. *SEPM Concepts in sedimentology and paleontology*, 1:187p, 1987.

[171] David M Rubin and Carissa L Carter. Bedforms 4.0: Matlab code for simulating bedforms and cross-bedding. Technical report, 2005.

[172] David M Rubin and Carissa L Carter. *Bedforms and cross-bedding in animation*. Number 2. Sepm Society for Sedimentary, 2006.

[173] Ehsan Saadatpoor, Steven L. Bryant, and Kamy Sepehrnoori. New Trapping Mechanism in Carbon Sequestration. *Transport in Porous Media*, 82(1):3–17, 2010.

[174] Ehsan Saadatpoor, Steven Lawrence Bryant, Kamy Sepehrnoori, et al. Effect of heterogeneous capillary pressure on buoyancy-driven co_2 mi-

gration. In *SPE Symposium on Improved Oil Recovery*. Society of Petroleum Engineers, 2008.

[175] M.P. Sampat, Zhou Wang, S. Gupta, A.C. Bovik, and M.K. Markey. Complex Wavelet Structural Similarity: A New Image Similarity Index. *IEEE Transactions on Image Processing*, 18(11):2385–2401, 2009.

[176] Ji-Quan Shi, Ziqiu Xue, and Sevket Durucan. Supercritical co_2 core flooding and imbibition in tako sandstone—influence of sub-core scale heterogeneity. *International Journal of Greenhouse Gas Control*, 5(1):75–87, 2011.

[177] Elizabeth J Spiteri and Ruben Juanes. Impact of relative permeability hysteresis on the numerical simulation of wag injection. *Journal of Petroleum Science and Engineering*, 50(2):115–139, 2006.

[178] Elizabeth J Spiteri, Ruben Juanes, Martin J Blunt, Franklin M Orr, et al. A new model of trapping and relative permeability hysteresis for all wettability characteristics. *Spe Journal*, 13(03):277–288, 2008.

[179] Shayan Tavassoli, Prasanna Krishnamurthy, Emily Beckham, Tip Meckel, Kamy Sepehrnoori, et al. Co storage in deltaic saline aquifers: Invasion percolation and compositional simulation. In *SPE Reservoir Characterisation and Simulation Conference and Exhibition*. Society of Petroleum Engineers, 2019.

[180] Michele Moisio Thomas and Jamie A Clouse. Scaled physical model of secondary oil migration. *AAPG bulletin*, 79(1):19–28, 1995.

[181] L. Trevisan, P.G. Krishnamurthy, and T.A. Meckel. Impact of 3D capillary heterogeneity and bedform architecture at the sub-meter scale on CO_2 saturation for buoyant flow in clastic aquifers. *International Journal of Greenhouse Gas Control*, 56:237–249, 2017a.

[182] Luca Trevisan, Abdullah Cihan, Fritjof Fagerlund, Elif Agartan, Hiroko Mori, Jens T. Birkholzer, Quanlin Zhou, and Tissa H. Illangasekare. Investigation of mechanisms of supercritical CO_2 trapping in deep saline reservoirs using surrogate fluids at ambient laboratory conditions. *International Journal of Greenhouse Gas Control*, 29:35–49, 2014.

[183] Luca Trevisan, Ronny Pini, Abdullah Cihan, Jens T. Birkholzer, Quanlin Zhou, Ana Gonzalez-Nicolas, and Tissa H. Illangasekare. Imaging and quantification of spreading and trapping of carbon dioxide in saline aquifers using meter-scale laboratory experiments. *Water Resources Research*, 53(1):485–502, 2017b.

[184] Luca Trevisan, Ronny Pini, Abdullah Cihan, Jens T. Birkholzer, Quanlin Zhou, and Tissa H. Illangasekare. Experimental analysis of spatial correlation effects on capillary trapping of supercritical CO_2 at the intermediate laboratory scale in heterogeneous porous media. *Water Resources Research*, 51(11):8791–8805, 2015.

[185] Takeshi Tsuji, Fei Jiang, and Kenneth T Christensen. Characterization of immiscible fluid displacement processes with various capillary numbers and viscosity ratios in 3d natural sandstone. *Advances in Water Resources*, 95:3–15, 2016.

[186] C.J.C. Van De Ven and Kevin G. Mumford. Visualization of gas dissolution following upward gas migration in porous media: Technique and implications for stray gas. *Advances in Water Resources*, 115:33–43, 2018.

[187] LGH Van der Meer. The co_2 storage efficiency of aquifers. *Energy conversion and management*, 36(6-9):513–518, 1995.

[188] Guy Vasseur, Xiaorong Luo, Jianzhao Yan, Didier Loggia, Renaud Toussaint, and Jean Schmittbuhl. Flow regime associated with vertical secondary migration. *Marine and petroleum geology*, 45:150–158, 2013.

[189] G Wagner, A Birovljev, P Meakin, J Feder, and T Jossang. Fragmentation and migration of invasion percolation clusters: Experiments and simulations. *Physical Review E*, 55(6):7015, 1997.

[190] Ying Wang, Changyong Zhang, Ning Wei, Mart Oostrom, Thomas W Wietsma, Xiaochun Li, and Alain Bonneville. Experimental study of crossover from capillary to viscous fingering for supercritical co_2–water displacement in a homogeneous pore network. *Environmental science & technology*, 47(1):212–218, 2013.

[191] K.J. Weber. Influence of Common Sedimentary Structures on Fluid Flow in Reservoir Models. *Journal of Petroleum Technology*, 34(03):665–672, 1982.

[192] David Wilkinson and Jorge F Willemsen. Invasion percolation: a new form of percolation theory. *Journal of Physics A: Mathematical and General*, 16(14):3365, 1983.

[193] Hirotatsu Yamabe, Takeshi Tsuji, Yunfeng Liang, and Toshifumi Matsuoka. Lattice boltzmann simulations of supercritical co_2–water drainage displacement in porous media: Co_2 saturation and displacement mechanism. *Environmental science & technology*, 49(1):537–543, 2015.

[194] Jianzhao Yan, Xiaorong Luo, Weimin Wang, Renaud Toussaint, Jean Schmittbuhl, Guy Vasseur, Fang Chen, Alan Yu, and Likuan Zhang. An experimental study of secondary oil migration in a three-dimensional tilted porous medium. *AAPG bulletin*, 96(5):773–788, 2012.

[195] Zhibing Yang, Liang Tian, Auli Niemi, and Fritjof Fagerlund. Upscaling of the constitutive relationships for co_2 migration in multimodal heterogeneous formations. *International Journal of Greenhouse Gas Control*, 19:743–755, 2013.

[196] Ioannis Zacharoudiou, Edo S Boek, and John Crawshaw. The impact of drainage displacement patterns and haines jumps on co_2 storage efficiency. *Scientific reports*, 8(1):1–13, 2018.

[197] Changyong Zhang, Mart Oostrom, Thomas W Wietsma, Jay W Grate, and Marvin G Warner. Influence of viscous and capillary forces on immiscible fluid displacement: Pore-scale experimental study in a water-wet micromodel demonstrating viscous and capillary fingering. *Energy & Fuels*, 25(8):3493–3505, 2011.

[198] Xianglei Zheng, Nariman Mahabadi, Tae Sup Yun, and Jaewon Jang. Effect of capillary and viscous force on co_2 saturation and invasion pattern in the microfluidic chip. *Journal of Geophysical Research: Solid Earth*, 122(3):1634–1647, 2017.